

THESIS FOR THE DEGREE OF DOCTOR OF PHILOSOPHY

Novel Materials and Technologies for IR
Optoelectronic Applications

Yuxin Song

(宋禹忻)

Photonics Laboratory
Department of Microtechnology and Nanoscience – MC2
CHALMERS UNIVERSITY OF TECHNOLOGY
Göteborg, Sweden 2012

Novel Materials and Technologies for IR Optoelectronic Applications

Yuxin Song

Göteborg, March 2012

©YUXIN SONG, 2012

ISBN 978-91-7385-637-9

Doktorsavhandlingar vid Chalmers Tekniska Högskola
Ny serie nr 3318
ISSN 0346-718X

Technical Report MC2-212
ISSN 1652-0769

Photonics Laboratory
Department of Microtechnology and Nanoscience – MC2
Chalmers University of Technology, SE-412 96 Göteborg, Sweden
Telephone: +46 (0) 31 772 1000

Printed by Reproservice, Chalmers University of Technology
Göteborg, Sweden, March 2012

To: Yuyan

Novel materials and technologies for IR optoelectronic applications

Yuxin Song

Photonics Laboratory

Department of Microtechnology and Nanoscience-MC2

Chalmers University of Technology, SE-412 96 Göteborg, Sweden

Abstract

This thesis focuses on novel III-V materials (InAs/GaSb type-II superlattices, T2SL, and dilute bismides) and metamorphic growth techniques for infrared optoelectronics all of which may find wide spread applications in telecommunication, energy harvesting and saving, sensing and imaging. Mid-wavelength infrared (MWIR) and long-wavelength infrared (LWIR) photodetectors at the atmospheric windows of 3-5 and 8-12 μm , respectively, are currently dominated by HgCdTe and quantum well infrared photodetectors. These detectors, however, suffer from the suitability for making focal plane array (FPA) detectors due to the material non-uniformity or the low operation temperature that significantly increases the cost for a practical detection or imaging system. InAs/GaSb type-II superlattices are promising candidates for FPA detectors with better performance at a lower cost. Dilute bismides where a small amount of Bi atoms are incorporated into traditional host III-V semiconductors have theoretically shown a number of interesting physical properties. The large energy band bowing effect with retained transport and optical properties make these materials attractive for making short-wavelength infrared (SWIR), MWIR and LWIR optoelectronic devices. Dilute bismides have been only little studied among the III-V semiconductors, and in particular epitaxial growth of dilute III-SbBi is almost unexplored. Metamorphic growth is an efficient technique for lattice engineering and useful for device applications such as multi-junction solar cells, III-V and Si integration, electronic and optoelectronic devices on cheap substrates. Here, growth optimization and innovations to minimize threading dislocations are challenging and crucial for improving the material quality.

The work in this thesis deals with issues related to the realization of these novel III-V materials and metamorphic growth techniques using molecular beam epitaxy (MBE). It is investigated how doping in alloy graded metamorphic buffers influences material quality and a new method to reduce dislocation density and improve optical quality by using dilute nitride buffer layers is demonstrated. Design and growth optimization of T2SL structures for mid-IR detectors are presented. MBE growth of novel dilute III-SbBi alloys is investigated. The growth of GaSbBi is reported for the first time. The abnormal lattice contraction of GaSbBi is discovered and explained.

Keywords: infrared, metamorphic, alloy graded buffer, molecular beam epitaxy, threading dislocation, InAs/GaSb type-II superlattice, dilute bismide, GaSbBi, InSbBi

List of papers

This thesis is based on the following appended papers:

- [A] I. Tångring, **Y. X. Song**, Z. H. Lai, S. M. Wang, M. Sadeghi, and A. Larsson, “A study of the doping influence on strain relaxation of graded composition InGaAs layers grown by molecular beam epitaxy,” *J. Cryst. Growth*, **311** (7), 1684-1687 (2009).
- [B] **Y. X. Song**, S. M. Wang, I. Tångring, Z. H. Lai, and M. Sadeghi, “Effects of doping and grading slope on surface and structure of metamorphic InGaAs buffers on GaAs substrates,” *J. Appl. Phys.*, **106** (12), 123531-123537 (2009).
- [C] **Y. X. Song**, S. M. Wang, Z. H. Lai, and M. Sadeghi, “Enhancement of optical quality in metamorphic quantum wells using dilute nitride buffers,” *Appl. Phys. Lett.*, **97** (9), 91903 (2010).
- [D] **Y. X. Song**, S. M. Wang, X. H. Cao, Z. H. Lai, and M. Sadeghi, “Investigation of metamorphic InGaAs quantum wells using N-incorporated buffer on GaAs grown by MBE,” *J. Cryst. Growth*, **323** (1), 21-25 (2011).
- [E] **Y. X. Song**, S. M. Wang, C. Asplund, R. Marcks von Würtemberg, H. Malm, A. Karim, F. Abbas, X. Lu, and J. Shao, “Growth optimization, strain compensation and structure design of InAs/GaSb type-II superlattices for mid-infrared imaging,” submitted to *J. Cryst. Growth*.
- [F] **Y. X. Song**, S. M. Wang, I. S. Roy, P. X. Shi, and A. Hallen, “Growth of GaSb_{1-x}Bi_x by molecular beam epitaxy,” *J. Vac. Sci. Technol., B* **30** (2), 02B114-7 (2012).
- [G] **Y. X. Song**, S. M. Wang, I. S. Roy, P. X. Shi, and A. Hallen, “MBE growth and lattice contraction of GaSb_{1-x}Bi_x thin films,” submitted to *Cryst. Growth & Design*.

Other papers not included in this thesis:

Journal papers:

- [I] H. Ye, P. F. Lu, Z. Yu, **Y. X. Song**, D. Wang, and S. M. Wang, “Critical thickness and radius for axial heterostructure nanowires using finite-element method,” *Nano Letters* **9**, 1921 (2009).
- [II] S. M. Wang, G. Adolfsson, H. Zhao, **Y. X. Song**, M. Sadeghi, J. Gustavsson, P. Modh, Å. Haglund, P. Westbergh, and A. Larsson, “Growth of dilute nitrides and 1.3 μm edge emitting lasers on GaAs by MBE,” *Phys. Status Solidi (b)*, **248**, 1207 (2011).
- [III] I. Tangring, **Y. X. Song**, D. H. Wu, Z. C. Niu, S. M. Wang, and A. Larsson, “Metamorphic InGaAs telecom lasers on GaAs,” *Proceedings of SPIE*, **7230**, 723003 (2009)

Book chapter:

- [I] X. J. Shang, **Y. X. Song**, Z. C. Niu, and S. M. Wang, “Metamorphic Quantum Well Lasers,” *Lattice Engineering, Technologies and Applications*, edited by Shumin Wang, Pan Stanford 2012, ISBN 9789814316293

Peer reviewed international conference papers:

- [I] I. Tångring, **Y. X. Song**, Z. H. Lai, S. M. Wang, M. Sadeghi, and A. Larsson, “Influence of Doping on Structural Properties of Graded InGaAs Layers Grown by MBE,” *15th International Conference on Molecular Beam Epitaxy*, Vancouver, Canada (2008).
- [II] **Y. X. Song**, S. M. Wang, I. Tångring, Z. H. Lai, M. Sadeghi, and A. Larsson, “Doping influence on structural property of linearly graded composition InGaAs buffer layer grown by MBE,” *15th European Molecular Beam Epitaxy Workshop*, Zakopane, Poland (2009).
- [III] S. M. Wang, **Y. X. Song**, I. Tångring, Z. H. Lai, M. Sadeghi, A. Larsson, D. H. Wu, and Z. C. Niu, “Metamorphic InGaAs materials and telecom lasers,” *International Conference on Materials and Advanced Technology (ICMAT)*, Singapore (2009) (*invited talk*).

- [IV] T. W. Reenaas, P. E. Vullum, **Y. X. Song**, M. Sadeghi, S. F. Thomassen, R. Holmestad, S. M. Wang, and B. O. Fimland, “Comparative Study of Spacer Layers for InAs Quantum Dot Stacks,” *22nd International Conference on Indium Phosphide and Related Materials (IPRM)*, Takamatsu, Japan (2010)
- [V] **Y. X. Song**, S. M. Wang, Z. H. Lai and M. Sadeghi, “Blocking of threading dislocation by nitrogen incorporation in metamorphic buffers,” *16th International Conference on Molecular Beam Epitaxy*, Berlin, Germany (2010)
- [VI] **Y. X. Song**, S. M. Wang, “Molecular Beam Epitaxy Growth of $\text{InSb}_x\text{Bi}_{1-x}$,” *Second International Workshop on Bismuth-Containing Semiconductors: Theory, Simulation and Experiment*, Guildford, UK (2011)
- [VII] **Y. X. Song**, S. M. Wang, C. Asplund, H. Malm, X. Lu, and J. Shao, “Growth Optimization for InAs/GaSb T2SL Structures by MBE,” *16th European Molecular Beam Epitaxy Workshop (Euro-MBE2011)*, Alpe d’Huez, France (2011).
- [VIII] **Y. X. Song**, S. M. Wang and I. S. Roy, “Molecular Beam Epitaxy Growth of $\text{GaSb}_x\text{Bi}_{1-x}$,” *28th North American Molecular Beam Epitaxy Conference (NAMBE2011)*, San Diego, USA (2011).

Acknowledgement

During my life as a PhD student I have received help from many people to whom I would like to express my gratitude.

I found myself so lucky to meet Prof. Shumin Wang who has been both a teacher and a friend. As my examiner and supervisor, I would like to express my deepest gratitude to his insightful, patient and passionate guidance. As a friend, I appreciate his availability whenever I needed help, his enthusiasm on sharing his interest and knowledge, and the occasions he created on which we together had memorable experiences.

Special gratitude to my predecessor Dr. Ivar Tångring for introducing me into the field, teaching me all the experimental skills, all the help in daily life, and discussing and debating with me on all the political topics. Warm thanks to Mahdad Sadeghi for providing me the epitaxy materials, ebulliently teaching me all the knowledge about MBE, solving all the MBE problems, and the fun talks in the noisy MBE lab.

I would like to thank all the former and present colleagues in the Photonics Lab who have been supporting me whenever I needed help in my research. Colleagues in IRnova, Hedda Malm, Carl Asplund etc. are thanked for the enjoyable collaborations. Dr. Zonghe Lai is sincerely thanked for implementing the TEM measurements for my tens of samples and also fruitful discussions. Ass. Prof. Huan Zhao is acknowledged for teaching me the experimental skills in the cleanroom and sharing the perplexing time when we just got the new MBE.

I would also like to thank the people helping me in the daily life all the time. Jörgen Bengtsson, Carl Borgentun, Benjamin Kögel and Göran Adolfsson are warmly thanked for taking care of my life so much. Special acknowledgements also to all the fellows in the Photonics Lab for the fun time after work, playing Ping-Pong and in the motion hall.

Sincere gratitude is given to Prof. Zhongyuan Yu in BUPT, Beijing, China for bridging me with Chalmers and offering me the opportunity.

I'd also like to thank all other friends made in Sweden. They make me feel like at home.

The China Scholarship Council and the Swedish Research Council (VR) are acknowledged for financial support.

Finally, I would like to sincerely thank my beloved wife, who accompanied me wherever I am on this earth. I would particularly like to thank my parents and parents in law for always loving and supporting me.

Yuxin Song

Göteborg, Feb 2012

List of acronyms

2D	two-dimensional
3D	three-dimensional
AFM	atomic force microscopy
AR	anisotropic ratio
BEP	beam equivalent pressure
BFM	beam flux monitor
FEM	finite element method
FIB	focused ion-beam
FPA	focal plane array
FTIR	Fourier transform infrared spectroscopy
FWHM	full-width-at-half-maximum
HEMT	high-electron mobility transistor
HH	heavy-hole
ICL	interband cascade laser
IEEE	Institute of Electrical and Electronics Engineers
IMF	interfacial misfit
IR	infrared
LAG	linear alloy grading/graded
LH	light hole
LTG	linear source temperature grading/graded
LWIR	long-wavelength infrared
MBE	molecular beam epitaxy
MCT	HgCdTe
MD	misfit dislocation
M-LTG	mirrored linear source temperature grading/graded
MOCVD	metal-organic chemical vapour deposition
MOVPE	metal-organic vapor phase epitaxy
MWIR	mid-wavelength infrared

NIR	near infrared
PID	proportional–integral–derivative
PL	photoluminescence
QCL	quantum cascade laser
QD	quantum dot
QW	quantum well
QWIP	quantum well infrared photodetector
RBS	Rutherford backscattering spectroscopy
RHEED	high-energy electron diffraction
RMS	root mean square
SIMS	secondary ion mass spectrometry
SL	superlattice
SO	spin-orbit
SWIR	short-wavelength infrared
T2SL	type-II superlattice
TD	threading dislocation
TEM	transmission electron microscopy
VCSEL	vertical cavity surface emitting laser
VLWIR	very-long-wavelength infrared
XRD	X-ray diffraction
XTEM	cross-sectional transmission electron microscopy

Table of contents

Abstract.....	i
List of papers.....	iii
Acknowledgement	vi
List of acronyms	vii
Table of contents.....	ix
1 Introduction	1
1.1 Infrared optoelectronic applications.....	1
1.2 Challenges and possible solutions of IR devices	3
1.2.1 Limitation from substrates	3
1.2.2 Challenges for MWIR and LWIR photodetection.....	6
1.3 Scope of this thesis	7
2 MBE growth and characterization techniques	9
2.1 MBE growth.....	9
2.2 Surface characterization	12
2.2.1 Atomic force microscopy (AFM)	12
2.2.2 Reflective high-energy electron diffraction (RHEED).....	13
2.3 Structural characterization.....	15
2.3.1 Transmission electron microscopy (TEM)	15
2.3.2 X-ray diffraction (XRD)	17
2.3.3 Rutherford backscattering spectroscopy (RBS).....	21
2.3.4 Secondary ion mass spectrometry (SIMS).....	22
2.4 Optical characterization by Photoluminescence.....	22
3 Metamorphic technology	25
3.1 Introduction	25
3.2 Strain relaxation in III-V semiconductors	27
3.2.1 Lattice mismatch and strain	27
3.2.2 Strain relaxation	27
3.2.3 Dislocations in zincblende crystals.....	29
3.3 Alloy-graded metamorphic buffer layers and doping effect.....	31

3.3.1	Strain relaxation in alloy graded buffer layers	32
3.3.2	Interplays between doping, grading profiles and grading slopes	36
3.3.3	Design of alloy-graded buffers for optoelectronic devices	37
3.4	Threading dislocation blocking.....	38
3.4.1	TD blocking through interactions with strain fields.....	38
3.4.2	TD blocking by dilute nitrides.....	39
4	Type II superlattice for MIR imaging.....	43
4.1	Introduction.....	43
4.2	Optimization of MBE growth conditions	44
4.3	Strain compensation.....	47
4.3.1	Strain compensation methods.....	49
4.3.2	Theoretical modeling of strain compensation in T2SL	52
4.4	Band structure calculations of proposed T2SLs	55
4.5	Single pixel photodetector	57
5	Dilute bismides.....	59
5.1	Introduction.....	59
5.2	Strategies for enhancing Bi incorporation	61
5.3	MBE growth and characterization of GaSb _{1-x} Bi _x	63
5.3.1	GaSbBi on GaSb substrates.....	63
5.3.2	Surface morphology	63
5.3.3	Confirmation of Bi incorporation.....	63
5.3.4	Lattice contraction.....	65
5.3.5	GaSb _{1-x} Bi _x on GaAs substrates.....	69
5.4	MBE growth and characterization of InSb _{1-x} Bi _x	69
5.4.1	Sample structure and growth.....	69
5.4.2	Surface morphology	69
5.4.3	Structural properties	70
5.4.4	Bi incorporation.....	72
5.4.5	Bi induced In/Ga intermixing.....	73
5.5	Bismuth as surfactant for InGaAs QW on GaAs	75
6	Summary of appended papers.....	77
Appendix	79
A1	Deviation of In segregation in alloy graded buffers	79

A2 Overall strain in T2SL structures with different strain compensation schemes	82
References.....	85
Papers [A]- [G]	96

1 Introduction

1.1 Infrared optoelectronic applications

Perhaps the most direct consciousness about infrared (IR) in people's life would be the TV remote controls which liberate lazy-bone TV fans from standing up from the couch and changing the channels. It might not be that easy to realize that another great invention, internet, which has revolutionized our life style, also relies on IR optoelectronic technology. The super fast vehicles carrying our data to/from YouTube, Skype, Twitter, etc. in the fibers connecting cities, countries and even continents are actually infrared light. IR applications have large impacts on not only our daily life but also industry, meteorology, astronomy, security and, probably more, military.

Figure 1-1 summarizes IR applications in different sub-divisions and corresponding involved materials and technologies as guidance. The ones marked in red are related to the work in this thesis.

The first row of Fig. 1-1 shows the electromagnetic spectrum. IR covers a broad region with wavelength larger than that of visible light and shorter than that of millimeter wave [1]. Depending on different criterions, the IR light can be made into sub-divisions in many schemes. One of them divides the IR region into near infrared (NIR), short-wavelength infrared (SWIR), mid-wavelength infrared (MWIR), long-wavelength infrared (LWIR) and very-long-wavelength infrared (VLWIR), based on the spectral bands of common IR detectors and the atmospheric windows, shown in the second row of Fig. 1-1. Some important applications of IR in each sub-division except VLWIR are summarized in the third row labeled "Applications". TV remote controls and current night vision devices with active illumination usually employ NIR. Wavelength of 850 nm is one of the choices for 10 and 100 Gigabit Ethernet for high-speed computer network standards, developed by the Institute of Electrical and Electronics Engineers (IEEE) [2], for short reach data communication with distances of 100+ meters. For the SWIR range, the most significant application would be in optical fiber communications utilizing the wavelength of 1.3 and 1.55 μm , which build the backbone of internet. 1.3 μm IR light has the least dispersion effect in glass fibers and is suitable for medium-reach communication systems (<40 km), while 1.55 μm IR light has minimum loss when transferred for long distance in glass fibers and is excellent for long reach systems (>40 km) [3]. Another potential application in SWIR is the 1 eV (1.24 μm) junction solar cell which is of significant technical challenge. A four-junction solar cell with a 1 eV junction embedded is promising to increase the solar energy conversion efficiency as high as 52% under concentrated condition (500 sun) [4]. MWIR and LWIR cover the two atmospheric

windows 3-5 μm and 8-14 μm , respectively, within which the IR light has low absorption from the atmosphere. Therefore, these two spectral regions are often chosen for IR imaging and remote gas sensing. In a broad sense, IR imaging covers thermal imaging, hyperspectral imaging, meteorology imaging, IR astronomy imaging with discrete wavelengths, etc [5]. The remote gas sensing is mostly based on IR vibrational spectroscopy of gas molecules which can be utilized to identify gas species by analysis of their constituent bonds with unique vibration frequencies [6]. The choice of these two bands should be based on background intensity, scene characteristics, temperature contrast and also weather conditions. MWIR provides higher contrast, higher transmittivity in high humidity and higher resolution due to relatively shorter wavelength and subsequently smaller optical diffraction. LWIR has higher sensitivity to ambient temperature objects, better performance in weather conditions with large particles in air, and higher immunity to atmospheric turbulence, due to longer wavelength [1]. Similar molecular spectroscopy has promising applications in breath diagnostics for early detection of breast cancer, lung cancer, and pulmonary diseases in real-time and with high sensitivity [7].

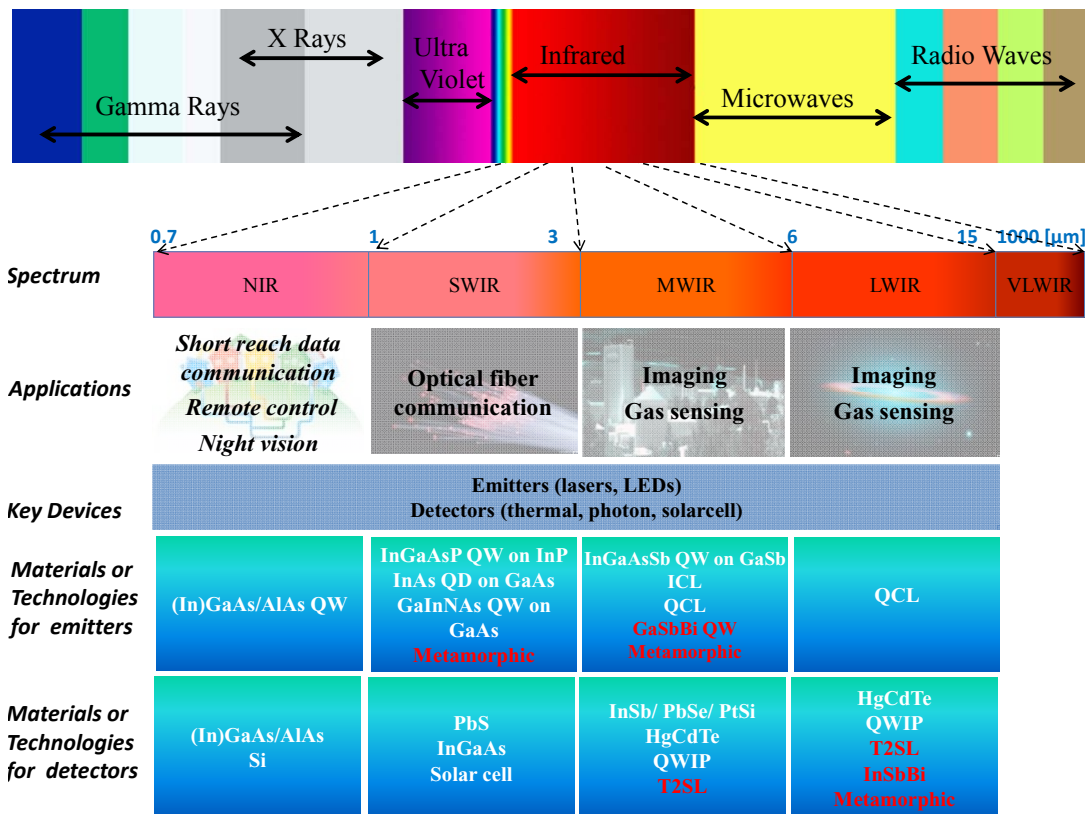


Figure 1-1. IR spectrum with applications in different sub-divisions and corresponding involved materials and technologies. The ones marked in red are related to the work in this thesis. Abbreviations: quantum well (QW), quantum cascade laser (QCL), interband cascade laser (ICL), quantum well infrared photodetector (QWIP), light-emitting diode (LED) and focal plane array (FPA).

1.2 Challenges and possible solutions of IR devices

All these applications are realized upon IR optoelectronic devices and systems. Emitters which supply IR light and detectors which detect IR light and convert it into electrical signals are two of the most important device categories. The last two rows of Fig. 1-1 list the common materials and technologies for both IR emitters and detectors. High performance IR lasers usually employ strained QWs in the active region, while IR detectors require lattice matched bulk layers to enhance optical absorption. IR technology has been developing rapidly from the mid last century and is getting more and more established. However, challenges still exist to be conquered. High efficiency, high stability, high speed, high working temperature and low production cost etc. are the mainstream research directions which require large freedoms in material selection, structure design and mature growth technology.

1.2.1 Limitation from substrates

All heteroepitaxial growth must start from a substrate, which should have a large wafer size, low crystal defects and reasonable prices. Commercial substrates are usually limited to binary compounds or single elements. In order to increase absorption efficiency, detectors are usually very thick in several micrometers. Very little lattice mismatch of the epilayer to the substrate is tolerable to avoid formation of structural defects. Thin layers, like QW, are possible to grow without strain relaxation, but are limited by the critical thickness. Fig. 1-2 shows a diagram of band-gap vs lattice constant for common semiconductors. GaAs, InP and GaSb are the most common substrates for optoelectronics. Schematically, the vertical magenta belts cover materials with lattice constants closely matched to these substrates. The limitation for QWs is relatively looser within the grey belts. The horizontal pink belts mark a few wavelength divisions. The crosses between the vertical and horizontal belts illustrate the possible materials corresponding to contain substrates for different wavelength requirements. Taking the telecom wavelengths (1.3 and 1.55 μm) for example, the only possible solutions are GaInAs(P) or InGaAsSb on InP substrates while there is no material at both wavelengths lattice matching to GaAs or Si substrates. Furthermore, MWIR optoelectronic devices are usually built on GaSb substrates and there is no direct III-V solution for LWIR on any commercial substrates. Table 1-1 summaries possible maximum wavelengths limited to some of the common III-V substrates to the best of our knowledge. The arrow in the bottom of Fig. 1-2 indicates a general trend for substrates with larger wafer size, higher quality, lower price and more mature process technology. It is clear from Fig. 1-2 that IR optoelectronic devices, especially for long wavelengths, need to be fabricated on small, expensive and less mature substrates. Realizations of IR devices with long wavelengths on substrates with small lattice constants may help not only reduce

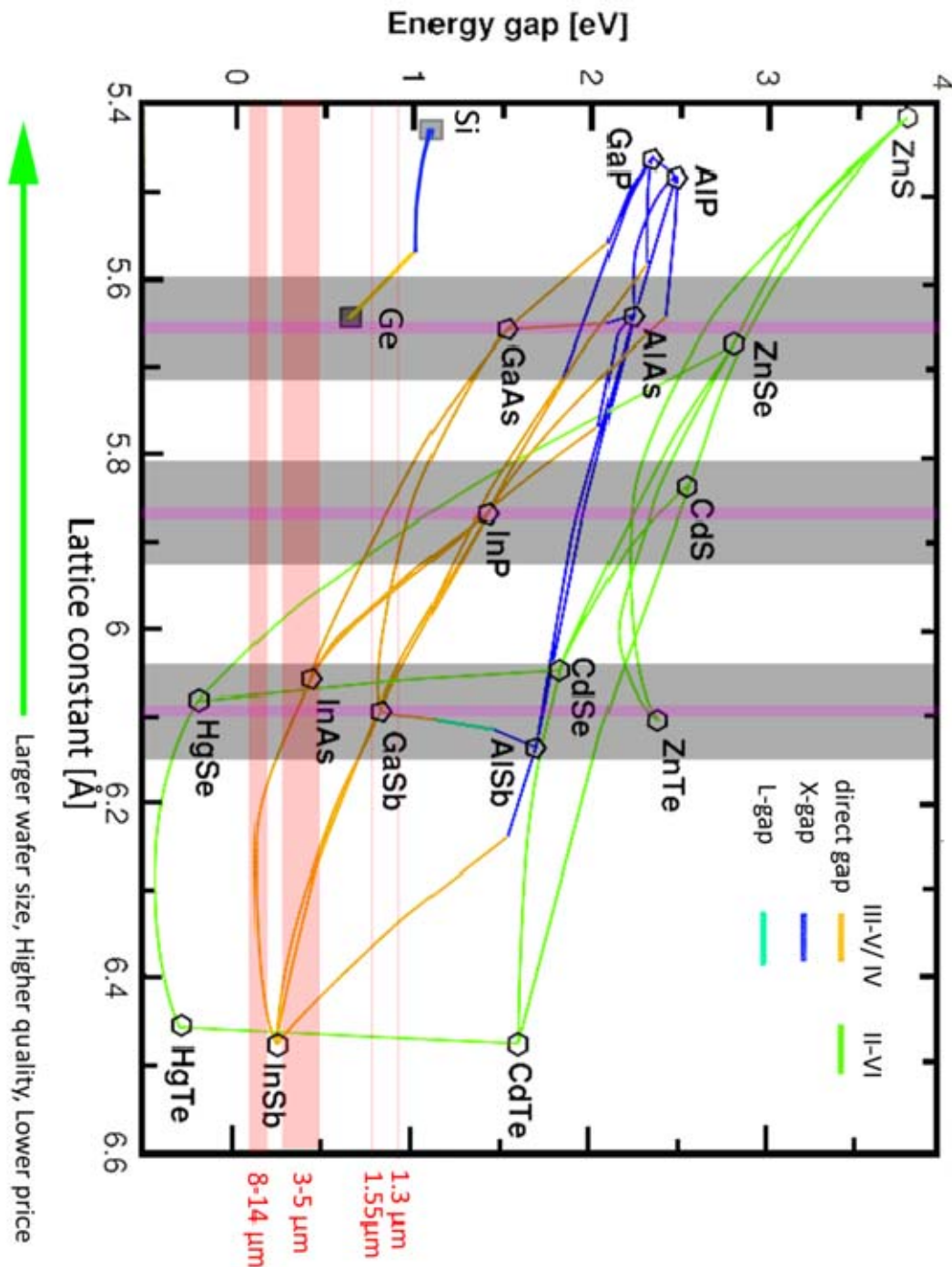


Figure 1-2. Band-gap vs. lattice constant for III-V, II-VI and IV compounds (dots) and their alloys (lines)[127]. The magenta and grey belts indicate lattice constants tolerably matched to some common substrates for QWs and bulk materials, respective. The pink lines and belts mark some of the IR regions.

cost but also improve the performance. For instance, telecom lasers with InGaAsP QWs grown on InP substrates reveal several drawbacks such as a low characteristic temperature making costly and energy inefficient coolers necessary to stabilize the lasing wavelength and the relatively small refractive index contrast making fabrication of low-cost vertical cavity surface emitting lasers (VCSELs) difficult. Telecom lasers built on GaAs may overcome these problems. It is

predicted that InGaAs QW lasers show the best characteristic temperature when they are grown on $\text{In}_{0.26}\text{Ga}_{0.74}\text{As}$ substrates [8] which are unfortunately unavailable commercially with high quality. The limitations of available substrates call for new materials, new device concepts employing band engineering or nanostructures, and new growth technologies for high performance IR optoelectronic devices at a low cost.

Table 1-1. Maximum achievable wavelength of common QWs and bulk materials grown on some commercial substrates.

substrates	max achievable wavelength [μm] (material)	
	QW	bulk
GaAs	$\sim 1.7 \mu\text{m}$ (GaInNAs)	$\sim 1 \mu\text{m}$ (GaInNAs)
InP	$\sim 2.5 \mu\text{m}$ (InAs)	$\sim 1.7 \mu\text{m}$ ($\text{In}_{0.53}\text{Ga}_{0.47}\text{As}$)
GaSb	$\sim 3.5 \mu\text{m}$ (GaInAsSb)	$\sim 3.5 \mu\text{m}$ (InAs)
InSb	—	$\sim 7.5 \mu\text{m}$ (InSb)

“Metamorphic” growth technology is one of the possible solutions which can break the lattice matching limitation. In this approach, a buffer layer is first grown on top of a commercial substrate to relax most of the strain and to retain a smooth surface with a low density of threading dislocations. Then a virtue substrate or template with a desired lattice constant and acceptable structural quality is grown on the metamorphic buffer followed by a prescribed device structure without strain relaxation. Metamorphic growth requires no process before or after epi-growth and can be utilized to integrate heterostructures with different lattice constants, for example, multi-junction solar cells [9], [10].

Novel device concepts utilizing intersubband transitions instead of interband transitions and sequential tunneling can largely help extend emission or absorption wavelengths in well established materials like GaAs/AlGaAs and InGaAs/InAlAs/InP. Quantum cascade lasers (QCLs) can lase through the use of intersubband transitions and sequential tunneling in a repeated stack of multiple coupled QWs [11] at the MWIR and LWIR regions. Similar processes but in the opposite way are employed in quantum well infrared photodetectors (QWIPs) for photodetection. QWIPs are one of the candidates for the third generation MWIR and LWIR detectors [12]. Another example of new device concepts employs band engineering of a unique type-II broken band alignment of InAs/GaSb with lattice mismatch of 0.61%. When InAs and GaSb thin layers are put together to form a superlattice, an effective band-gap can be formed and tuned from 0 to 0.5 eV by adjusting the thickness of the layers [13]. InAs/GaSb type-II superlattice (T2SL) on GaSb substrate is a promising candidate for high quality photodetectors working in both MWIR and LWIR [14], and has attracted great attention worldwide recently. Interband cascade lasers (ICLs) employ the same concept but using more complicated cascade structures to emit IR light in the MWIR range [15].

Novel materials employing isoelectronic dopants with a large difference in electronegativity with respect to the host alloy possess a large energy bowing effect and are therefore of particular interest for IR optoelectronic applications [16]. One famous example is dilute nitride. When a small amount of N is incorporated into InGaAs, as large as 160 meV/at %N band bowing can be obtained making GaInNAs a strong candidate for GaAs based telecom lasers [17]. Bismuth, the heaviest group V element, has been found to also have a large band bowing effect when incorporated in common III-V compounds [18], [19]. To the contrary of dilute nitrides, which modify the conduction band, the influence of Bi on the band structure occurs only in the valence band. The electron transport properties in dilute bismide materials are therefore much less influenced than those in dilute nitride materials [20]. The perturbation of Bi atoms in the valence band also leads to strong spin-orbit splitting [21]. All these provide new degrees of freedom to engineer band structure of semiconductors for potential electronic and optoelectronic applications using dilute bismides. Intensive research has been implemented recently on $\text{GaAs}_{1-x}\text{Bi}_x$ and related materials aiming to realize 1.55 μm telecom lasers on GaAs with low inter-valence band Auger recombination [22]. There are very few reports on other III-V-Bi compounds. The large valence band edge reduction resulted from Ga(In)SbBi is promising for realizing $>3 \mu\text{m}$ GaSb based type-I quantum well lasers [23]. Band bowing in $\text{InSb}_{1-x}\text{Bi}_x$ is expected to reach absorption wavelengths at 8-14 μm making it a promising candidate for LWIR detector material [24].

1.2.2 Challenges for MWIR and LWIR photodetection

Specific to the photodetection for gas sensing and imaging FPA detectors in MWIR and LWIR, the main requirements are higher pixel sensitivity, higher pixel density, multispectral functionality and higher operation temperature [25]. $\text{Cd}_x\text{Hg}_{1-x}\text{Te}$ (MCT) material is the most established candidate covering both MWIR and LWIR. Another well developed material is QWIP. The InAs/GaSb T2SL is expected to be a very attractive material system with superior performance compared with the two materials above [26]. The main advantages of MCT are high quantum efficiency, wide spectral bandwidth and high operating temperature, while it has problems with the low yield in fabricating FPAs and subsequently high cost. The advantages of QWIP are high uniformity, fast response and low cost based on mature III-V technology, while the main problems are low operating temperature, normal incident absorption forbidden and, most importantly, low quantum efficiency, requiring long integration time for imaging. T2SL has relatively high efficiency and is capable of operating at high temperatures.

1.3 Scope of this thesis

This thesis summarizes my work on novel materials and technologies for IR optoelectronic applications with focus on three main topics: metamorphic technology, T2SL materials and dilute bismide materials. MBE growth and characterization of the materials are the main perspectives.

Metamorphic technology has been employed with the aim of improving 1.3 and 1.55 μm InGaAs quantum well (QW) telecom lasers on GaAs substrates with high temperature stability. Alloy graded metamorphic InGaAs buffer layers are investigated with the main focus on studying the doping effect on quality of buffers with different grading profiles and slopes. A novel technique to block threading dislocations by using dilute nitride metamorphic buffers has been demonstrated.

MBE growth of InAs/GaSb T2SLs for MWIR imaging has been investigated and the growth conditions optimized. Different strain compensation strategies are proposed, theoretically analyzed and experimentally tested. Single pixel photodetector with a low dark current is demonstrated.

The work on dilute bismides focuses on MBE growth of III-SbBi and use of Bi as surfactant when growing InGaAs. $\text{GaSb}_{1-x}\text{Bi}_x$ thin films have been grown for the first time by MBE. Bismuth atoms are found to be an excellent surfactant for InGaAs leading to enhanced photoluminescence intensity and emission wavelength at room temperature.

The thesis is structured as follows. Chapter 2 starts with introduction to the MBE growth followed by various characterization techniques used in this work. Chapter 3 discusses about metamorphic technology. In Chapter 4 MBE growth and optimization of T2SL detector materials are presented. Chapter 5 describes the MBE growth and characterization of III-SbBi materials as well as the surfactant effect of Bi during the growth of InGaAs. Finally, summary of each appended paper is presented.

2 MBE growth and characterization techniques

Material growth by MBE and sample characterization for surface, structural and optical properties compose most of the experimental work in this thesis. MBE growth and some of the characterization techniques are introduced below with particular emphasis laid on the aspects closely related to the materials discussed in this thesis.

2.1 MBE growth

“Molecular beam epitaxy (MBE) is a term used to denote the epitaxial growth of compound semiconductor films by a process involving the reaction of one or more thermal molecular beams with a crystalline surface under ultra-high vacuum conditions.” This is the definition of MBE by its inventors John R. Arthur and Alfred Y. Cho [27]. Nowadays, MBE has become one of the most advanced and widely applied epitaxial techniques. The ultra-high vacuum (with a typical background pressure in 10^{-11} Torr range) in the growth chamber enables atoms evaporated from heated sources to impinge onto a substrate without collisions. The low growth rate (commonly around 1 monolayer/s) allows films to grow epitaxially with a precise thickness control down to the sub-monolayer level.

Figure 2-1 and Fig. 2-2 show a photo and a schematic layout of our Riber Compact21 MBE system, respectively. Cracker sources are equipped for arsenic and antimony to produce dimeric molecules (As_2 and Sb_2) from elemental sources (As_4 and Sb_4). The flux is controlled by needle valve without changing source and cracker temperatures. Nitrogen is produced by cracking pure N_2 in a RF source. All other elements including Bi, group III elements In, Ga and Al, and dopants Te, Si, Be are held in effusion cells. In and Ga sources are in “dual-filament” configuration which allows for using different temperatures for the material and the tip region. When an effusion cell is heated, a beam of atoms of the source material are incident onto the substrate. The beam flux is determined by the effusion cell temperature. All source temperatures in this MBE are regulated by proportional–integral–derivative (PID) controllers. A beam flux monitor (BFM) is utilized to measure the beam equivalent pressure (BEP) of each source which is related to the real flux, J , through

$$J = \alpha \frac{P}{\eta} \left(\frac{T}{M} \right)^{1/2} \quad (2-1)$$

where, P is the BEP of the element, M is the molecular weight, T is the absolute temperature of the source, η is ionization efficiency, and α is a constant related to

geometry and is the same for all sources in the same MBE system [28]. The ionization efficiency of an element η_x can be estimated relative to N_2 , using

$$\frac{\eta_x}{\eta_{N_2}} = \frac{0.4Z}{14} + 0.6 \quad (2-2)$$

where Z is the atomic number of element x .

Regular checking of BEP can help track the stability and any change of the source flux. The beam of group III atoms can be switched on and off by mechanical shutters providing a precision of sub-monolayer in epi-layer thickness. The ultra-high vacuum within the growth chamber is maintained by a high capacity cryopump and an ion pump, and liquid nitrogen cooled cryo-shrouds. The cryo-shroud between effusion cells eliminates thermal cross-talk and the other one surrounding the substrate holder acts mainly as impurity traps. The substrate holder is heated and can be rotated at a speed up to 300 revolution/minute to enhance uniformity of doping, alloy compositions and layer thickness across a 3" wafer.



Figure 2-1. A photo of a Riber Compact21 MBE system

Substrate temperature or growth temperature is one of the vital parameters determining the material quality. It is measured by both a thermocouple and a pyrometer. The pyrometer can directly measure the temperature of the sample with an accuracy of ± 5 °C as shown in Fig. 2-2. However it can only accurately measure temperatures above 450 °C. The thermocouple mounted on the backside of the substrate holder can measure lower temperatures, but the value can differ significantly from the real growth temperature on the sample surface. For most

samples involved in this thesis, the growth temperature is below 400 °C and therefore is measured only by a thermocouple.

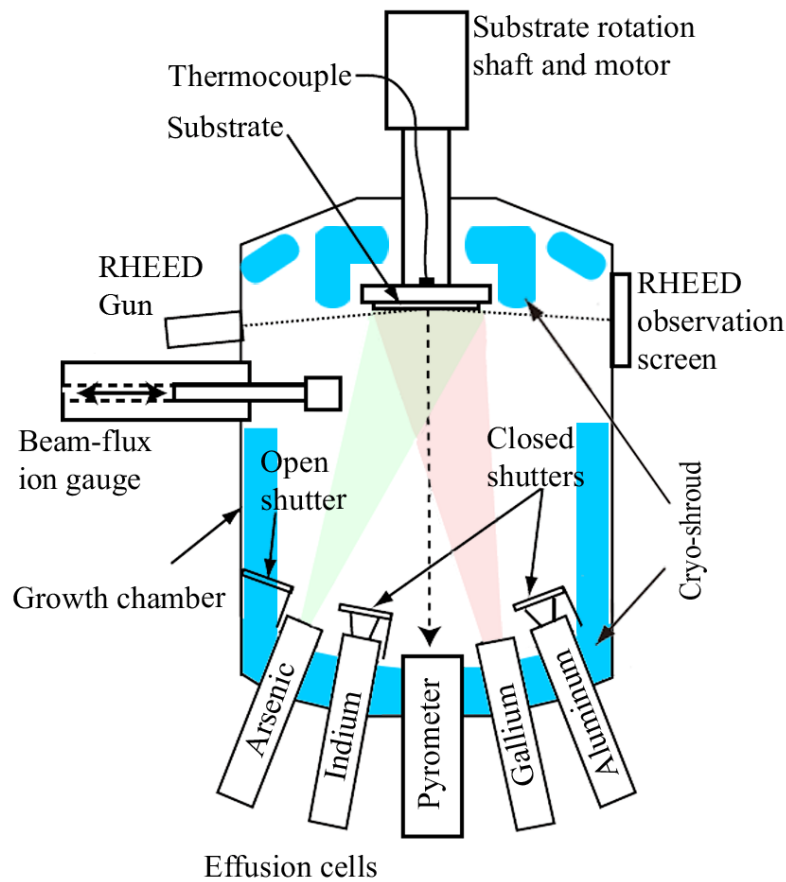


Figure 2-2. Schematic layout of a Riber Compact21 MBE system.

One of the advantages of MBE over other epitaxial technologies is that the ultra-high vacuum enables *in-situ* characterization by using reflective high-energy electron diffraction (RHEED). RHEED can be used to check surface reconstructions and calibrate the growth rate. A more detailed discussion of RHEED will be in Section 2.2.2.

Two MBE systems are installed in our lab, a VEECO EPI930 and a Riber Compact21. Growth of metamorphic samples was performed in the EPI930 system while the T2SLs and dilute bismides were grown by Riber Compact21. The EPI930 system is capable of maintaining very high vacuum ($\times 10^{-11}$ torr) for all the source temperatures at growth conditions (with As needle valve closed) after more than 14 years usage. The Riber Compact21 system includes an automatic wafer transfer system, making it very friendly for operators. Interestingly, many growth parameters are specific to a particular system, for example, the reading of BEP of

group-III sources at the same growth rate differs by almost twice in the two systems.

2.2 Surface characterization

Surface morphology of MBE-grown samples is an important indicator of the material quality. Here we discuss two surface characterization techniques: RHEED is used to *in-situ* monitor the surface morphology and atomic force microscopy (AFM) is to measure the surface morphology and roughness after growth.

2.2.1 Atomic force microscopy (AFM)

AFM is one of the most powerful tools to measure surface morphology of semiconductors with the vertical resolution of sub-nanometer. A small tip with a typical radius of 20 nm on a cantilever is used to probe the surface. In our measurements we use the tapping mode, in which the tip is driven by a piezoelectric element to oscillate at a frequency near the cantilever's resonant frequency. The van der Waals force acting on the tip can decrease the oscillation amplitude when the tip is close to the sample surface. The distance of the cantilever above the surface is adjusted to keep the same oscillation amplitude during the scanning. Thus, the surface topography is reconstructed by movement of the cantilever. Compared with the contact mode, the tapping mode offers little damage to the samples as well as a high signal over noise ratio resolution.

The equipment used in this thesis is a Digital Instruments Dimension 3000 Scanning Probe Microscope in which AFM is one of the working modes. The highest vertical resolution is 0.1 nm. Fig. 2-3 is an AFM image of MBE grown GaSb surface on a GaSb substrate showing clear atomic steps with 0.3 nm height difference.

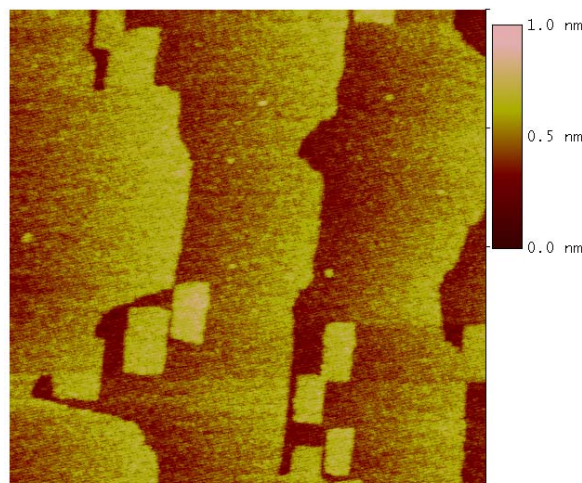


Figure 2-3. An $1 \times 1 \mu\text{m}^2$ AFM image of homo-epitaxial GaSb on a GaSb substrate showing single atomic layer steps.

The AFM measurement involves both mechanical movements and data processing. Artifacts would arise when interpreting the data. Under certain circumstances, these artifacts may be difficult to be eliminated, leading to false qualitative conclusions. Fig. 2-4 shows some typical artifacts one may observe during AFM measurements. The first type is the so-called “tail effect”. Clear tails can be observed at the right side of each Ga droplet in the left image. The data are recorded when the tip moving from left to right. When the tip meets a high droplet, it will move up quickly to avoid collision. After passing the droplet, it moves down in a slower pace, leading to insufficient closeness to the surface. The recorded height data is therefore higher than the real values. The “tails” look like “shadows” in the amplitude data channel as found in the right figure of Fig. 2-4, which can be utilized to judge whether some features are real or measurement defects. This problem can be solved by using slow scanning rates to enable the tip following the terrain. By comparing images scanned at different angles, artifacts are possible to be detected. The second type is “repeating features”. From the right amplitude image in Fig. 2-4 one may find that the top shape is almost the same for all the Ga droplets. This is an indication that the tip is dirty, probably adhered with dust particles. If necessary, a new tip is required.

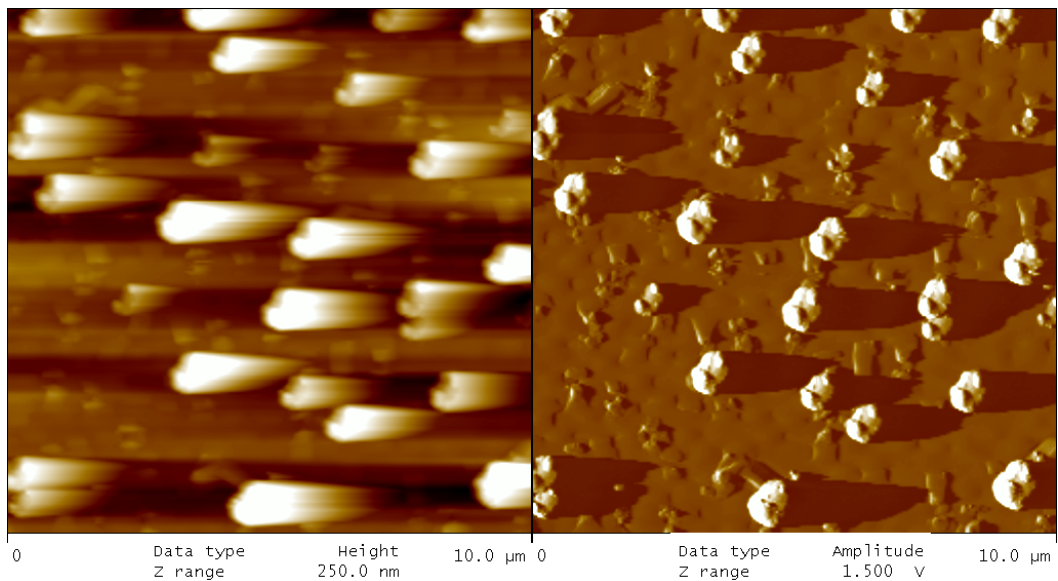


Figure 2-4. $10 \times 10 \mu\text{m}^2$ AFM images of Ga droplets on GaAs(Bi) surface in both height (left) and amplitude (right) data channel showing typical artifacts.

2.2.2 Reflective high-energy electron diffraction (RHEED)

In a RHEED measurement, a beam of high energy electrons (10 to 100 keV) are incident on the sample surface at a glazing angle of 1 to 2° [29]. The electrons do not penetrate deep into the sample at such an angle. The diffraction is essentially only from the 2D lattice on the surface.

During MBE growth, RHEED can be used to monitor surface reconstructions by observing the diffraction patterns. As shown in Fig. 2-5 (a), the diffraction pattern of a smooth surface consists of a group of parallel streaks. The case (b) shows the RHEED pattern when 3D islands are formed on the surface. The change from a streaky to a spotty pattern is a clear signature of the formation of QDs when growing InAs on GaAs. For a rough surface, the pattern is often a mixture of streaks and dots.

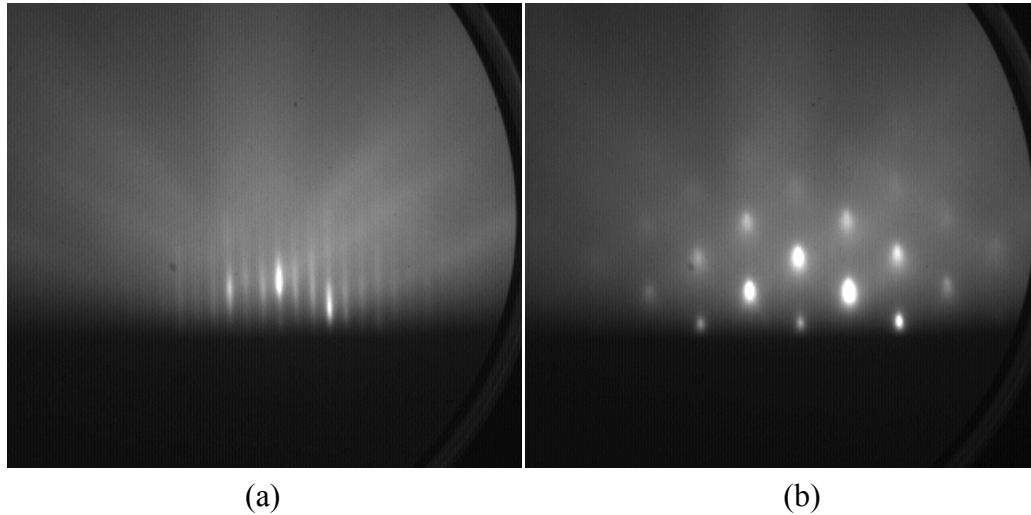


Figure 2-5. RHEED diffraction patterns of a smooth (a) and a rough surface with 3D islands (b).

RHEED can also be used to calibrate the growth rate in MBE. When measuring intensity of a beam spot of the diffraction pattern, it oscillates during the film growth. When the surface is covered by a fraction of a monolayer, part of the diffracted electrons will be scattered leading to a decrease of the intensity received by the detector. The amount of scattered electrons is proportional to the coverage of adatoms on surface. When a full monolayer is deposited, the intensity will go back to the maximum. Therefore the period of this oscillation corresponds to the time to grow one monolayer of the material, and the growth rate can be calculated subsequently. Practically, the amplitude of the oscillation decays with the film thickness due to the surface roughening [30], but this does not affect the periodicity.

Figure 2-6 (a) shows an example of GaSb grown on GaSb. Usually, the growth rate of AlAs is calibrated with the aid of GaAs, as shown in Fig. 2-6 (b), due to the rapid surface roughening if AlAs is grown alone.

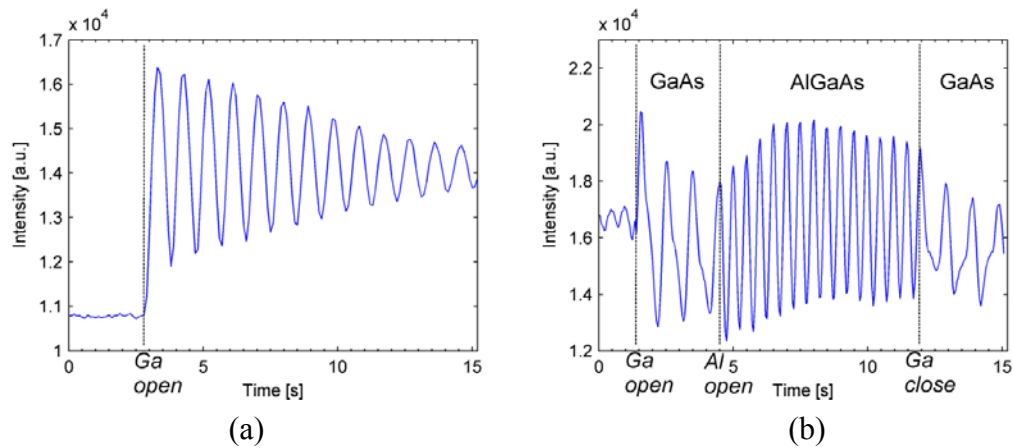


Figure 2-6. RHEED intensity oscillation of (a) GaSb grown on GaSb, and (b) GaAs/AlGaAs grown on GaAs.

2.3 Structural characterization

2.3.1 Transmission electron microscopy (TEM)

TEM is a characterization technique allowing for direct vision of a sample structure. Layers with different compositions and interfaces, line and plane defects can be seen by different contrasts in TEM images.

Electrons are accelerated to a very high energy, typically 200 keV, and focused by electromagnetic lenses onto a specimen. Some of the electrons are scattered by collisions with atoms in the crystal lattice when passing through the sample. The diffraction pattern is an array of bright spots corresponding to the reciprocal lattice as shown in Fig. 2-7. By inserting an aperture in the diffraction plane, a particular diffracted beam can be selected to view an image. If the beam transmitted directly through the sample is chosen, a bright-field image can be obtained. Otherwise, by selecting one of the diffracted beam spots, a dark-field image is achieved. In a bright field image, the regular crystal lattice appears as a bright background while the defects, such as dislocations, are dark due to strong scattering of the electrons. Fig. 2-8 shows an example of a bright field cross-sectional TEM (XTEM) image.

TEM is intensively used for characterizations of metamorphic samples. Dislocations and their distribution can be clearly revealed. We can estimate the threading dislocation (TD) density by counting the number of TDs in large scale XTEM images. Limited by the sample preparation the minimal detectable TD density is in the order of 10^6 - 10^7 /cm².

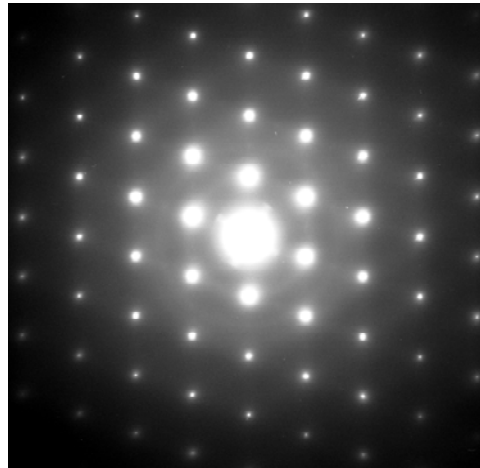


Figure 2-7. Electron diffraction pattern from a metamorphic structure observed in TEM.

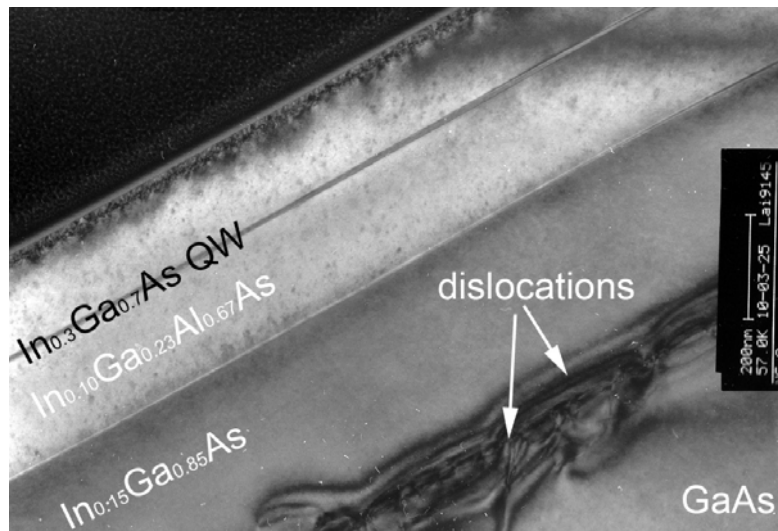


Figure 2-8. A bright field cross-sectional TEM image of a QW structure on a uniform InGaAs metamorphic buffer grown on a GaAs substrate.

Since the electrons can't penetrate too deep into a crystal, the specimen should be made very thin, typically around 100 nm. Therefore, specimen preparation is crucial for obtaining high quality images and is very time consuming. Figure 2-9 shows the major preparation steps in which a focused ion-beam (FIB) source is employed to cut a slice of material.

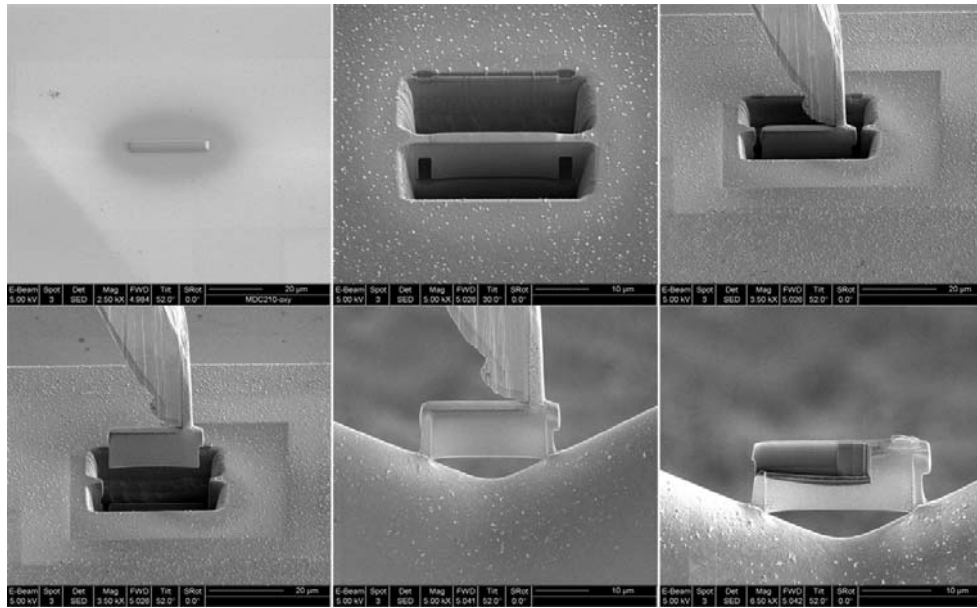


Figure 2-9. Specimen preparation for TEM. From upper-left to lower-right, the steps are: deposition of a platinum protection layer; etching by FIB to produce a slice; sealing of a tungsten tip to the slice and breaking the rest connections by FIB; taking out the specimen, sealing the specimen to a copper grid; thinning down layer by layer by FIB until reaching a thickness of about 100 nm.

2.3.2 X-ray diffraction (XRD)

XRD is a very useful tool for determining structural properties. It is a non-destructive method with a high precision and less time consuming compared with TEM. The basic underlying physics is the Bragg diffraction. Figure 2-10 shows the geometry of different angles used in the XRD measurement.

There are three angles that must be optimized before a real measurement. The first one is ω which is the angle between the incident X-ray beam and the sample surface. The second one is ϕ which is the angle between the in-plane crystal direction and the plane formed by the incident and the diffracted beams. The last one, ψ , is the tilting angle of the sample surface to the sample holder normal. The ω -value is theoretically determined when a crystal plane is chosen. It can deviate up to 2° caused by the crystal misorientation in a real measurement for non-off cut substrates. The other two angles should be 0° if the sample is perfectly mounted. These angles are very sensitive to diffraction peak positions and intensity and must be carefully optimized. The procedure is first to find out the rough position of ω and then optimize ϕ and ψ one by one. They are not independent and an iterative optimization procedure is necessary.

Rocking curve is the most common measurement for characterization of metamorphic samples. This is done by carrying out a ω - 2θ scan. The 2θ is the angle between the incident and the diffracted beams and the χ is the offset between

ω and θ . In the ω - 2θ scan, ω and 2θ change simultaneously while the χ is kept constant.

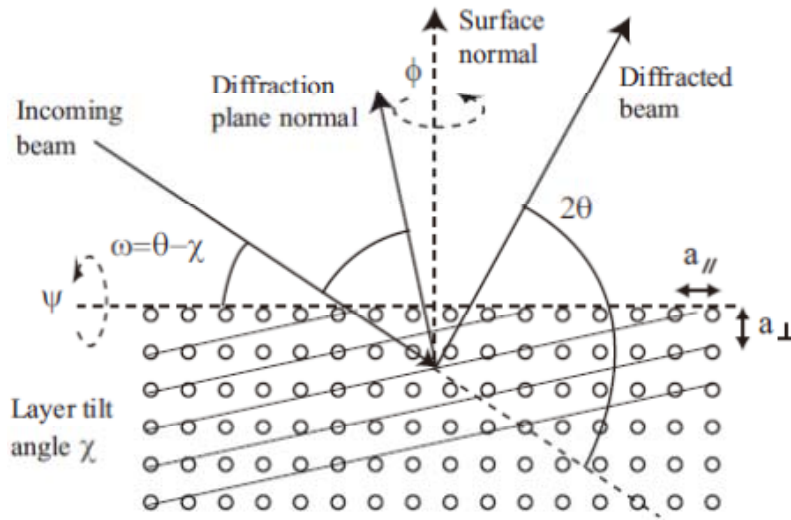


Figure 2-10. The geometry for the (115) plane asymmetric X-ray diffraction [31].

A typical rocking curve of a metamorphic structure is shown in Fig. 2-11. The different peak positions indicate different lattice constants along the growth direction. For a pseudomorphic layer, one rocking curve from a symmetric (004) plane is sufficient to obtain all the information since the lateral lattice constant is the same as that of the substrate. For a relaxed structure, by measuring a series of scans on asymmetric planes, commonly the (115) and the $(11\bar{5})$ planes, both the lateral and the vertical lattice constants can be obtained. The fully relaxed lattice constant can then be calculated from these two values based on elastic theories. If we know the elements of the layer, for example $\text{In}_x\text{Ga}_{1-x}\text{As}$, then the compositions of the elements can be determined by Vegard's law [32].

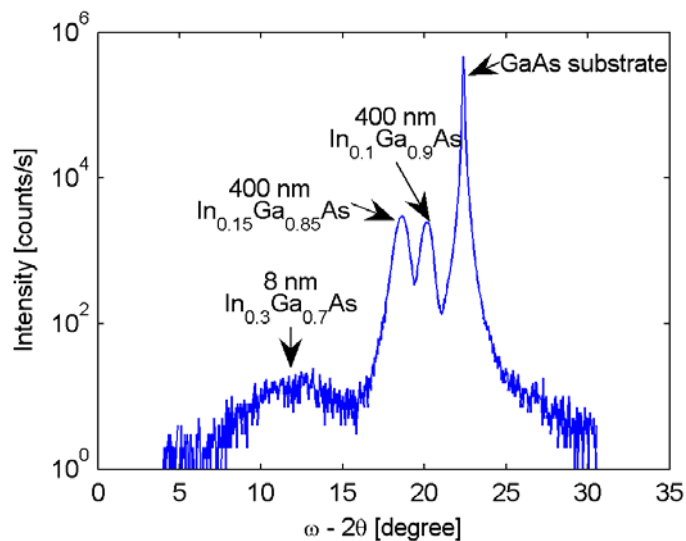


Figure 2-11. A typical (004) rocking curve of a metamorphic structure.

The above analysis is valid only for thick layers. For thin layers, theoretical simulation based on dynamic theory is necessary to fit the measured rocking curve and to extract information on thickness and alloy composition. The precision varies depending on structures and is very high for short-period SLs. As shown in Fig. 2-12 for a GaSb/AlGaSb SL, even the high order interference fringes can be matched, leading to a precision up to 0.05 nm in thickness and 0.1% in element composition. This provides alternative ways for calibration of growth rates. For a partially relaxed structure, fitting is not easy to implement unless the relaxation rate is known.

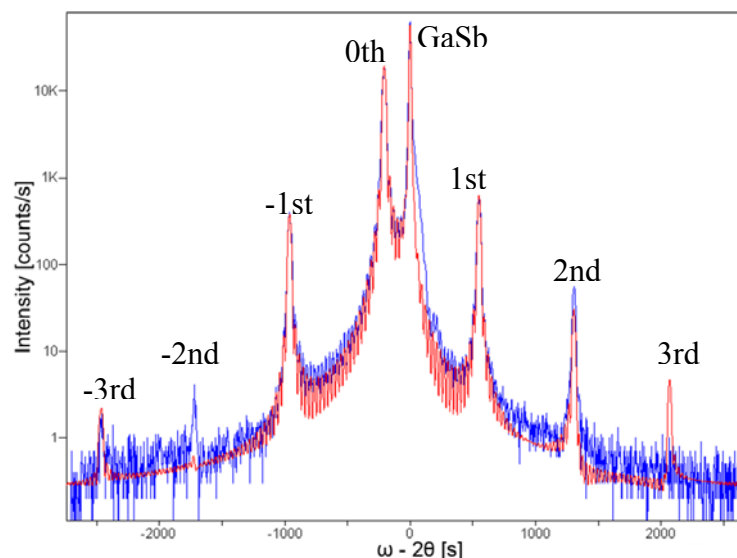


Figure 2-12. A measured (004) rocking curve of a GaSb/AlGaSb SL (blue) and the fitted curve (red). Satellite peaks are labeled.

XRD was employed as the main tool to characterize the structural properties also for T2SL materials. Figure 2-13 shows a typical XRD (004) rocking curve of a T2SL sample. The interface quality is one of the major factors for structural quality and can be quantified by measuring the full width at a half maximum (FWHM) of the diffraction fringes. The narrower the diffraction peaks, the smoother the interfaces. Moreover, the separation between the GaSb substrate (or layer) peak and the 0th order diffraction peak of the superlattice in XRD rocking curves can be used as a parameter to indicate the overall lattice mismatch of the T2SL to GaSb substrate. The thickness of one period of the superlattice can also be obtained by measuring the space between the diffraction fringes. Simulation and fitting of the XRD rocking curves for T2SLs is difficult. Because the total thickness of one period of a T2SL structure for MWIR detection is commonly less than 20 MLs, the two interfaces compose a significant portion of each period and their chemical compositions are usually unknown in simulation and have to be regarded as fitting parameters.

Strain relaxation in T2SL materials can be reflected in XRD rocking curve as well. Although the lattice constants of InAs and GaSb are very close (6.0960 vs 6.0583 Å), there is still 0.6% lattice mismatch (tensile strain for InAs grown on a GaSb substrate or buffer template) between them. Strain relaxation may occur for micrometer thick devices. An example of this can be seen in the XRD rocking curve of a sample grown on a thick GaSb buffer template on a GaAs substrate in Fig. 2-14 (a), where each superlattice peak is split into two. An XTEM image shown in Fig. 2-14 (b) confirms that the upper part of the T2SL structure is partially relaxed by nucleation of misfit dislocations (MDs). These MDs are usually accompanied by threading dislocations (TDs) terminated on the sample surface. The two sets of diffraction peaks correspond to X-ray interference from the upper relaxed and the lower strained superlattices, respectively.

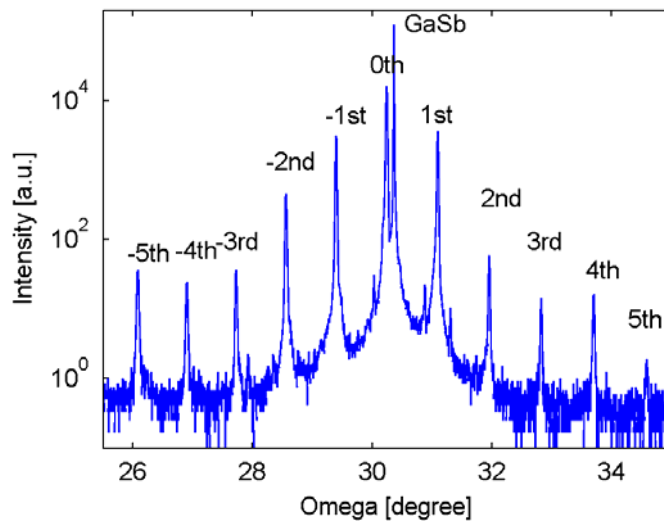


Figure 2-13. A (004) XRD rocking curve from a high quality T2SL sample.

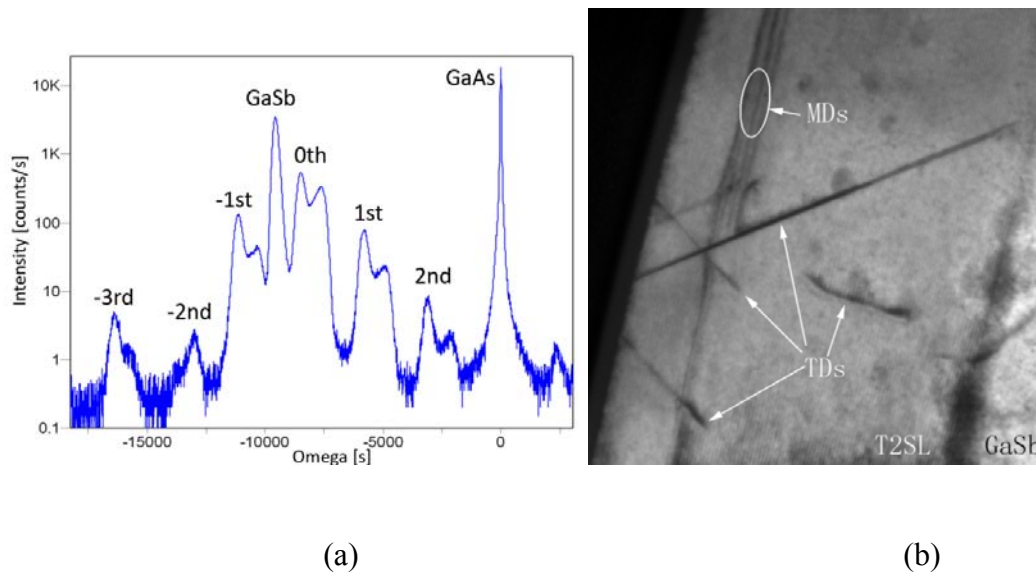


Figure 2-14. (a) An XRD rocking curve of a partially relaxed T2SL sample grown on a thick GaSb buffer template on a GaAs substrate, and (b) an XTEM image of the same sample. Both MDs and TDs are marked.

Reciprocal space mapping by XRD is another very powerful method by which all the information regarding strain and relaxation can be obtained. However this kind of measurement is very time consuming.

2.3.3 Rutherford backscattering spectroscopy (RBS)

RBS is a technique for analysis of materials that can be utilized to study element composition and depth-distribution profile, species of dopants and their density, film thickness, etc [33]. In an RBS measurement, accelerated α particles (commonly ^4He ions with energy of a few MeV) are incident on the target to be analyzed, partly backscattered through elastic collisions with the target atomic nuclei, and then captured by detectors, as illustrated in Fig. 2-14. The energy of the backscattered ions can be used to determine the mass and the depth distribution of the atoms in the target, while the counting of the backscattered particles determines the density of the atoms. The retrieval of information is commonly done by curve fitting for the measured spectra.

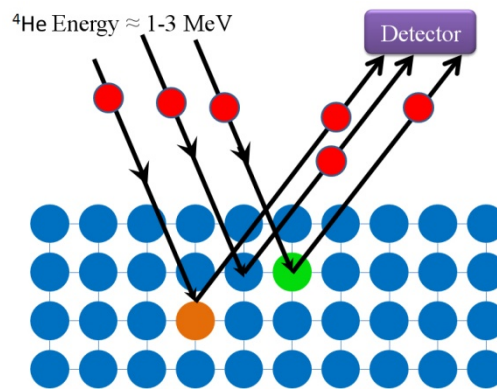


Figure 2-15. Schematic of the RBS measurement.

For a channeling RBS measurement, the incident beam of ions is aligned with a major symmetry axis of the crystal. The incident ions can then penetrate deeply into the target crystal without being backscattered, leading to a dramatic reduction of the measured backscattered signal. This measurement can help determine the regularity of the crystal structure of the target sample. One of the applications of channeling RBS is to determine whether the measured atoms are interstitial or at substitutional sites.

RBS measurements are sensitive, fast and non-destructive, and therefore widely applied for material analysis, particularly for semiconductors. We have successfully utilized RBS to demonstrate the incorporation of Bi in GaSb and InSb. A large fraction of the Bi atoms are found to be at substitutional sites, meaning that these atoms have been incorporated into the crystal lattice.

2.3.4 Secondary ion mass spectrometry (SIMS)

SIMS is a material analysis technique for determining the composition of solid surfaces and thin films. As shown in Fig. 2-16, a beam of “primary ions” are incident on the surface of the sample and transfer their energy to molecules on the surface leading to sputtering of the “secondary ions” [34]. The secondary ions which are charged are accelerated by an electric field and then collected and measured by a mass spectrometer. SIMS measurements are highly sensitive and capable of analyzing practically any ionizable elements down to a few parts-per-billion levels [35]. Compared with RBS, SIMS has higher sensitivity for element detection and high resolution in element distribution profile, but it is destructive to the measured sample.

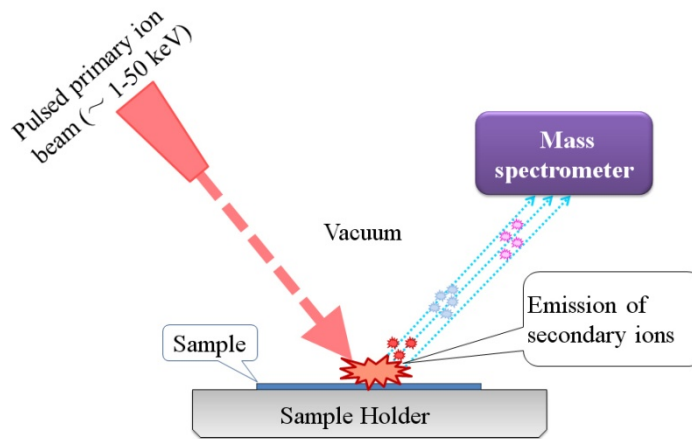


Figure 2-16. Schematic of the SIMS measurement.

SIMS measurements were carried out for our dilute bismide samples for confirmation of Bi incorporation and for studies of element distribution profiles. The measurement parameters were first optimized using a Bi_2Te_3 thin film as a reference. Oxygen and cesium ions were tested. It was found that use of negative oxygen ions with an incidence angle of 60° yields the highest sensitivity for Bi detection.

2.4 Optical characterization by Photoluminescence

Photoluminescence (PL) is one of the most widely used experimental techniques for characterizing optical property of semiconductor heterostructures. Excited by a focused laser beam with larger photon energy than the material band-gap, electrons and holes are generated. Then they can relax to low energy states, diffuse and eventually recombine either by emission of a photon or generation of heat. Through studying the emission spectrum, a wealth of information can be obtained such as the band-gap energy, energy confinement in QWs and QDs, defect levels, carrier lifetimes in time-resolved PL and so on. For metamorphic

materials, the optical property of a QW structure above a metamorphic buffer can act as an efficient indicator for the structure quality of the metamorphic buffer, while for T2SL materials, the PL intensity is another indication of the structural quality. For wavelength shorter than $1.7 \mu\text{m}$, we use a monochromator based setup which is shown in Fig. 2-17. A sample is excited by an Ar ion laser with a wavelength of 514.5 nm . Spontaneous emission is then collected and focused into a monochromator for wavelength dispersion. The PL intensity at each wavelength is measured by a liquid nitrogen cooled Ge detector. A phase-locked loop implemented by a chopper and a lock-in amplifier is utilized to improve the signal-to-noise ratio.

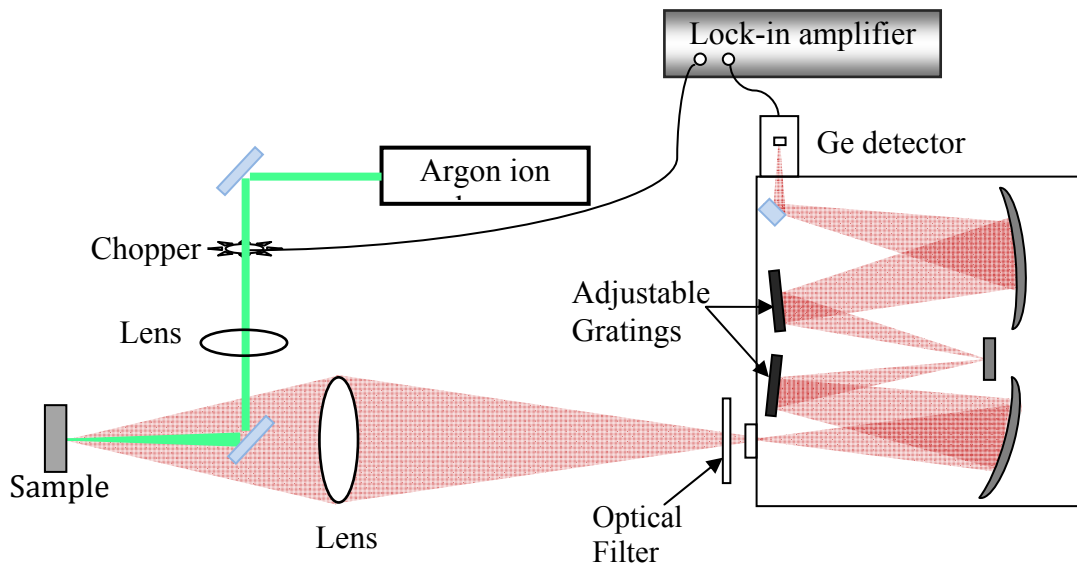


Figure 2-17. Schematic layout of the PL setup for wavelength $<1.7 \mu\text{m}$.

For longer wavelength ($>1.7 \mu\text{m}$), Fourier transform infrared spectroscopy (FTIR) is utilized to measure the spectra. Fig. 2-18 shows the setup of a FTIR for PL measurement. The sample is also excited by a laser (not shown in the figure). The emitted signal from the sample is split into two beams, which interfere with each other after reflected back from a fixed mirror and a moving mirror, respectively. The recorded interferogram is then converted into frequency domain mathematically by Fourier transformation.

The most important parameters of a PL spectrum are peak wavelength, peak intensity and full-width-at-half-maximum (FWHM). The PL intensity is a strong indicator of defect density, for example TDs in metamorphic samples and point defects in T2SL samples. These defects act as carrier traps, where electrons and holes combine very fast through a non-radiative channel. For metamorphic QWs, a high TD density will lead to weak PL intensities or no PL. The FWHM is dependent on the interface roughness and alloy non-uniformity. Figure 2-19 shows PL spectra from two identical QWs grown on two metamorphic buffers with different structural qualities.

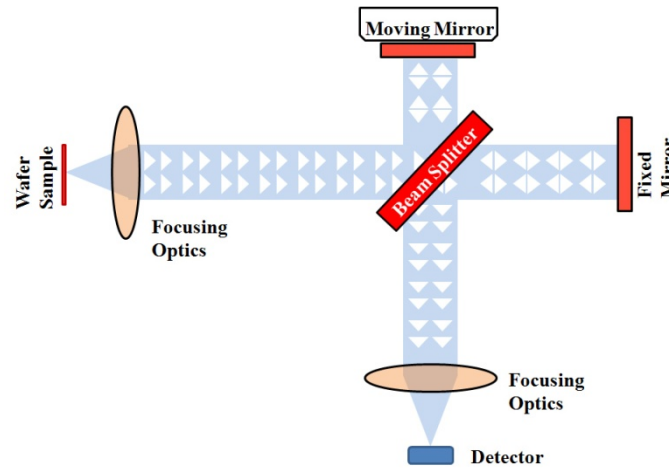


Figure 2-18. Schematic of PL measurement by FTIR.

The most important parameters of a PL spectrum are peak wavelength, peak intensity and full-width-at-half-maximum (FWHM). The PL intensity is a strong indicator of defect density, for example TDs in metamorphic samples and point defects in T2SL samples. These defects act as carrier traps, where electrons and holes combine very fast through a non-radiative channel. For metamorphic QWs, a high TD density will lead to weak PL intensities or no PL. The FWHM is dependent on the interface roughness and alloy non-uniformity. Figure 2-19 shows PL spectra from two identical QWs grown on two metamorphic buffers with different structural qualities.

PL for T2SL materials were carried out at 77 K, with the aim of examining the band-gap energy as well as the optical quality.

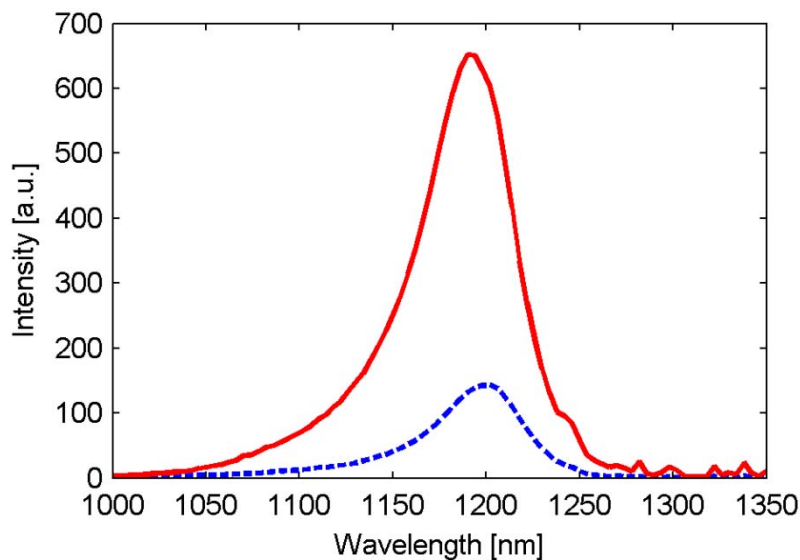


Figure 2-19. PL spectra of $\text{In}_{0.3}\text{Ga}_{0.7}\text{As}$ QWs grown on two different metamorphic buffers on GaAs: a uniform $\text{In}_{0.15}\text{Ga}_{0.85}\text{As}$ buffer (blue dashed line) and a strain compensated $\text{GaAs}/\text{In}_{0.3}\text{Ga}_{0.7}\text{As}$ SL buffer (red solid line).

3 Metamorphic technology

3.1 Introduction

The proposal and realization of the concept “semiconductor heterostructures” was revolutionary in electronics and optoelectronics and paved the road to the fast development of information and communication technology nowadays [36]. The epitaxy of heterostructures has already become a common technology for semiconductor industry. Modern heteroepitaxy methods, namely molecular beam epitaxy (MBE) and metal-organic vapor phase epitaxy (MOVPE), provide a great freedom on designing heterostructures. However, at a very high evolution pace, the freedom soon meets some practical limitations, the most crucial one of being lattice mismatch as heterostructures must be epitaxially grown on substrates of a similar lattice constant, large wafer size, low crystal defects and reasonable prices. If a thin crystal layer is grown onto a substrate with a different lattice constant, the atoms in the epi-layer will be forced to align with the lattice below at the initial growth [37]. This phenomenon is called pseudomorphic growth and the epi-layer is fully strained in this case. The strain force or energy will be accumulated while the epi-layer is growing thick until a critical point [38], at which the strain starts to relieve by formation of three-dimensional (3D) islands on the growth front for large lattice mismatch or misfit dislocations (MDs) inside the crystal for small lattice mismatch. The MDs are often in the form of section of lines lying at the epi-layer/substrate interface leaving threading components called threading dislocations (TDs) penetrating through subsequent heterostructures. In most cases, TDs have an adverse effect for optoelectronic devices.

As shown in Figure 1-2, commercial substrates are usually binary compounds or single elements. This restriction allows for only those materials with a lattice constant very close to that of substrate to be employed as building blocks for heterostructures and devices. Taking GaAs or InP substrates for instance, only the combinations within the grey area, limited by the critical thickness, can be chosen to design devices. For example, a 1.3 μm pseudomorphic $\text{In}_x\text{Ga}_{1-x}\text{As}$ QW laser on GaAs requires a minimum In composition of 45.5%, but the corresponding critical thickness is only 3 nm making such a laser on a GaAs substrate impossible [39]. There are also other practical applications requiring the solutions to the lattice mismatch problem, for example, Ga(Al)N growth for visible and ultraviolet light emission [40], uncooled telecom lasers on GaAs [41][42], integration of GaAs and/Si based devices [43–50] and multiple junction solar cells [10], [51], [52] etc.

Many techniques have been proposed to overcome the lattice mismatch problem such as compliant substrates [53–55], patterned substrate epitaxy [56], wafer bonding [57] and metamorphic growth. All the techniques except the last one require processes steps either before or after epitaxial growth and thus increasing

complexity. Metamorphic growth is a monolithic method involving no processes and can be repeatedly used if needed. In this approach, a thick buffer layer, by either step-grading or alloy-grading, is grown on a commercial substrate to relax most of the strain followed by growth of a virtual substrate or template with a desired lattice constant and acceptable surface and structural quality. The metamorphic growth is very effective for templates with small and medium lattice mismatch respect to the substrate. For large lattice mismatch and under special growth conditions, a high quality template can be grown directly on a substrate without any buffer using the interfacial misfit (IMF) method which works very well for example for InAs/GaAs [58], GaSb/GaAs [59] and AlSb/Si [60] etc..

After the first experiments with the idea of metamorphic growth in the 1970s and 80s [61], [62], there have been extensive studies in both metamorphic electronic and optoelectronic devices. However only metamorphic HEMTs were found to be compatible with those based on InP [63], [64], [65] and have been commercialized in the late 1990s. HEMT is a small device in which the distance between a source and a drain is of μm , making it possible to tolerate a moderate TD density. Most optoelectronic devices are considerably large in size ($>10 \mu\text{m}$), and thus require a much lower TD density to function. Our group has been working on metamorphic QW lasers at telecom wavelengths since 2003 and has made remarkable breakthroughs including demonstrations of the world first $1.34 \mu\text{m}$ InGaAs QW lasers under continuous wave excitation [66] and $1.58 \mu\text{m}$ metamorphic InGaAs QW lasers at room temperature [67] in collaboration with Institute of Semiconductors, Chinese Academy of Sciences, China.

Use of an alloy graded buffer is one of the most successful metamorphic growth schemes and has been extensively investigated for several material combinations such as InGaAs on GaAs [68], [69], SiGe on Si [70], AlGaAsSb on GaAs [71], InGaP on GaAs [72] and GaAs on Si [73]. By continuously changing alloy compositions in the buffer layer, most TDs are bent and confined in the bottom part of the buffer layer leaving a nearly dislocation free virtual template with a desired lattice constant. In our previous work we have found that doping in a graded buffer, which is necessary for metamorphic lasers and solar cells, can have strong influences on both surface morphology and structural properties of the metamorphic template. The device architecture and process complexity are highly related to whether the device structure will be grown on semi-insulating or highly doped substrates. It is therefore important to study the interplays between doping and alloy grading schemes on metamorphic template quality to find out optimal buffer designs. Even if the metamorphic buffer design is optimized, further reduction of TDs in the device active layers using novel dislocation blocking or filtering techniques is beneficial to improve material as well as device quality.

In this chapter, I will first introduce some basic knowledge on strain relaxation and structural defects in metamorphic buffers. The study of the doping effect on buffer quality with different alloy grading profiles and grading slopes will be then

presented. Finally a novel method for TD blocking employing dilute nitrides will be described.

3.2 Strain relaxation in III-V semiconductors

3.2.1 Lattice mismatch and strain

When a thin crystal film is epitaxially grown on a substrate, the lattice of atoms in the epi-layer tends to align with that in the substrate if the epi-layer thickness is much smaller than that of the substrate (typically 300 μm). In the ideal case, the two lattices will align perfectly in the lateral directions through biaxial deformation of the epi-layer, leading to compressive strain if the epi-layer has a larger lattice constant compared with the one in the substrate or tensile strain in the opposite case. Lattice mismatch is defined as the relative difference in percentage between the two bulk lattice constants.

Strain provides some freedoms to tailor-make the energy band structure and carrier transport, and thus plays an important role in heterostructure devices. Strain energy is accumulated when the structure is growing thick, and strain relaxation highly depends on the lattice mismatch and growth conditions. While strain relaxation often generates deleterious structural defects in pseudomorphic heterostructures which degrade device performances, it can also be utilized. The most significant example is the self-assembled QDs which are formed by nucleation and coalescence of 3D “islands” via the Stranski-Krastanov [74] growth mode. QDs have been successfully used in many kinds of devices such as solar cells [75], light emitting diodes [76] and diode lasers [77] etc. Another example is metamorphic growth, the main topic of this chapter. In metamorphic buffers, strain relaxation by formation of MDs is required in a controlled manner to minimize surface roughness and the density of TDs.

3.2.2 Strain relaxation

Strain in heterostructures can be relaxed in many different ways such as formation of 3D islands, formation and propagation of dislocations, cracks, and coherent elastic deformation, etc. All these are related and compete with each other.

Formation of 3D islands

Strain can be relaxed by means of increasing surface area to form 3D islands (also called QDs if their size is in nm scale) if the increase of the surface energy is smaller than the relief of the strain energy. This happens when the lattice mismatch is large. Figure 3-1 (a) shows the simulation of the in-plane strain of a lens shaped $\text{In}_{0.5}\text{Ga}_{0.5}\text{As}$ island growing on a GaAs substrate using finite element method (FEM). The strain relaxation in 3D islands is incomplete and non-uniform: the top part of the island is mostly relaxed while the edge of the island is highly strained,

in consistent with the experiments [78]. If the size of the island is large enough, the residual strain in the island will be further relaxed by formation of MDs. For $\text{In}_x\text{Ga}_{1-x}\text{As}$ grown on a GaAs substrate, the critical In composition for onset of formation of 3D islands is around 25-30% which has lattice mismatch of about 2% [39].

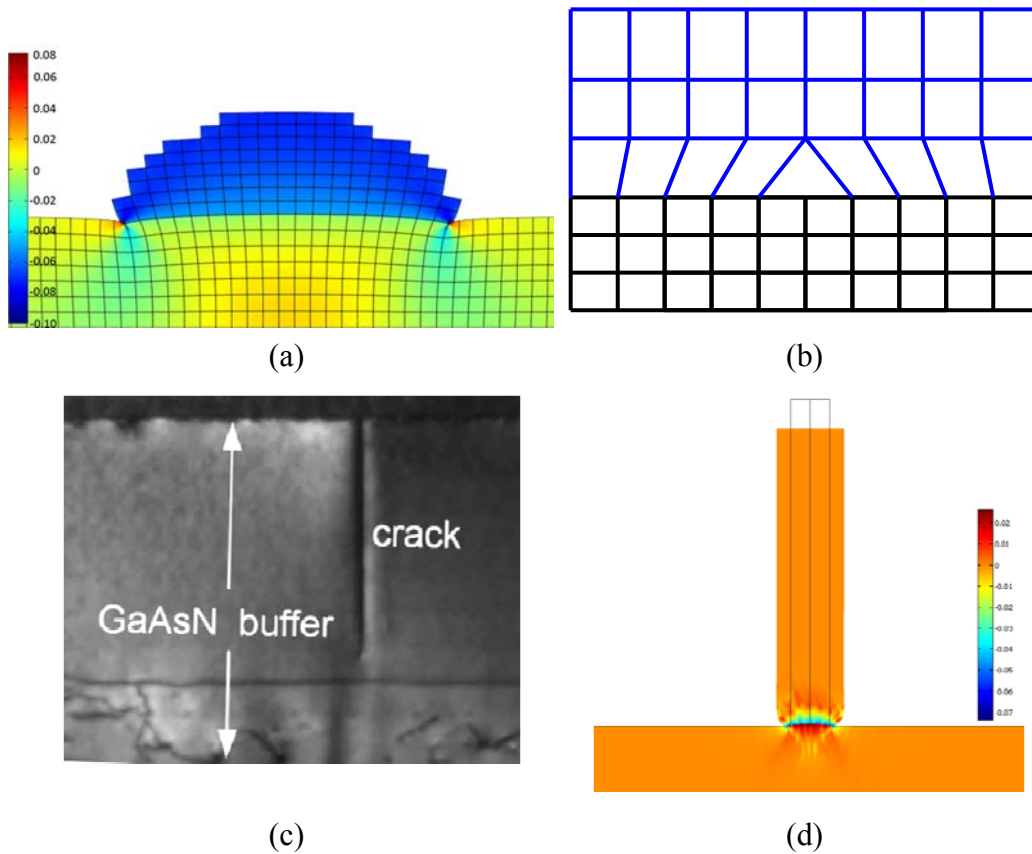


Figure 3-1. Ways of strain relaxation. (a) FEM simulation of coherent strain relaxation in a compressively-strained $\text{In}_{0.5}\text{Ga}_{0.5}\text{As}$ 3D island on a GaAs substrate. The color indicates the value of the in-plane strain. The deformation is 2 times exaggerated. (b) Schematic of a MD in a heterostructure. (c) Cross-sectional TEM image of a crack in a GaAsN buffer grown on GaAs. (d) In-plane strain distribution of a relaxed 30 nm radius InAs nanowire grown on GaAs simulated by FEM. The black frame is the original shape without relaxation. The deformation is 10 times exaggerated. The color indicates the value of the in-plane strain.

Misfit dislocations

For lattice mismatched heterostructures with relatively small lattice mismatch ($<2\%$), strain tends to be relaxed by formation of MDs at the critical thickness. Figure 3-1 (b) shows a schematic of a MD generated in a compressively strained epi-layer in which one row of the bonds are missing at the interface, allowing for

the lattice of the epi-layer to slightly stretch towards its original size and thus releasing part of the strain. Effective strain relaxation occurs via formation of a network of orthogonal MDs. Practically, a dislocation is hardly as simple as is illustrated in Fig. 3-1 (b). Dislocations in diamond and zincblende (001) heteroepitaxial layers will be discussed in detail in the next section.

Cracks

Cracks can occur during the cooling process when the epi-layer has a larger thermal expansion coefficient than that of the substrate, i.e. due to the thermal mismatch. They may also show up in a tensile strained epi-layer as a competing mechanism against formation of MDs. Crack is a common problem in III-nitride materials [79] but also in other III-V materials for example when InGaAs grown on InP [74, 75]. Figure 3-1 (c) shows an example of a crack formed in a GaAsN buffer grown on GaAs [72].

Coherent elastic deformation

Strain relaxation through coherent elastic deformation could become significant in nano-scale structures like nanowires or near the edges of the epi-layer grown on a patterned substrate. Figure 3-1 (d) shows an example of the lateral residual strain from a 500 nm long InAs nanowire with a radius of 30 nm grown on a GaAs substrate simulated by FEM. As seen, the nanowire expands laterally and contracts vertically. The majority upper part of the nanowire is almost strain free. This kind of strain relaxation can be so efficient such that, if the diameter of a nanowire is sufficiently small, it can be grown infinitely long without any MDs [82].

3.2.3 Dislocations in zincblende crystals

In zincblende (001) heteroepitaxial layers, most MDs are 60° type dislocations with a Burgers vector 60° away from the MDs lying along the orthogonal $[110]$ and $[\bar{1}10]$ directions as sketched in Fig. 3-2 (a). This type of MDs has a mixture of screw and edge dislocation components and is not as efficient as pure 90° edge MDs for strain relaxation. 60° type MDs are often connected by one or two TDs that can thread through the whole structure and terminate at the surface. Therefore it is essential to suppress TDs in a metamorphic structure.

There are several sources of generating MDs such as bending of existing TDs from the substrate, homogeneous and heterogeneous nucleation and gliding of dislocation half loops and dislocation multiplications etc. Nowadays, commercial substrates have an etch pit density down to 10^3 cm^{-2} or lower. The bending of existing TDs from the substrate is therefore not enough to relax the strain. It is calculated that homogeneous nucleation of dislocation half-loops in InGaAs on GaAs occurs only for large lattice mismatch $>2\text{-}6\%$ depending on the selected dislocation core values [83]. The dislocation multiplication is unlikely to happen at the initial strain relaxation. It is generally accepted that the dominant strain

relaxation mechanism in InGaAs epi-layers grown on GaAs is heterogeneous nucleation of dislocation half loops on the surface as shown in Fig. 3-2 (b).

Dislocation half loops first nucleate at the growth front, then glide toward the interface in the (111) plane and relax part of the strain from the surface through the epi-layer. The gliding process eventually stops at the interface between the uniform epi-layer and the substrate to form a MD segment and two TDs, or at the position where the strain force is balanced by the dislocation line tension and the Peierls–Nabarro friction force in an alloy graded buffer [84]. The two TDs can still glide laterally until meeting strong impedances or being annihilated. For InGaAs grown on a GaAs (001) substrate, the MDs lie in the $[1\bar{1}0]$ and the $[110]$ directions (called α and β dislocations, respectively) [50, 51], forming a grid of dislocation lines at the interface. Figure 3-3 (a) [86] shows an in-plane TEM photo of a MD grid. The MDs cause strain non-uniformity at the growth front, which induces preferential deposition of the impinging Ga and In atoms and thus thickness and alloy fluctuations [87].

In order to reduce the TD density, the average length of MD segments should be as long as possible. Gliding of TDs increases the length of MD segments. So it would be wonderful if all the TDs can glide all the way to the edge of the sample. However, most of them are stopped after interacting with other MDs or TDs, or pinned by point defects in the crystal. When two MDs or TDs meet, there are several possible ways of interactions and Fig. 3-3 shows a few examples. The most interesting case is that when two TDs with anti-parallel Burgers vectors meet they will annihilate leaving a MD.

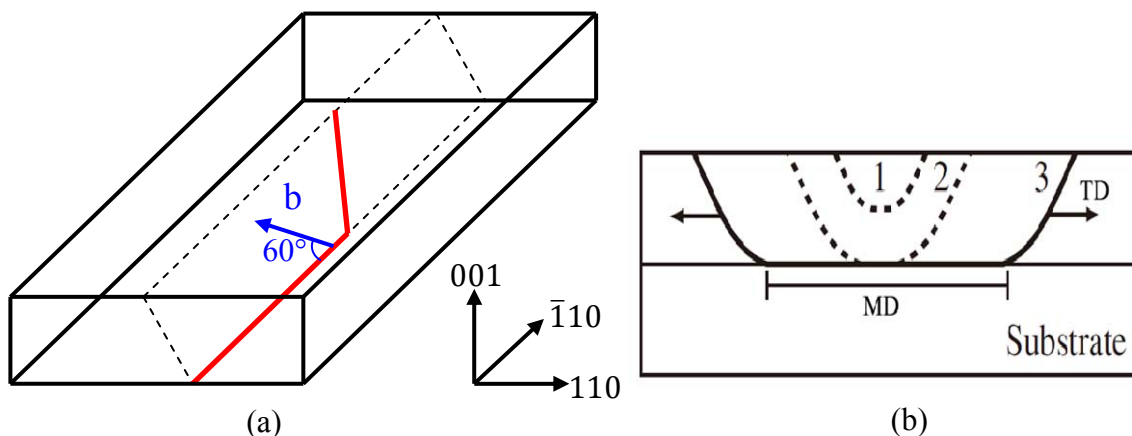


Figure 3-2. (a) Geometrical illustration of a 60° dislocation in zincblende crystals. (b) Illustration of the formation and gliding of a dislocation half loop in a uniform epi-layer.

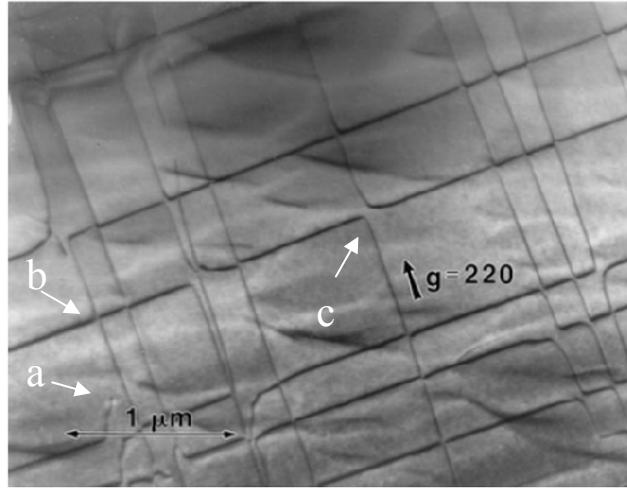


Figure 3-3. A MD grid at the interface of $\text{In}_{0.027}\text{Ga}_{0.973}\text{As}/\text{GaAs}$ revealed by bright field planar-view TEM. Reproduced from reference[86] by permission of the author T. Wosinski. (a) indicates a TD. Two situations when MDs meets without (b) and with interaction (c) are indicated.

3.3 Alloy-graded metamorphic buffer layers and doping effect

In a uniform thick buffer, strain relaxation is realized by gliding of dislocation half-loops from surface to the buffer/substrate interface forming MDs as well as a large amount of TDs. Dislocation interactions are also functioning to replicate more MDs and TDs if their densities are high. The TD density decreases with the buffer thickness, h , at the scaling of $1/h$ for a TD density $>10^7 \text{ cm}^{-2}$ and of $e^{-\alpha h}$, where α being a constant, when the TD density is $<10^7 \text{ cm}^{-2}$ [88]. For GaAs/Si as example, it was experimentally found that the TD density decreased from initially 10^9 cm^{-2} to $2.2 \times 10^7 \text{ cm}^{-2}$ and $7 \times 10^6 \text{ cm}^{-2}$ for 10 and 60 μm thick GaAs, respectively. Use of an alloy graded buffer is much more effective in reducing the TDs. By continuously changing the alloy composition in the buffer layer, TDs can be effectively bent by the increased or decreased strain force and confined in the bottom part of the buffer layer leaving a fully strained top layer which acts as a virtual template with a desired lattice constant. The TD density can be easily reduced to 10^7 cm^{-2} by a $\sim 1 \mu\text{m}$ alloy graded buffer.

For metamorphic optoelectronic devices where back-contacts on conductive substrates are often used, it is necessary to dope the metamorphic buffer to lead the current through the device. We have found that different types of dopants in alloy graded InGaAs metamorphic buffers have a significant effect on structural properties and surface morphology [89]. The easiest way to realize an alloy graded buffer during MBE growth is to linearly ramp the In and/or Ga source temperatures. Since the beam flux depends exponentially on the source temperature, the actual alloy profile following a *linear source temperature grading* (LTG) is a super-linear curve with a slow increase of the alloy composition

initially and a fast increase at the end. Therefore alloy grading profile is an important parameter for buffer optimization. In this thesis, three grading profiles as shown in Fig. 3-4 are discussed. In addition to the LTG, the second is a truly *linear alloy grading* (LAG) and the last one is essentially a *mirror image* of the LTG (M-LTG) profile with respect to the LAG showing a sub-linear curve, both

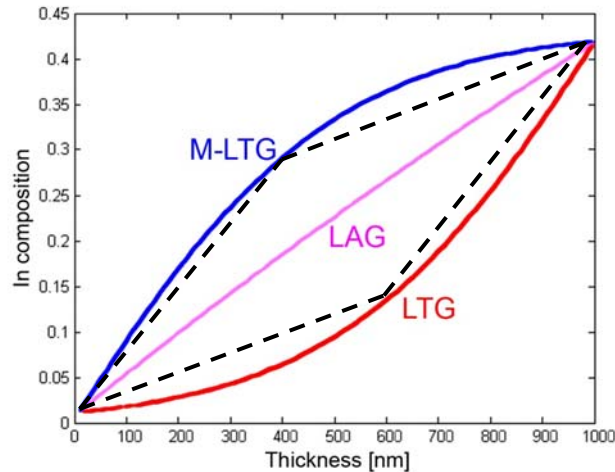


Figure 3-4. Three alloy grading profiles of InGaAs on GaAs studied in the thesis. The broken lines illustrate approximation of the LTG and M_LTG profiles into two LAG with different slopes.

produced by a carefully designed source temperature ramping program to compensate the exponential temperature dependence. The LTG can be approximated as superposition of two LAG profiles: an initial small grading slope LAG and a final large grading slope LAG, while the M-LTG has the opposite situation. As will be discussed below, In segregation is highly dependent on the grading slope and is responsible for final surface and structural properties of a metamorphic buffer. This motivates that the grading slope should be considered as an independent parameter for buffer optimization.

3.3.1 Strain relaxation in alloy graded buffer layers

Strain relaxation process and dislocation kinetics are different in continuous alloy grading compared with the case of a uniform buffer. In the former case, the major mechanism of the TD reduction is bending of TDs to form MDs. The differential change in lattice mismatch ensures that the generated MDs can distribute at any place in the buffer rather than being confined only at the interface in the uniform buffer. Hence, the chance for a MD to be pinned by another MD running along the orthogonal direction is much smaller in the alloy grading case and a TD can glide for a long distance and has a large probability to be annihilated by other TDs with opposite Burgers vectors [68, 69]. Below I summarize some common features found in alloy graded metamorphic buffers based on our own experiments. All the metamorphic buffers were grown at 380 °C read by the thermocouple using MBE.

“Dislocation-free” region and residual strain

Figure 3-5 shows an XTEM image of an LAG $\text{In}_x\text{Ga}_{1-x}\text{As}$ buffer with $x=0-0.42$. A clear boundary (marked by the broken line) can be found in the image leaving a nearly “dislocation-free” region above it. This phenomenon was predicted by J. Tersoff [91]. In his model, the equilibrium distribution of dislocations and residual strain in an alloy graded buffer were calculated by minimizing the total energy (strain energy plus dislocation energy). Theoretically, at the equilibrium, the part below this boundary is fully relaxed while the upper “dislocation-free” region is fully strained. With increasing the alloy grading rate (thus also of the lattice mismatch), the thickness of the “dislocation-free” region decreases while the residual strain in the upper part of the buffer increases. Taking the LAG profile as an example, the thickness of the “dislocation-free” region, h , can be expressed by

$$h = \sqrt{2\lambda/bc\epsilon'} \quad (3-1)$$

and the residual strain, $\bar{\epsilon}$, is

$$\bar{\epsilon} = \sqrt{2\lambda\epsilon'/bc} \quad (3-2)$$

where λ is the dislocation energy per unit length, b is the misfit component of the Burgers vector of the dislocation, c is an appropriate elastic constant for biaxial strain and ϵ' is the grading slope of the lattice mismatch. For a fixed material system, λ , b and c can be treated as constants. So the thickness of the “dislocation-free” region and the residual strain are dependent only on the grading slope. The measured thickness of the “dislocation-free” region is always smaller than the theoretical calculations by 10-40% from our measurements because the strain below the boundary is only partially relaxed due to the dislocation interactions. A thick “dislocation-free” region is found to favor the gliding of TDs resulting in long MD segments and a low TD density.

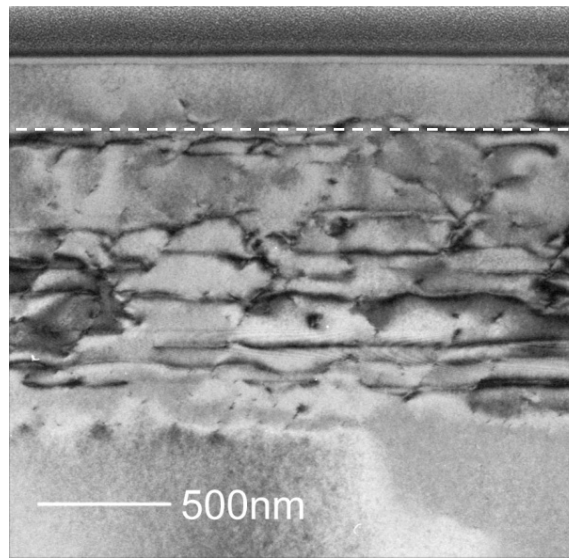


Figure 3-5. An XTEM image of an LAG $\text{In}_x\text{Ga}_{1-x}\text{As}$ buffer with $x=0-0.42$.

Step-like strain relaxation

Another phenomenon found in Fig. 3-5 is that the MDs are formed at discrete levels, which indicates a step-like strain relaxation process even though the alloy grading is continuous. The Tersoff model based on equilibrium assumptions hasn't explain this phenomenon. We propose the following model. In the beginning of the growth, the epi-layer grows pseudomorphically until the thickness reaches a critical value and dislocation half-loops begin to form. The dislocation half-loops glide toward the interface and thus relax part of the strain from the surface through the epi-layer. During the downward gliding process, the residual strain, which is equal to the difference between the lattice mismatch (position dependent) and the degree of strain relaxation (constant), decreases and so does the strain force that drives the dislocation gliding. The strain force is eventually balanced by the dislocation line tension and the Peierls-Nabarro friction force [84]. The gliding is then stopped and MDs are formed. No MDs will be generated in the region where the strain force is smaller than the friction force. Now, the overall strain in the upper part of the alloy graded buffer becomes much smaller than before the relaxation. The growth continues, and new strain accumulates again. When it reaches the critical thickness, similar relaxation happens again. New MDs will be generated at the places where the new force balance is established as discussed above. Thus, the strain is relaxed by formation of MDs at discrete levels. If the gliding of TDs is impeded by some reasons, e.g. the MDs in the orthogonal direction or crystal defects, the length of MDs can be short and it is difficult to see the step-like distribution of MDs in this case.

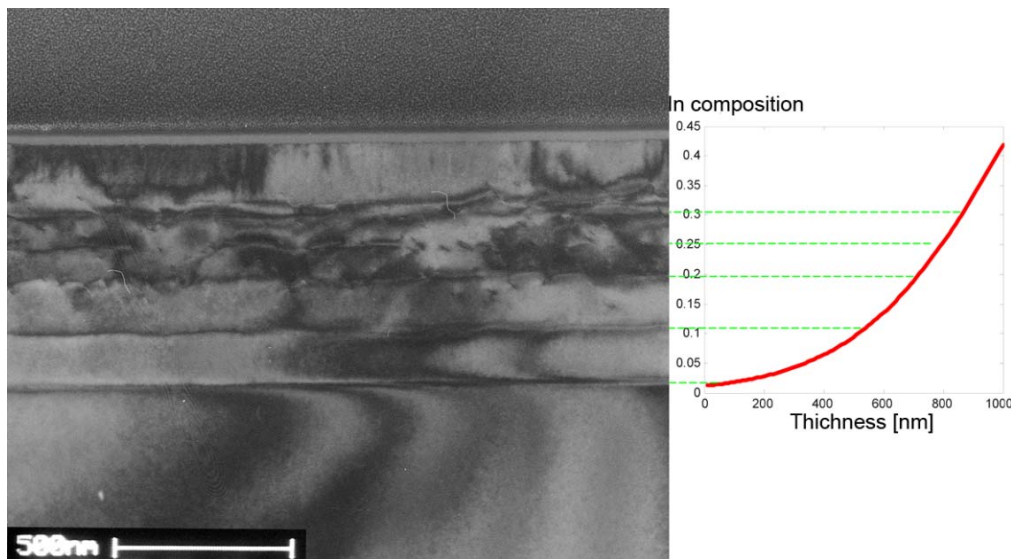


Figure 3-6. An XTEM image of an LTG $\text{In}_x\text{Ga}_{1-x}\text{As}$ layer with $x=0\sim 0.42$. The right figure shows the In grading profile.

Figure 3-6 shows another example using LTG. The In source temperature is linearly graded in this sample leading to an exponentially graded In composition shown at the right side of the figure. It can be seen that in the beginning, the grading slope is small, so it requires a large thickness to initiate the first strain

relaxation. When the grading slope becomes steeper, the space between the two neighbor MD layers turns to be smaller. This experimental finding supports our model above.

Cross-hatch surface

The cross-hatch pattern is a typical surface morphology of alloy graded buffers, shown in Fig. 3-7 as an example. The MDs underneath the surface create strain uniformity at the growth front, inducing preferential agglomeration of the impingent Ga and In atoms. Indium segregation during InGaAs growth is a well known fact [92]. As a result, excess In atoms are found on the growth surface leading to the enhanced In concentration and the lattice mismatch on the growth front. These mobile In and Ga adatoms tend to nucleate in a 3D mode resulting in formation of the cross-hatch pattern with fluctuated thickness and composition on the growth surface. The amount of In atoms and their diffusion length on an $\text{In}_x\text{Ga}_{1-x}\text{As}$ graded buffer are two important factors determining the surface morphology and structural properties.

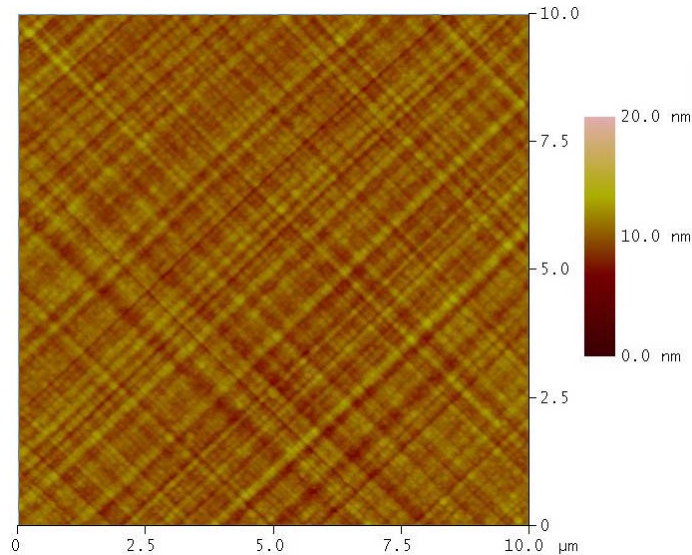


Figure 3-7. A typical cross-hatch pattern of an alloy graded InGaAs buffer on GaAs shown in a $10 \times 10 \mu\text{m}^2$ AFM scan.

J. M. Muraki *et al* proposed a model to simulate the In segregation process in uniform III-V ternary compounds based on an iterative approach [92]. We extend this model to simulate the segregation in LAG $\text{In}_x\text{Ga}_{1-x}\text{As}$ buffers and find that the amount of segregated In atoms in terms of monolayer on the growth front of an $\text{In}_x\text{Ga}_{1-x}\text{As}$ buffer, $C(h)$, with thickness, h , and In grading slop, α , is

$$C(h) = \frac{\alpha\eta}{1-\eta} h \quad (3-3)$$

where η is the segregation rate which is defined as the percentage of In atoms segregated to the surface from the underneath mono-layer. The detailed deviation is shown in Appendix A1. η is basically a constant with a typical value around 0.8

for In segregation in InGaAs. Therefore, the amount of segregated In atoms is directly proportional to the grading slope and buffer thickness.

3.3.2 Interplays between doping, grading profiles and grading slopes

Figure 3-8 shows both surface morphology and XTEM images of the undoped, the Be-doped (*p*-type) and the Si-doped (*n*-type) samples with the M-LAG profile. Both 3D islands and a cross-hatch pattern are observed for the undoped (a) and the Si-doped (c) samples but only the cross-hatch pattern is found for the Be-doped sample (b). The sequence of the root-mean-square (RMS) surface roughness value follows: (b)<(a)<(c). The 3D islands formed on the surface are directly related to the amount of segregated In atoms. Presence of 3D islands also modifies strain relaxation. Instead of forming 60° mixed type dislocations, 3D islands create strong strain inhomogeneity on the growth front leading to preferentially site selective bonding of impinging In and Ga atoms. The coalescence of 3D islands results in formation of 90° edge dislocations which are sessile and can't be eliminated. From Fig. 3-8 we observe such edge type TDs in both the undoped and the Si-doped samples while there are no TDs found in the Be-doped one.

It is observed that for Be-doped samples, the “dislocation-free” region is basically free of TDs, the boundary of the “dislocation-free” region is well defended, the MD segments are long and smooth and the step-like MD distribution is clear. The situation for the Si-doped sample is totally opposite. It is difficult to find flat MDs and the crystal lattice is strongly distorted in some parts of the buffer. There are many TDs penetrating to the surface.

The generality of the doping effect exists in all alloy grading profiles studied in this thesis while the degree is found to be dependent on the grading profile as well as the slope. Be-doping generally reduces the TD density by reducing the pinning effect and enhancing the gliding of the TDs; and can suppress the In segregation thus smoothening the growth front and avoiding formation of the edge type TDs, while the Si-doping has obviously an opposite effect. The best quality buffer is found to be Be-doped LTG, with the lowest surface roughness and the TD density. The difference between the undoped, the Be-doped and the Si-doped samples is less exhibited when an LAG profile is used. For LAG profiles, the thickness of the “dislocation-free” region and the residual strain are dependent on the grading slope while the pinning effect on dislocations is influenced by the doping. A moderate In grading (around 42% In/ μm) is preferable for strain relaxation and minimizing the negative effects on both the surface roughness and the TD density caused by the Si doping.

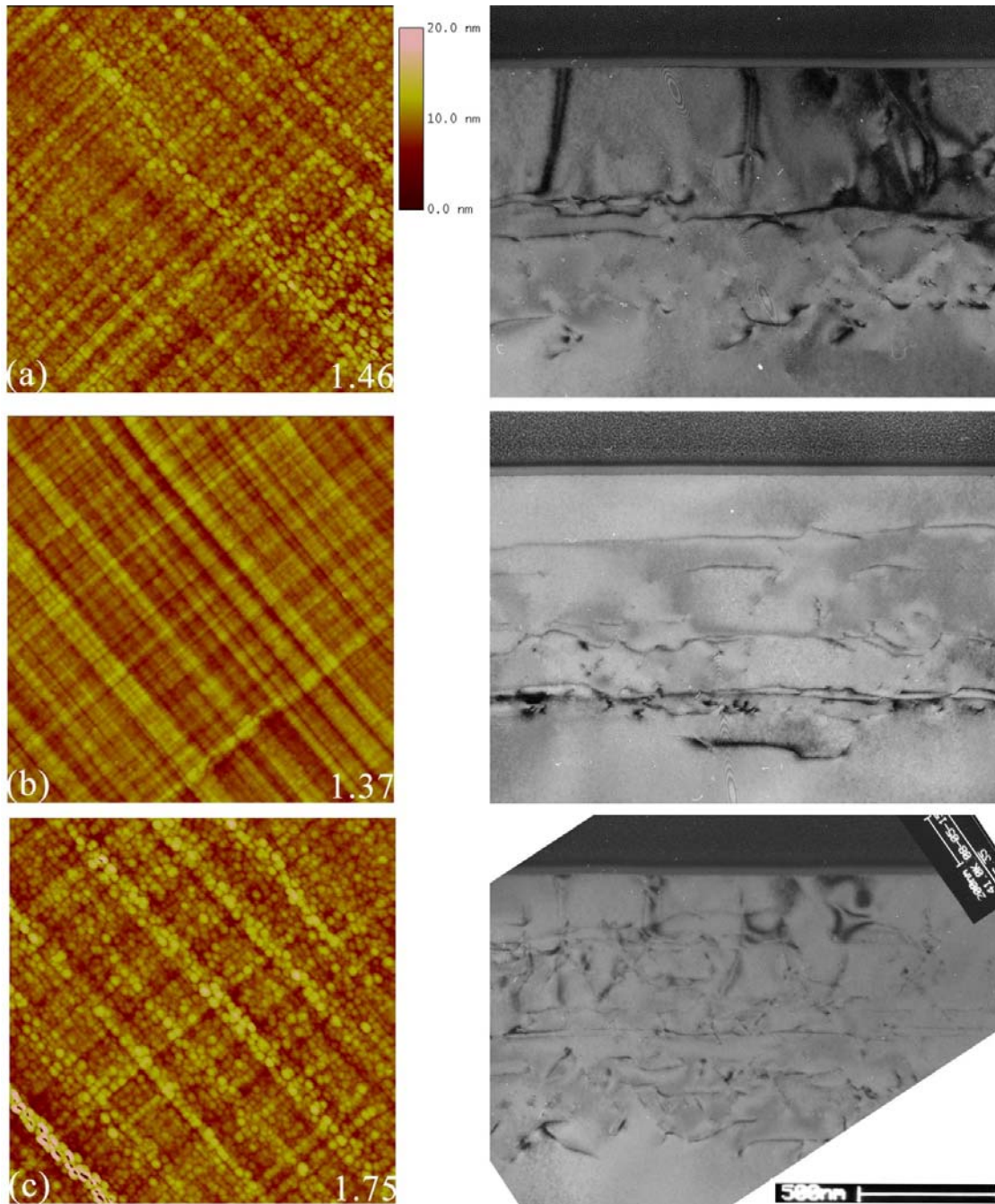


Figure 3-8. Surface morphology obtained by $10 \times 10 \mu\text{m}^2$ AFM scans (left) and XTEM images (right) of the undoped (a), the Be-doped (b) and the Si-doped (c) M-LTG $\text{In}_x\text{Ga}_{1-x}\text{As}$ buffers with $x=0\sim 0.42$. The numbers at the lower-right corner of the AFM images are the RMS roughness values in nanometer.

3.3.3 Design of alloy-graded buffers for optoelectronic devices

When considering a real optoelectronic device like laser or solar cell, current injection turns out to be an issue. Taking $\text{InGaAs}/\text{GaAs}$ edge emitting lasers for instance, the most common design is to grow the whole structure on an n -type

substrate. When it comes to metamorphic growth, the buffer layer must also be *n*-type doped. Using an LAG profile with a moderate slope can mitigate the problems related to the Si-doping to a large extent and this scheme has been used by us to demonstrate the first 1.58 μm metamorphic InGaAs QW laser at 300 K [67].

The high quality Be-doped buffer could be chosen together with a *p*-type substrate, and then the current runs in the opposite direction compared with a conventional semiconductor laser on an *n*-type substrate. The resistivity of *p*-type substrates and buffers is commonly much higher than that of the *n*-type counterparts. The Joule heating can significantly affect the temperature stability and lifetime of the devices.

Another possibility to utilize the advantage of the Be-doped buffer is to design a co-planar contact scheme for current injection on a semi-insulating substrate. In this design, the non-uniform distribution of current density could cause some problems such as local heating due to the current crowding effect. We used such a design and demonstrated 1.3 μm metamorphic InGaAs QW lasers at 300 K [66].

3.4 Threading dislocation blocking

Optimizations of alloy graded buffer design and growth conditions are essential to achieve a smooth metamorphic template with a low TD density. In the best case, the TD density can be reduced to 10^6 - 10^7 cm^{-2} , i.e. the average distance between two neighbor TDs is in the order of a few μm . This is enough for metamorphic electronic devices but still challenging for metamorphic optoelectronic devices. Further reduction of the TD density using different blocking schemes is necessary. There are several different ways to block TDs by, for example multiple QD layers, a strain compensated superlattice (SL) or using dilute nitrides as proposed in this work. These TD blocking methods alone may not be efficient, in particular if the initial TD density is low. However it is possible to combine these methods with the optimized metamorphic buffers to reach the optimal effect.

3.4.1 TD blocking through interactions with strain fields

TDs can have strong interactions with the strain field they experience [93] and possibly change the propagating directions [38]. Therefore, intentional introduction of strained structures can help reduce the TD density. There are two main methods based on this mechanism: strain compensated SL and multiple QD layers. The basic idea of both methods is utilizing the excess strain field to bend the TDs. In the strain compensated SL case, the alternate compressive and tensile strain relative to the relaxed layer below enables to push the TDs back and forth, thus increasing the chance of TD annihilation as schematically shown in Fig. 3-9

(a). This method has been proven to be effective in InGaAs on GaAs [94], GaAs on Si [95] and InP on Si [96].

Z. Mi *et al.* used multiple layers of self-organized InAs QDs as a TD filter above a GaAs buffer and demonstrated QD lasers grown on Si substrates [84, 85]. The local strain field imposed by InAs QDs on GaAs is much larger than that produced by a strained SL. When a TD meets a QD, it can be bent to form a MD segment below the QD as shown Fig. 3-9 (b). When it glides out of the QD region, it would propagate in the same direction or climb up again in the cap layer. The mechanism is still not fully understood yet. Even if the MD segment turns to be a TD segment again, it can meet another QD in the next QD layer and be bent again. Therefore the possibility for TDs to glide to the edge of the sample or annihilate with other TDs increases with increasing the number of QD layers. This scheme has also been demonstrated in GaN on sapphire substrates [99].

When the QD filter is intended to be combined with an InGaAs metamorphic buffer, some technical problems arise. The relatively rough surface of the metamorphic buffer and the smaller lattice mismatch between InAs and the relaxed InGaAs compared with that of InAs on GaAs lead to formation of large InAs QDs with a small density, thus reducing the filtering efficiency.

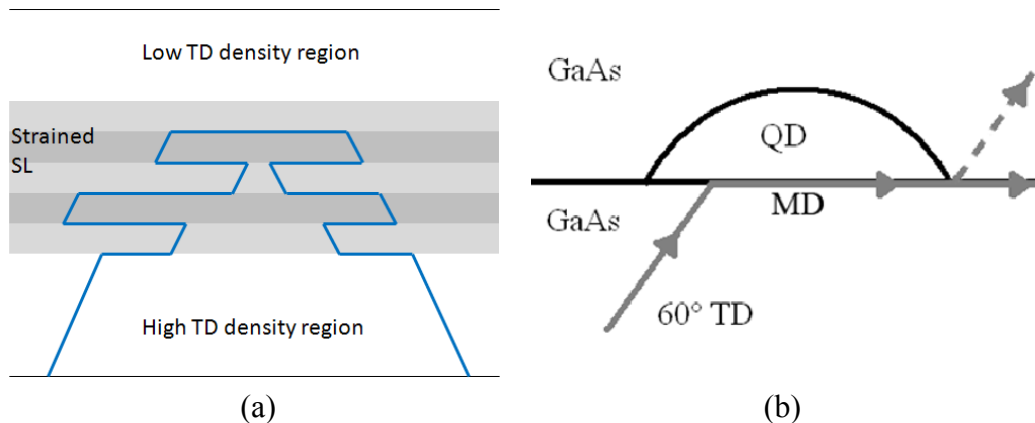


Figure 3-9. . Schematic of TD blocking methods. (a) TD blocking by a strain compensated SL. The different contrast in the SL presents alternation of strain types. (b) TD bending by a QD.

3.4.2 TD blocking by dilute nitrides

We propose a new method of TD blocking by incorporation of nitrogen in metamorphic InGaAs buffers. This method works effectively even for a metamorphic template with a small TD density. When the TD density is in 10^7 cm^{-2} or lower, TDs are hardly observed by XTEM. However, PL intensity is very sensitive to TDs at this range since the carrier diffusion length is still comparable or larger than the average spacing between TDs. Therefore PL is used to study the TD blocking effect although it is an indirect method.

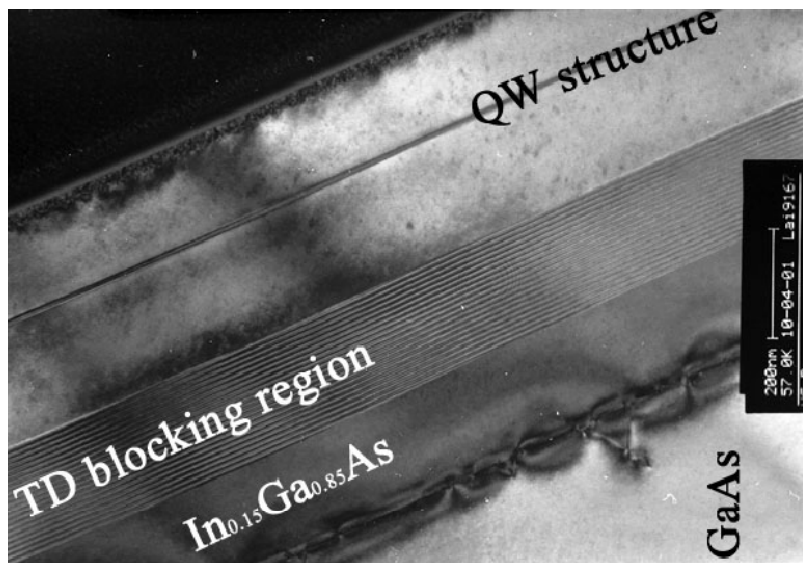


Figure 3-10. An XTEM image showing a typical sample structure containing a dilute nitride TD blocking region.

An XTEM image of a typical sample structure is shown in Fig. 3-10. By inserting N into an $\text{In}_{0.15}\text{Ga}_{0.85}\text{As}$ buffer to form an $\text{In}_{0.15}\text{Ga}_{0.85}\text{As}/\text{In}_{0.15}\text{Ga}_{0.85}\text{N}_{0.012}\text{As}_{0.988}$ SL in the TD blocking region above a 200 nm uniform $\text{In}_{0.15}\text{Ga}_{0.85}\text{As}$ buffer, a more than three times enhancement of PL intensity from the QW is observed (shown in Fig. 3-11 (a)).

N is also incorporated in different parts of the $\text{GaAs}/\text{In}_{0.3}\text{Al}_{0.7}\text{As}$ strain compensated SL and resulting PL spectra are shown in Fig. 3-11 (b). The strain compensated SL alone without N (S1) increases the PL intensity by about 2.5 times as compared with the Ref sample. When N is incorporated into the SL, further improvements are obtained. Compared with the S1 sample, the strain difference becomes slightly larger or smaller when N is incorporated in GaAs (S2) or $\text{In}_{0.3}\text{Al}_{0.7}\text{As}$ (S3), respectively. The PL intensity of S3 shows an almost 50% increase compared with the S1. Even more, sample S4 with N incorporated in both GaAs and $\text{In}_{0.3}\text{Al}_{0.7}\text{As}$ layers shows the highest PL intensity. These improvements show unambiguous evidences of the N effect. The strong nitrogen bonding reveals the lattice hardening effect [100]. Dislocations generated in “soft” InGaAs are likely to be bent when they penetrate through the “hard” GaNAs or InAlNAs layer. This effect is independent of and stronger than the minor strain effect induced by N atoms.

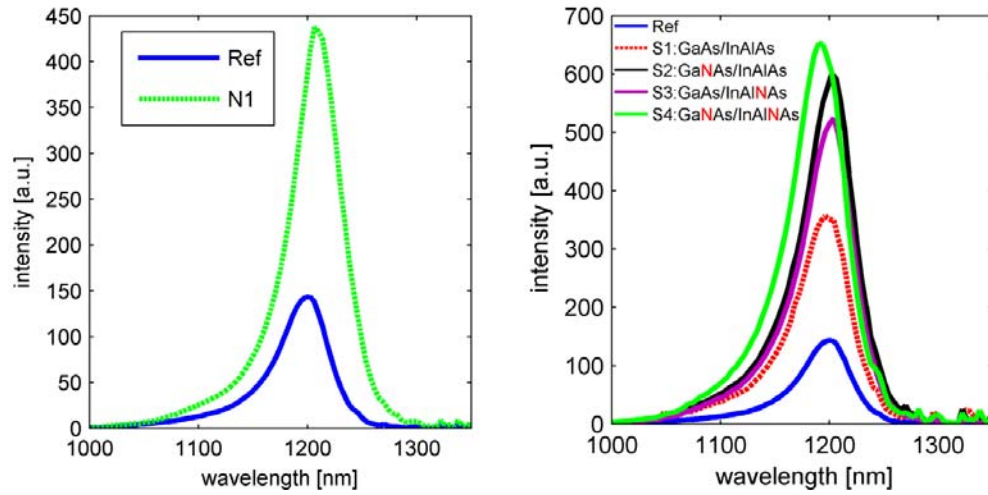


Figure 3-11. PL spectra of (a) the reference sample (Ref) and the sample with a dilute nitride SL (N1) and (b) samples with both N and a strain compensated SL in the TD blocking region.

4 Type II superlattice for MIR imaging

4.1 Introduction

InAs and GaSb has a type-II broken band alignment, as shown in Fig. 4-1 (a). When thin layers of InAs and GaSb are epitaxially grown alternately to construct a so called type-II superlattice (T2SL) as shown in Fig. 4-1 (b), an effective direct band-gap is formed. The effective band-gap can be tuned from 0 (semimetallic) to 0.5 eV just by adjusting the thickness of layers [13].

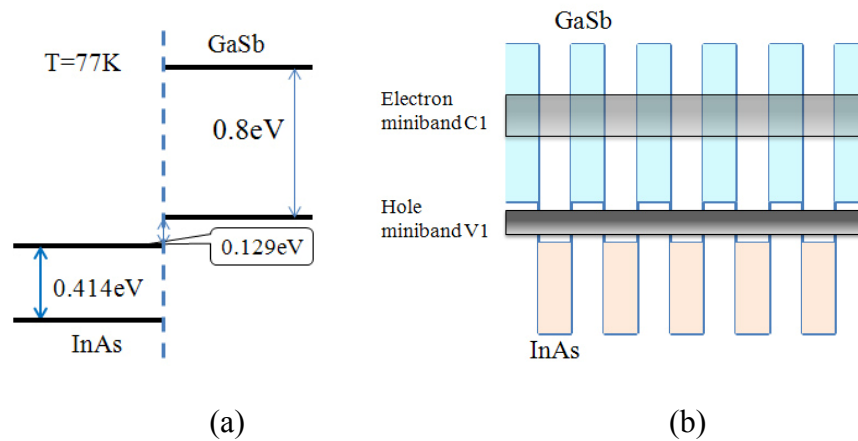


Figure 4-1. (a) Band alignment of InAs and GaSb (b) effective band-gap of an InAs/GaSb T2SL.

The InAs/GaSb T2SL structure was first proposed by Sai-Halasz *et. al.* in 1977 [101] and suggested to be a candidate for infrared detection by Smilth and Mailhiot in 1987 [26].

For MWIR and LWIR imaging, the most developed materials are $\text{Cd}_x\text{Hg}_{1-x}\text{Te}$ (MCT) and Quantum Well Infrared Photodetectors (QWIPs). MCT detectors have high efficiency and high operating temperature but struggle with the stability problem at long wavelength, leading to both high production costs and low image quality. By contrast, QWIP can achieve very nice image quality at relatively low cost of production, but the quantum efficiency is too low for some applications and also requires a low operating temperature [25]. The InAs/GaSb T2SL has recently shown very promising opportunities. A quantum efficiency of the same size as the MCT has been achieved in this material system [102]. At the same time it has all the similar advantages as QWIPs: a mechanically robust III-V material system that provides very good stability, uniformity and operability (few dead pixels).

In this chapter, we present optimization of growth parameters and interface control of InAs/GaSb T2SLs grown by MBE aiming for fabrication of MWIR FPA devices. In addition to the traditional group-V soaking, several strain compensation schemes are proposed and evaluated both experimentally and theoretically, and structural as well as optical qualities are compared. These schemes are of practical use and important if the MBE system has a high As background or the As-cell is inefficient to supply As₂. We have also carried out calculations for the band structure of T2SLs to assist understanding and design. Single pixel photodetectors with low dark current were demonstrated using the optimized growth conditions.

4.2 Optimization of MBE growth conditions

For MBE growth of new materials, the first step is to find proper growth conditions. Growth temperature (T_g) is one of the most important parameters for MBE growth of InAs/GaSb T2SL structures. To save cost, we use GaAs substrates to find the growth window. Fig. 4-2 (a) compares XRD rocking curves of the two samples grown at 340 and 470 °C, respectively. It can be found that the one grown at a low temperature shows better structural quality with narrow diffraction peaks and clear high-order peaks, while the one grown at a high T_g has inferior quality judged by broadening of the diffraction peaks. It is essential to employ low growth temperatures to obtain sharp interfaces. Due to different heater designs and temperature measurement techniques employed in different MBE systems, the nominal T_g -values reported in literatures are unreliable. We use the temperature and Sb flux dependent (1×3) to (2×5) surface reconstruction transition on GaSb, described by Bracker *et al* [103] to calibrate growth temperature. Figure 4-3 shows the (1×3) and (2×5) RHEED patterns and the surface phase diagram.

The proper T_g -value reported in literatures is commonly lower than the transition temperature at a certain Sb flux [104], i.e. under the (1×3) surface reconstruction. We optimize the growth temperature in the range of 320-380 °C using XRD and Hall measurement and results are summarized in Fig. 4-2 (b) and (c), respectively. The sample grown at 340 °C has the best interface quality as indicated by the narrowest -1st order diffraction peak, while the electron mobility shown in Fig. 4-2 (c) reaches a maximum at 360 °C. We choose 340 °C for the later samples. This temperature is much lower than the optimal growth temperature for GaSb.

InAs bulk is normally *n*-type, while GaSb is *p*-type, presumably due to the Fermi level pinning. The residual carrier density in an InAs/GaSb T2SL is determined by compensation of unintentionally doped carriers in GaSb and InAs layers [105]. The optimal T_g (340-360 °C) for InAs/GaSb T2SL is far below the optimal T_g -values for both GaSb and InAs bulk materials, leading to possibly an even higher density of residual carriers in both layers than the values grown at the optimal T_g . The measured net *n*-type carriers indicate that there are more electrons contributed

by InAs than the holes by GaSb. It's still unclear why the carrier density increases with growth temperature while the mobility has a maximum at 360 °C.

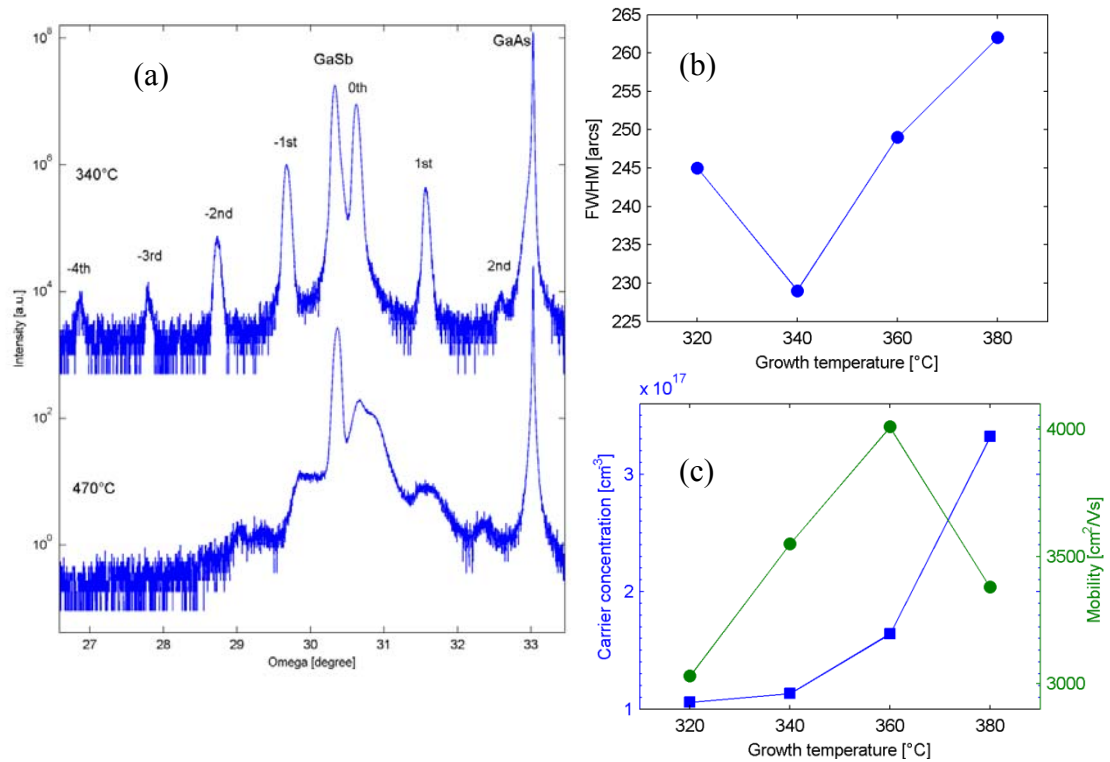
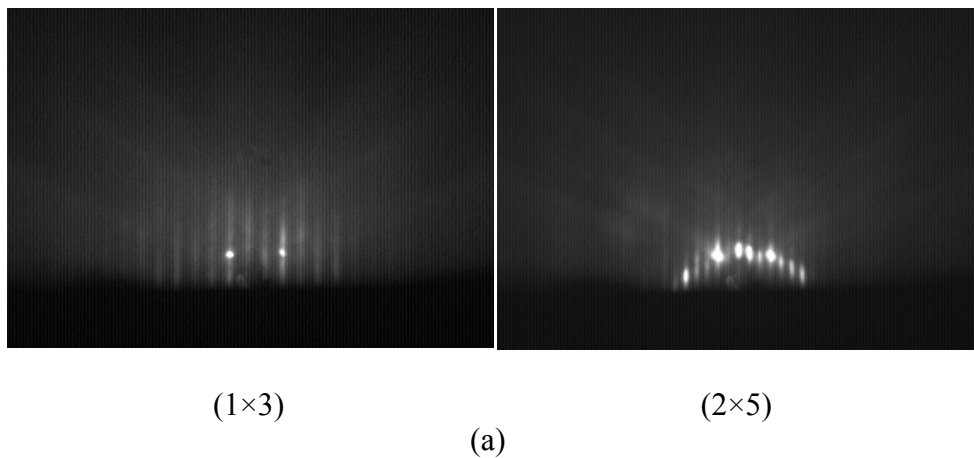


Figure 4-2. Effects of growth temperature on interface and transport quality of T2SL structures on GaAs comprising of 100 periods (10 ML InAs/10 ML GaSb). (a) shows XRD (004) rocking curves grown at 340 °C and 470 °C, respectively. (b) is the FWHM of the -1st order diffraction peaks vs. T_g . (c) shows the carrier density and mobility vs. T_g . All measurements are carried out at room temperature.



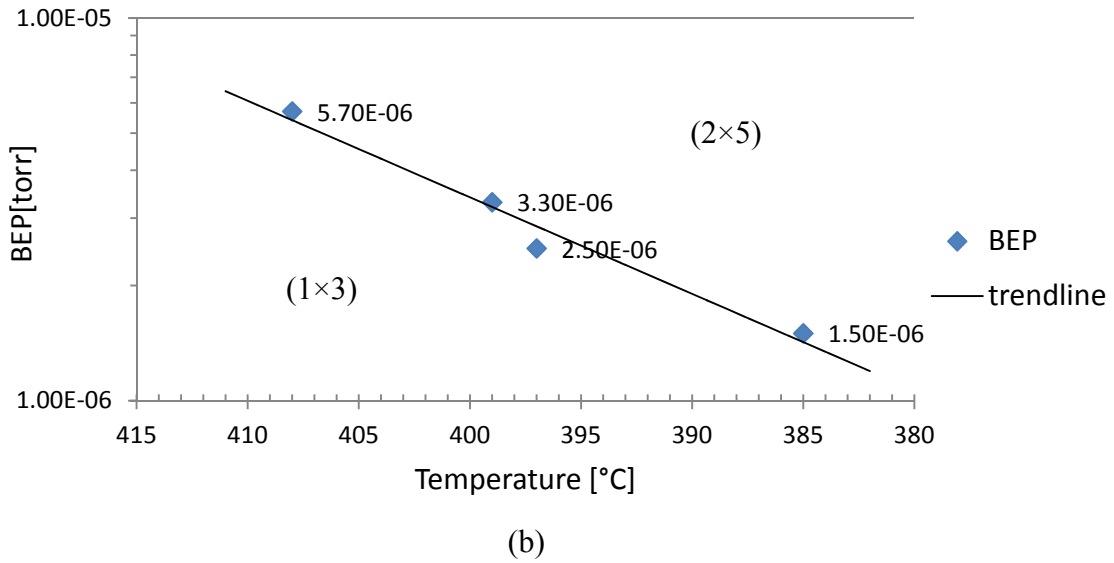


Figure 4-3. (a) RHEED patterns of the (1×3) and (2×5) surface reconstruction. (b) Surface phase diagram of GaSb.

Due to the fact that dual group-V elements are involved in growth of T2SL materials, soaking of one element at the interface is commonly used and necessary to control interface quality and tune the overall strain. Arsenic soaking after growth of GaSb will strengthen GaAs-like interface leading to extra tensile strain in the structure. However, it has been reported that proper As soaking can help in obtaining high crystalline and optical quality [106]. We have tested four different As soaking times with otherwise the same growth conditions. The XRD (004) rocking curves shown in Fig. 4-4 reveal clear differences between samples with and without As soaking. For the sample grown without As soaking, the interfaces have very low quality with almost no clear diffraction peaks. However, as short as 0.5 second As soaking makes a significant difference. This sample has well shaped high order diffraction peaks. Further increasing the As soaking time to 2 seconds and 3 seconds leads to peak splitting, indicating strain relaxation possibly caused by As-soaking induced excess tensile strain. This underlines the importance of strain compensation, which will be discussed in detail in the next section. For most of the following samples, 0.5 second As soaking time is employed after growth of GaSb. It should be noted that the proper As soaking time is related to the As flux used as well as the background As during the growth of GaSb. It also depends on whether the T2SL structure is grown on a GaSb substrate or GaSb template on a GaAs substrate since in the latter case, the GaSb template is not fully relaxed. For the optimization shown in Fig. 4-4, an Addon As-cracker is used and the sample is grown on GaAs. This cracker has an inefficient cracking efficiency and a severe leakage when the needle valve is closed leading to a high As background. When a Ribber As-cracker is used later, the background As is reduced significantly and the optimal As-soaking may shift away from 0.5 second.

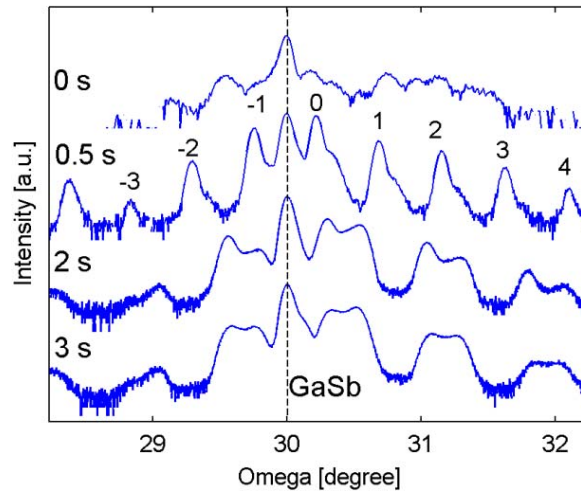


Figure 4-4. XRD (004) rocking curves of 100 periods (10 ML InAs/10 ML GaSb) T2SLs grown at 340 °C on GaAs with different As soaking time labeled above each curve. The order of the diffraction peaks for the sample with 0.5 s As soaking is marked above the curve.

Antimony soaking after growth of the InAs layer up to 14 seconds has been tested. No obvious difference is observed. This is probably due to the large amount of accumulated As on the InAs surface caused by the problem related to the Addon As-cracker discussed above, such that the Sb soaking becomes ineffective. 12 second Sb soaking time is employed for most of the later samples.

4.3 Strain compensation

Although InAs and GaSb are commonly regarded as a “lattice matched” material system, the 0.6% lattice mismatch still leads to tensile strain in the structure when grown on GaSb substrates and strain relaxation may occur for micrometer thick devices. Threading dislocations will then strongly degrade the device performance. Therefore, a strain compensation scheme to avoid formation of TDs is essential for high performance of T2SL photodetectors.

Besides the intrinsic lattice mismatch between InAs and GaSb, different types of interfaces can also bring in excess strain, which, however, can be engineered. There are basically two types of interfaces in InAs/GaSb T2SL structures: GaAs-like and InSb-like. Due to the different bonding lengths, GaAs-like interfaces will add tensile strain, while InSb-like interfaces bring in compressive strain. Apparently, an InSb-like interface is preferable to compensate the accumulated tensile strain of the InAs layers. Group-V-rich condition is common for MBE growth of III-V compounds, i.e. each layer of InAs and GaSb is group-V terminated. When growth of an InAs layer is finished, the top atomic layer is As. The next incorporated atomic layer will be the group-III element, Ga, when

continuing growing a GaSb layer. Consequently, the interface is connected by As-Ga bonds, forming a GaAs-like interface as shown in Fig. 4-5 (a). One would expect an InSb-like interface to form in a similar way when an InAs layer is grown on a GaSb layer, as shown in Fig. 4-5 (b). However, since the substitution of Sb atoms by As atoms is thermodynamically favored due to the higher bonding strength of As-Ga than Sb-Ga, the result can be a partial or complete GaAs-like interface also in this case; see Fig. 4-5 (c). Therefore, the chance to form GaAs-like interfaces is usually higher than that for InSb-like interfaces, leading to increased overall tensile strain, i.e. the 0th peak of an XRD rocking curve appears at a larger angle than that of the GaSb peak. Fig. 4-6 shows an XRD rocking curve of a T2SL sample without strain compensation.

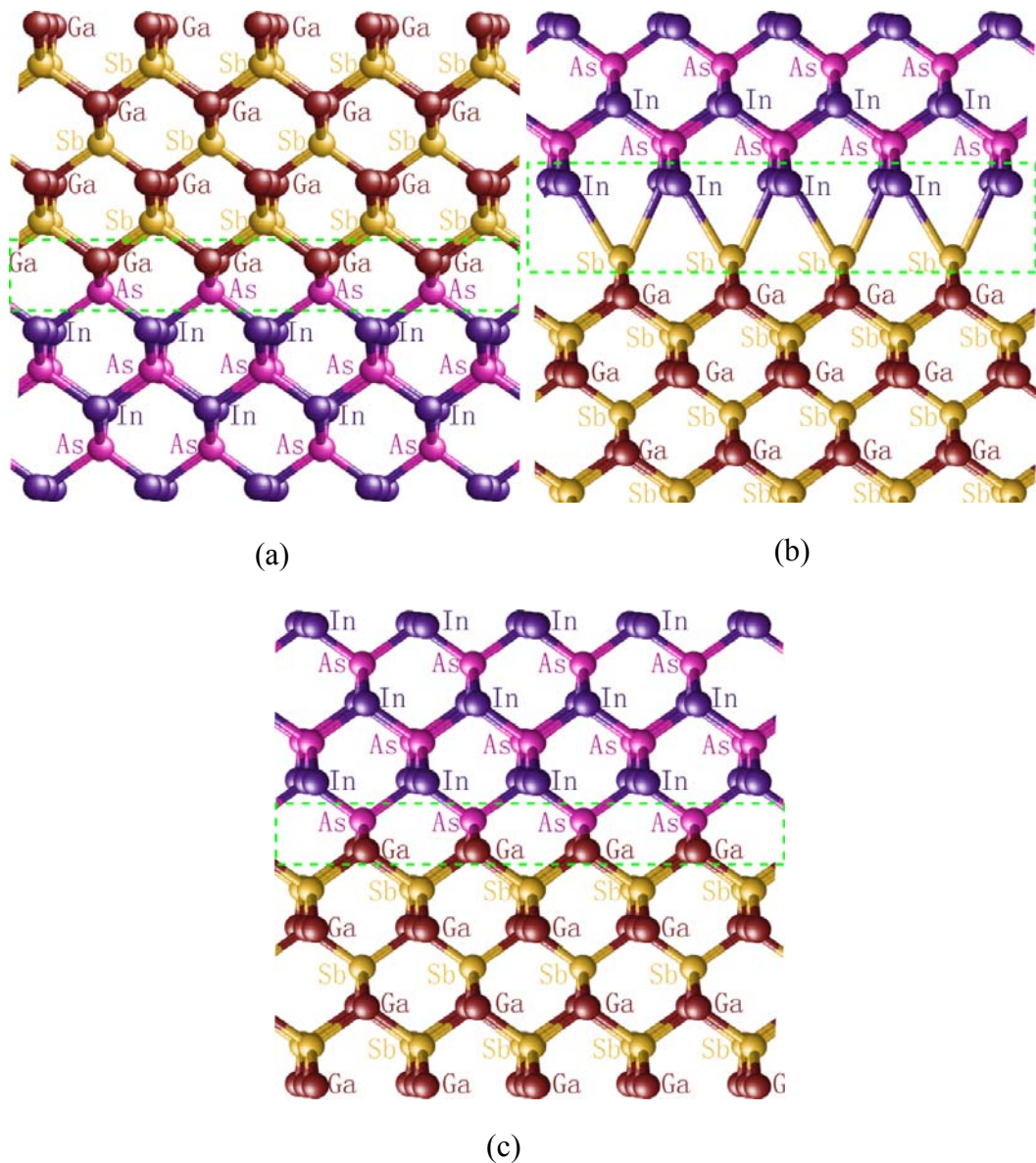


Figure 4-5. Schematic illustrations of different types of interfaces. (b) InSb-like interface, (a) and (c) GaAs-like interface.

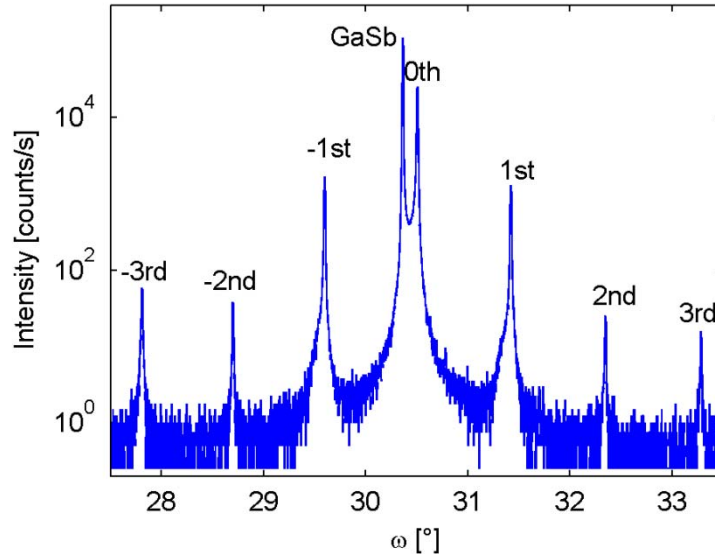


Figure 4-6. An XRD (004) rocking curve of a T2SL sample without strain compensation but with group-V soaking at interfaces.

4.3.1 Strain compensation methods

Strengthening the InSb-like interfaces by extensive Sb soaking is a common strategy for strain compensation in T2SL structures. By using long time Sb soaking after growth of InAs layers, part of the top As atoms would be replaced by Sb atoms, forming partially InSb-like interfaces. Figure 4-7 (a) shows the shutter sequence of this method with Sb soaking after InAs layer and short As soaking after GaSb layer. However, this method was found insufficient to compensate the strain to an acceptable extent due to the As-problem mentioned above [106], [107]. We propose new strain compensation methods based on shutter sequences as schematically shown in Fig. 4-7 (b)-(d). An additional In layer is introduced to reinforce the InSb-like interfaces. In method (b), 1 ML In is deposited right after GaSb, and then soaked with Sb to form 1ML InSb. The short As soak before switching to InAs may lead to formation of a monolayer of InAsSb due to As-Sb intermixing. In method (c), a short Sb soaking is employed after the growth of InAs layer to remove residual As and establish an Sb environment on the growth front. Then 1 ML In is deposited and followed by Sb soaking again. Thus, a full monolayer of InSb is formed. In both cases, formation of GaAs-like interfaces can be avoided. In method (d), 1 ML InSb is directly inserted in the middle of the GaSb layer, as far away as possible from the As-containing interfaces.

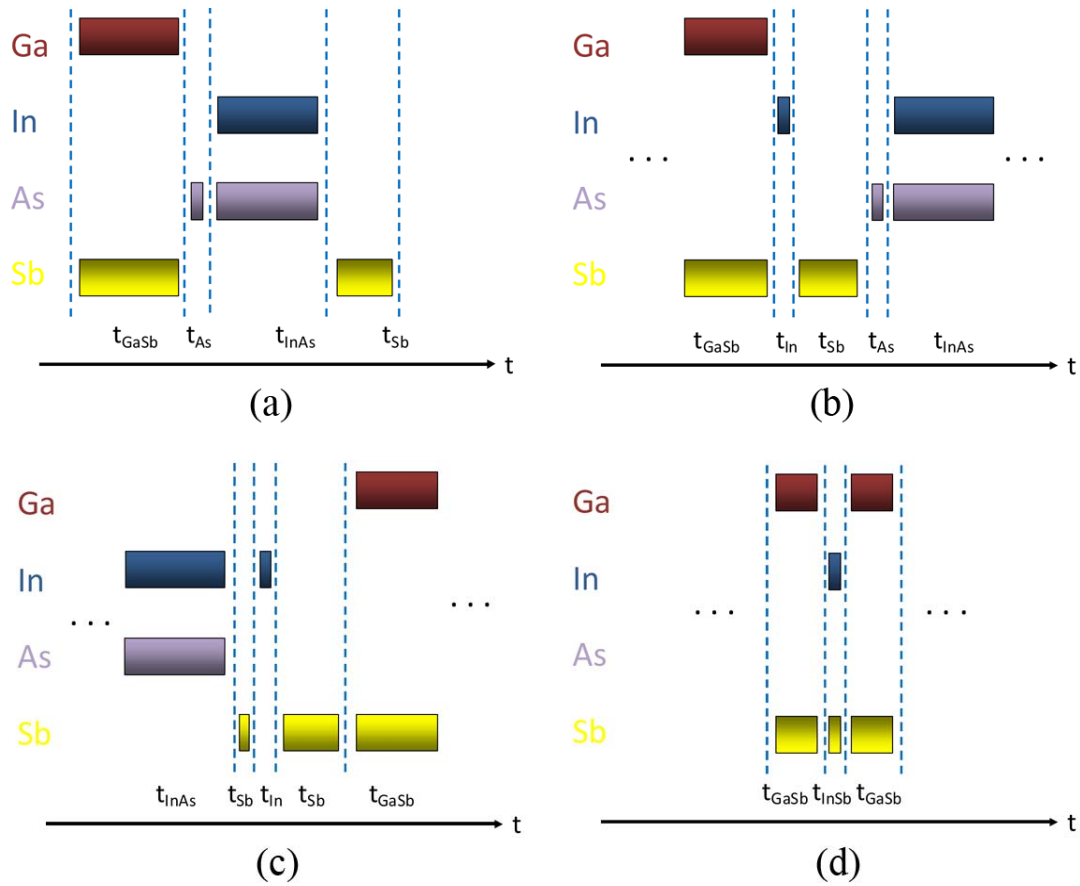


Figure 4-7. Shutter sequences of different strain compensation methods. (a) Common strategy with As and Sb soakings only. (b) Strengthened In(As)Sb-type interface after GaSb layer. (c) Strengthened In(As)Sb-type interface after InAs layer. (d) One additional InSb monolayer inserted in the middle of a GaSb layer.

The strain compensation methods shown in Fig. 4-7 are tested individually on the first batch of samples with 100 periods of 10 ML InAs/10 ML GaSb layers grown on GaSb substrates. When one method is applied at one interface, the other interface is treated with normal soaking. The FWHM of the -1^{st} order diffraction peak for the sample with method (a) is 165 arcs, and the residual lattice mismatch is -0.51% . It turns out that the strain compensation method (b), (c) and (d) indeed reduces the overall strain compared with (a) by 49%, 78% and 41%, respectively. Method (c) shows the largest strain compensation effect, but the FWHM of the -1^{st} order diffraction peak is 2.3 times compared with that of method (a). Method (b) and (d) show narrower -1^{st} diffraction peaks than that of method (a) by 34% and 76%, respectively, despite being less effective in strain compensation. The sample grown with method (d) has better interface quality and smaller lattice mismatch, and shows a much higher PL intensity compared with the sample using method (a), see Fig. 4-4. Since the sample grown with method (d) has one ML of InSb

embedded in the GaSb layer, the PL peak wavelength is red-shifted with respect to the sample grown with method (a).

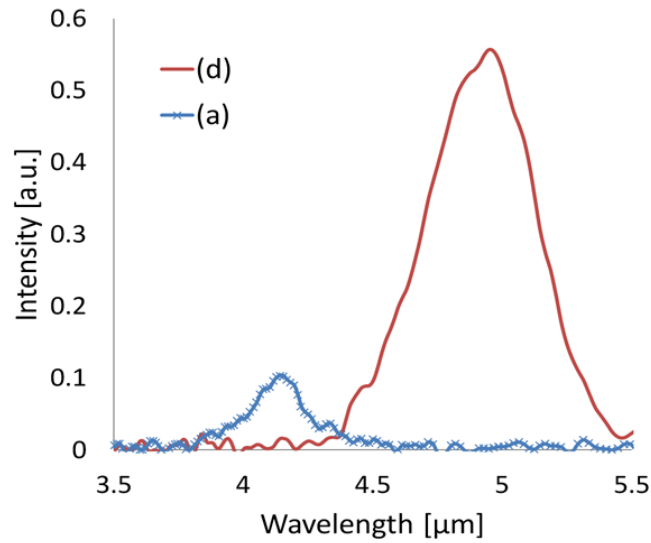


Figure 4-8. PL results at 77K of samples with the strain compensation method (a) and (d).

In order to further compensate the overall strain in T2SL materials, strain compensation schemes with combinations of the above methods are investigated. The results on structural properties of this group of samples are summarized in Table 4-1. It should be noted that the thickness of InAs layers in this group of samples is 7 ML in order to adjust PL wavelength to be shorter than 5 μm . The interface quality is surprisingly very much improved, compared to when only one strain compensation method (b) or (c) is employed. Both the combinations of (b)+(d) and (c)+(d) show very small residual lattice mismatch and narrow -1st order diffraction peak indicating high interface quality. Combination of (b)+(c) leads to slightly larger residual lattice mismatch and worse interface quality. By combining all methods (b)+(c)+(d), the strain is tuned from tensile type to compressive type with relatively good interface quality.

Table 4-1 Comparison of different strain compensation strategies. Positive lattice mismatch values are for compressive strain while negative ones for tensile strain. All samples are grown on GaSb substrates with 100 periods of 7 ML InAs and 10 ML GaSb.

Methods	FWHM of -1st peak [arcsec]	Lattice mismatch [%]
b+c	63	-0.18
c+d	37	-0.09
b+d	38	-0.06
b+c+d	53	0.09

PL measurements are carried out and show peak wavelengths around 4.5 μm for samples grown with a combination of two methods, and higher intensity than that of the samples which are grown with only one method. Strain compensation strategies presented here are effective for both strain compensation and improvement of interface quality. In this way, the residual strain can be controlled between tensile and compressive type.

4.3.2 Theoretical modeling of strain compensation in T2SL

At low growth temperatures used in this work, it is reasonable to assume that there is little intermixing between group-III atoms through diffusion or segregation. For an ordinary InAs/GaSb T2SL structure as shown in Fig. 4-9 (a), the number of In and Ga atomic layers in each period is denoted by M and N , respectively. We assume that As and Sb intermixing only occurs at the interface to form one atomic layer of AsSb, and denote x and y as the As composition at the GaSb/InAs and the InAs/GaSb interfaces, respectively. Subsequently, for the last layer of Ga atoms at the GaSb/ InAs interface, the bottom (left in the figure) bonds are Ga-Sb, while the upper (right) bonds become mixture of Ga-As and Ga-Sb with proportion of x and $1-x$, respectively. Same for the first layer of the In atoms that, the bottom bonds are mixture of x In-As and $1-x$ In-Sb while the upper bonds are still In-As. It is in a similar situation for the other interface. The In-As, Ga-As and In-Sb bonds contribute to lattice mismatch with respect to the GaSb substrate. Therefore, the overall lattice mismatch can be expressed as

$$f = \left[\left(M - 1 + \frac{x}{2} + \frac{y}{2} \right) f_{InAs} + \left(\frac{x}{2} + \frac{y}{2} \right) f_{GaAs} + \left(\frac{1-x}{2} + \frac{1-y}{2} \right) f_{InSb} \right] / (M + N) \quad (4-1)$$

where f_{InAs} , f_{GaAs} and f_{InSb} are the lattice mismatch of InAs, GaAs and InSb with respect to GaSb, respectively. $(M+N)$ is the total number of atomic monolayers of one period of the T2SL structure. In the above derivation, we neglect the small difference in lattice constants of InAs and GaSb in the denominator. Detailed derivation is given in Appendix A.

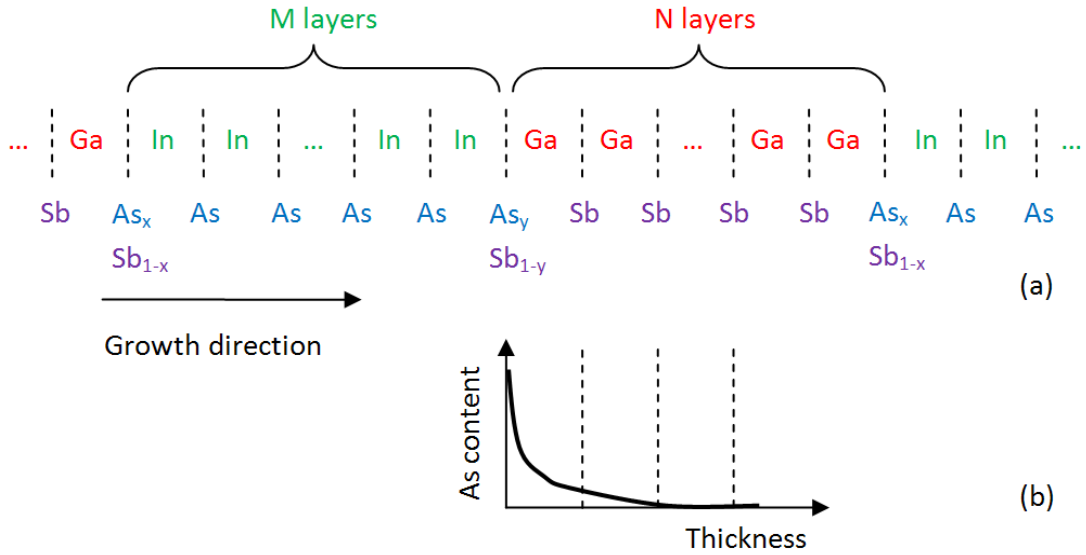


Figure 4-9 Schematics of (a) an InAs/GaSb T2SL structure, and (b) incorporation of background As into the following GaSb layer.

For an MBE chamber used to grow arsenides, a small amount of background As is expected to be incorporated during growth of the GaSb layer, forming $\text{GaSb}_{1-z}\text{As}_z$, where z is the composition of As. Use of an inefficient and leaky As-cracker discussed above will significantly enhance the As background. Moreover, at such low growth temperatures which are comparable to the As source temperature, the adsorbed As atoms may not be capable of re-evaporating from the sample surface if not incorporated, leading to a certain amount of residual adsorbed As atoms on the growth front of the InAs layer. Part of these adsorbed As atoms will be incorporated into the following GaSb layer as schematically shown in Fig. 4-9 (b). A similar process could occur at the other interface for Sb atoms, but the effect will be much weaker due to the weak bonding of Ga-Sb compared with Ga-As and is negligible here. In addition, the background Sb in InAs is much lower than the background As in GaSb, judged by at least one order of magnitude difference in background pressure when growing GaSb and InAs. As a result, additional tensile strain will be introduced by the adsorbed and background As atoms. Then, Eq.(4-1) becomes

$$f = \left[\left(M - 1 + \frac{x}{2} + \frac{y}{2} \right) f_{\text{InAs}} + \left(\frac{x}{2} + \frac{y}{2} + Nz' \right) f_{\text{GaAs}} + \left(\frac{1-x}{2} + \frac{1-y}{2} \right) f_{\text{InSb}} \right] / (M + N) \quad (4-2)$$

where, $z' = \alpha / N + z$ is the average background As composition in GaSb and α is the total amount of incorporated As in GaSb layer due to the excess As atoms adsorbed during InAs growth.

By inserting the values of f_{InAs} , f_{GaAs} and f_{InSb} with -0.0062, -0.0726 and 0.0629, respectively, we get

$$f = (0.0691 - 0.0062M - 0.0709x - 0.0709y - 0.0726Nz') / (M + N) \quad (4-3)$$

Therefore, the key idea for strain compensation is to reduce the values of x and y , as well as using small As flux to minimize α .

The overall lattice mismatch of the strain compensation methods shown in Fig. 4-7 (a) can be modeled in the same way. It is easily seen that the strain can never be fully compensated if the InAs thickness is more than 11 ML by only soaking even with both x - and y -values equal to zero. Sb-As exchange during Sb soaking has been found to be much less effective than the As-Sb exchange during As soaking [106], [107]. Therefore, we expect that the value of y is high in our case, or even close to 1. If we assume that $y=1$, (4-3) reduces to

$$f = (-0.0018 - 0.0062M - 0.0709x - 0.0726Nz') / (M + N) \quad (4-4)$$

This indicates that f can never reach zero for any thickness of InAs using only soaking.

The overall lattice mismatch of other methods shown in Fig. 4-7 is summarized in Table A-1, Appendix A2.

It should be noted that, for methods (b), (c) and (d), one additional monolayer of In is inserted, so the total thickness is changed to $(M+N+I)$. If we compare the first equation of each method in Table A-1, the first term with f_{InAs} does not differ very much among case (a) - (d). The second term with f_{GaAs} is reduced to roughly half in (b) and (c). This gives direct evidence that insertion of 1 ML InSb at one interface avoids direct contact of As and Ga atoms forming GaAs-like interface. The last term with f_{InSb} reflects the effect of the one monolayer InSb.

f , M and N are variables which can be controlled or measured by XRD, so they can be considered to be known values. By changing the GaSb thickness, *i. e.* N , but keeping all other growth conditions the same, the average residual As composition in the GaSb layer, z' , can be obtained with any methods discussed above. If we assume that the overall lattice mismatch of an original T2SL structure is f_1 , and that of another structure with the GaSb layer thickness changed by ΔN , is f_2 , we can calculate the z' by

$$z' = \frac{(M + N)f_1 - (M + N + \Delta N)f_2}{0.0726\Delta N} \quad (4-5)$$

It is understood from Fig. 4-7 that, under the same growth conditions, the x -value should be the same for methods (a), (c) and (d), while the y -value should be the same for (a), (b) and (d). z' -value should be the same for all the cases as long as the same As flux is used. Upon knowing the z' -value, both x - and y -values can be readily obtained by solving the equations. By applying these equations to our experimental results for the samples with one strain compensation method used, we find $y = 95\%$ in method (a) and $x + 1.025 Nz' = 26\%$ in method (c). This implies that at almost 26% Sb was replaced by As during only 0.5s As soaking and only 5% As is replaced by Sb when InAs surface is soaked by Sb for 12 second.

Strain compensation schemes with combinations of the methods are also studied and summarized in Table A-2, Appendix A2.

The above modeling of strain compensation methods provides quantitative information of chemical compositions at the two interfaces and indicates the effectiveness for the particular strain compensation technique used. The strain compensation can therefore be implemented in a controlled manner, making it easy to balance strain compensation with other requirements for a detector, such as bandgap, optical and structural qualities.

4.4 Band structure calculations of proposed T2SLs

The insertion of 1 ML InSb in the GaSb layer of a T2SL structure has been found to be beneficial for strain compensation, improving interface and optical properties. The band structure of such T2SL structures have been calculated with the $\mathbf{k}\cdot\mathbf{p}$ model. Figure 4-10 (a) and (b) show the band alignments as well as the envelope wavefunctions of a T2SL structure composed of 10 ML InAs/5 ML GaSb/1 ML InSb/5 ML GaSb. It is found that the lowest lying conduction band state in the superlattice, namely C1, is a mixture of mainly bulk conduction band (C) and light hole (LH) states (78% and 19%, respectively), and very little of spin-orbit (SO) states. The lowest valence band state, HH1, on the other hand, is pure 100% heavy-hole (HH) states in character. The electron wavefunction extends into the GaSb layer, while that of holes in the valence band is confined mostly in the GaSb layer. The corresponding band dispersion in the in-plane and along the growth direction is shown in Fig. 4-10 (c). The HH1 band is found to have very little dispersion in the growth direction, which means that the effective mass is very large and that it is difficult for the holes to tunnel through the layers. InAs and GaSb thicknesses are varied individually in our calculations. Fig. 4-10 (d) shows the effective cutoff wavelength of the material as a function of layer thickness. Like T2SL structures without an InSb layer in the middle of GaSb layer, the

effective band-gap is found to be sensitive only to changes in the InAs thickness. The reason is that, due to the large heavy-hole effective mass of the GaSb valence band, an increased GaSb thickness leads only to a small upward movement of the HH1 energy.

The optical matrix element $\| \langle C1 | P(\mathbf{k}) | HH1 \rangle \|$ is an indication of optical transition strength. It can be found in Fig. 4-10 (e) that the matrix element at the zone centre is indeed larger with thinner GaSb or InAs layers. The band-gap and optical transition can thus be optimized by individually varying GaSb and InAs layer thicknesses.

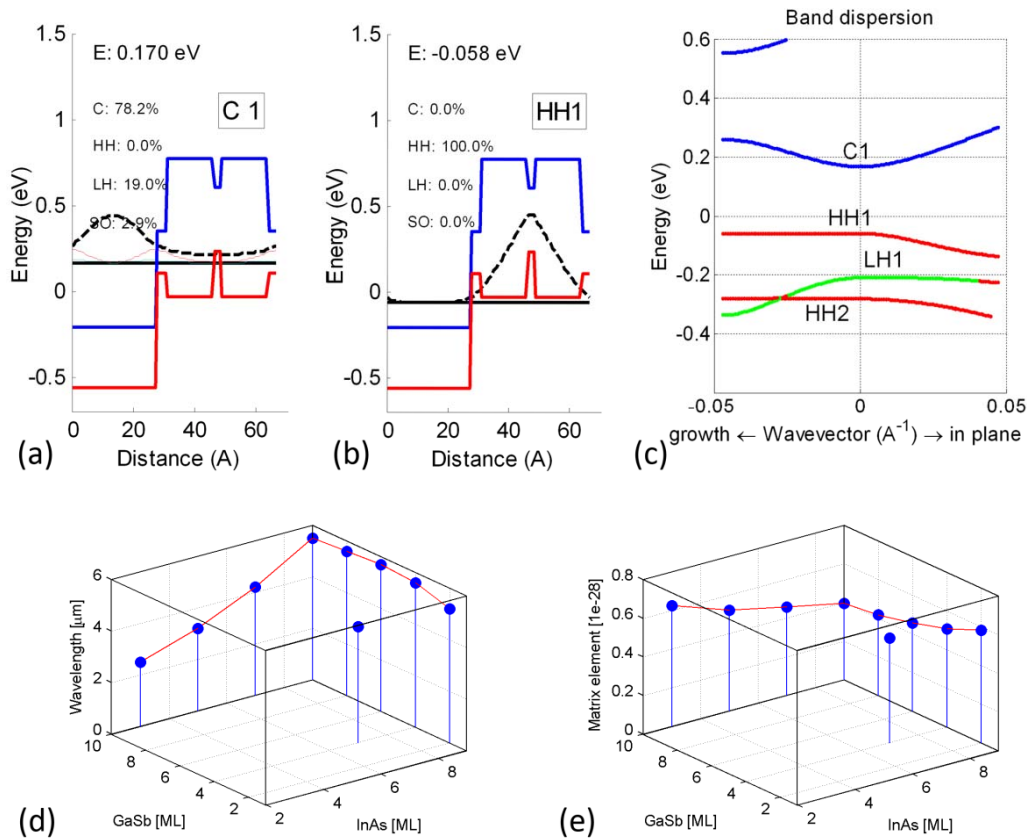


Figure 4-10. Band structure calculations based on the $k \cdot p$ model. (a) and (b) show band alignments of a T2SL structure with 10ML InAs/5ML GaSb/1ML InSb/5ML GaSb and the calculated energy levels and zone center envelope wavefunctions for the lowest confined levels in the conduction and the valence band, respectively. (c) shows the band dispersion of the same T2SL structure along, and perpendicular to, the growth direction. (d) and (e) show the cutoff wavelength and zone center optical matrix element $\| \langle C1 | P(k=0) | HH1 \rangle \|$, respectively, as a function of InAs and GaSb thicknesses.

4.5 Single pixel photodetector

Single pixel *p-i-n* photodetectors are demonstrated. The structure consists of 560 periods of 4 ML InAs/8 ML GaSb T2SLs with strain compensation strategy of (b)+(c)+(d). The process uses a combination of dry and wet etching to create pixels. The mesa sidewalls are then passivated with polymer-based passivation and the contacts are deposited. The optical response is measured with a 100 % cutoff at 3.8 μm . Fig. 4-11 shows the dark current density for different pixel sizes at 80 K. The dark current density at small reverse biases is in the 10^{-9} A/cm² range at 80 K and increases to the 10^{-4} A/cm² range at 160 K, and is almost independent of pixel size as a result of effective device passivation.

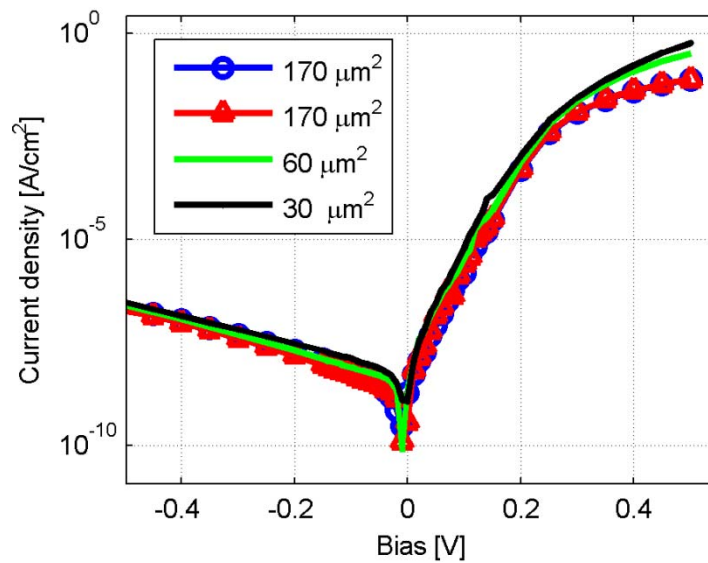


Figure 4-11. Measured dark current density for different pixel sizes at 80K.

5 Dilute bismides

5.1 Introduction

Bismuth is the heaviest and the least studied group-V element. When a small amount of Bi atoms are incorporated in common III-V compounds, for example arsenides and antimonides, Bi defect states will be formed close to the valence band edge of the host semiconductor. The quantum interaction between the valence band states and the Bi states is expected to lead to a large band gap reduction [18] [19] and strong spin-orbit splitting [16] which is schematically shown in Fig. 5-1. Contrary to the case of dilute nitride, which is well-known for its large bandgap bowing effect by lowering of the conduction band edge, the influence of Bi on band structure occurs only in the valence band. This provides a new degree of freedom to engineer band structure of semiconductors for potential electronic and optoelectronic applications. Furthermore, electron transport in dilute bismide materials are much less influenced than those in dilute nitride materials since little perturbation happens in the conduction band [20]. Figure 5-2 shows how the bandgap changes with Bi composition in some dilute bismide materials based on theoretical calculations or experiment results. The bandgap reduction of $\text{In}_x\text{Ga}_{1-x}\text{As}$, $\text{In}_x\text{Ga}_{1-x}\text{Sb}$, $\text{GaAs}_x\text{Sb}_{1-x}$ and $\text{InAs}_{1-x}\text{Sb}_x$ for $x=1\%$ is 15, 10, 19 and 9 meV, respectively [108] for comparison.

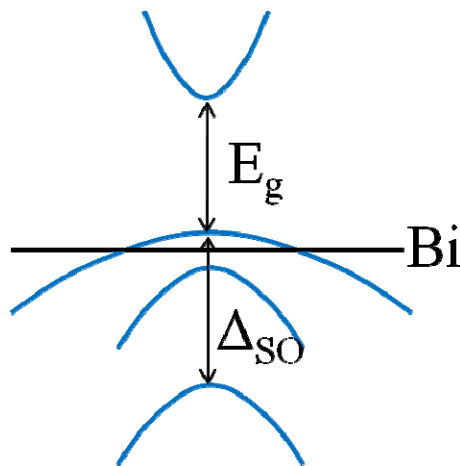


Figure 5-1. Schematic showing the anticrossing of the valence band of III-V host material with the Bi defect state.

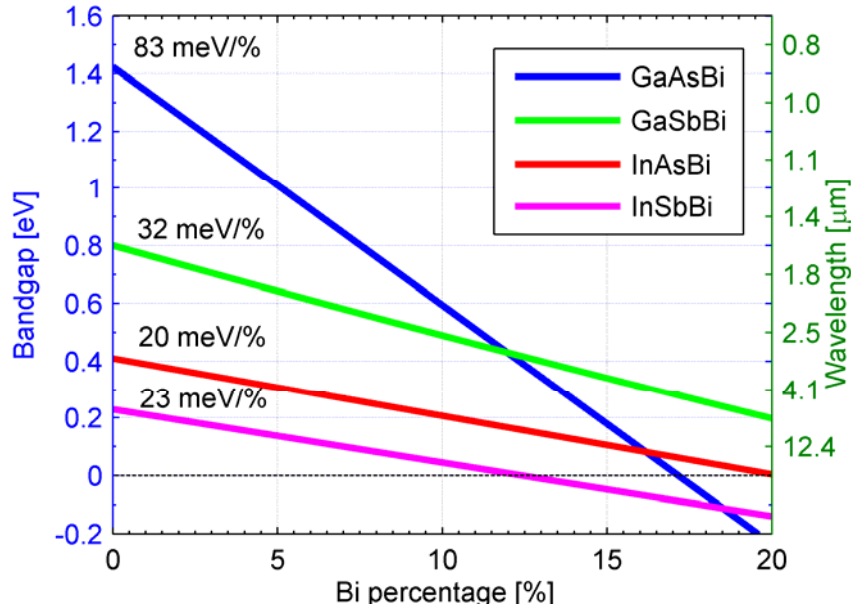


Figure 5-2. Bandgap energy and the corresponding wavelength vs. Bi percentage in $\text{GaAs}_{1-x}\text{Bi}_x$ (300K) [19], $\text{GaSb}_{1-x}\text{Bi}_x$ (77K) [128], $\text{InAs}_{1-x}\text{Bi}_x$ (77K) [18] and $\text{InSb}_{1-x}\text{Bi}_x$ (77K) [18], respectively. The slope labeled above each curve may be valid only for small x -values.

Intensive research has been implemented on $\text{GaAs}_{1-x}\text{Bi}_x$ and related materials after its first realization of epitaxial growth by metal organic vapor phase epitaxy (MOVPE) in 1998 [109] and by molecular beam epitaxy (MBE) in 2003 [110]. The bandgap bowing effect [19] and the spin-orbit splitting effect [21] were experimentally observed afterwards. The valence band edge reduction can lead to a reduced temperature dependence of the band gap, which is attractive for fabricating temperature insensitive lasers, optical amplifiers, and modulators for telecommunication. The large spin-orbit splitting is also proposed to suppress inter-valence band Auger recombination processes and thus increasing the characteristic temperature of 1.55 μm telecom lasers on GaAs [22]. Antimonide based dilute bismides are much less studied. By utilizing the bandgap bowing effect, several attempts to reach the narrowest possible band gap of III-V materials for long wavelength infrared detectors were carried out since the late 1970s by synthesizing $\text{InSb}_{1-x}\text{Bi}_x$ [111] [112] [113] and $\text{InAs}_{1-x}\text{Bi}_x$ bulk materials [114]. While, $\text{GaSb}_{1-x}\text{Bi}_x$ is almost unexplored.

GaSb based III-V semiconductor compounds are very attractive for optoelectronic devices working at near- and mid-infrared range, such as lasers, detectors and modulators; as well as high speed electronic devices, for example, bipolar transistors [125]. Incorporation of Bi in III-Sb will have several potential benefits. First, Bi incorporation in GaSb can reduce the band gap and thus extend the emission wavelength more effectively than utilizing InGaSb. Second, one major problem for $>3 \mu\text{m}$ GaSb based type-I quantum well (QW) lasers is insufficient valence band offset [23] due to the use of heavily compressively strained

InGaAsSb QWs, resulting in significant hole leakage. By employing Bi, the large valence band offset can suppress the hole leakage. Third, the spin-orbit splitting energy of GaSb at 300 K is about 0.735 eV, very close to the direct band gap of 0.75 eV. Only a small amount of Bi in $\text{GaSb}_{1-x}\text{Bi}_x$ is required to reverse the two energy values, suppressing Auger recombination processes in optoelectronic devices. So far, little work has been done on synthesis of $\text{GaSb}_{1-x}\text{Bi}_x$. To the best of our knowledge, only two publications attempting to incorporate Bi in bulk GaSb ingots using liquid phase growth methods were found [116], [117]. Both work were intended to use Bi as a dopant to reduce background p-doping in GaSb ingots.

In this chapter, we first present the physical challenges of growing dilute bismide materials by MBE and our strategies to enhance Bi incorporation while avoiding surface defects. Then we report growth and characterizations of $\text{GaSb}_{1-x}\text{Bi}_x$ and $\text{InSb}_{1-x}\text{Bi}_x$ thin films.

5.2 Strategies for enhancing Bi incorporation

There are several physical challenges for the growth of dilute bismide materials. Firstly, there is a solubility limit of Bi concentration in III-V-Bi alloys. Non-thermal equilibrium methods, such as MBE, are necessary to incorporate Bi atoms beyond this limit. Secondly, the large atomic size and heavy weight of Bi atoms makes Bi alloys thermally unstable. A low growth temperature must be employed to synthesize dilute bismide materials without decomposition. For example, less than a doping level of Bi atoms can be incorporated into GaAs if the growth temperature is higher than 450 °C [118]. Thirdly, the bonding energy of III-Bi (GaBi 1.47 eV, InBi 1.16 eV) is smaller compared with that of common III-V compounds such as GaAs (2.12 eV), GaSb (1.83 eV) and InSb (1.39 eV) [119] [120]. This makes Bi atoms difficult to compete with As or Sb to form crystal lattice. Therefore, a high Bi/V flux ratio and a low V/III flux ratio are critical to enhance Bi incorporation. The latter enhances the risk for formation of group-III droplets, e.g. Ga and In droplets, in particular at high growth temperatures. Figure 5-3 shows the surface morphology of GaSbBi grown on GaSb with excess Bi. Fourthly, Bi is metallic that is different from other group-V elements. Excess Bi atoms on the growth surface will form Bi droplets if they are neither incorporated nor evaporated. This risk increases at low growth temperatures. Finally, Bi is known as surfactant on InGaAs to lower surface energy. This property together with the large atomic size of Bi atoms facilitates Bi accumulation on growth surface via segregation.

Based on previous experiences on growth of GaAsBi and above identified challenges, our strategies for enhancing Bi incorporation in III-SbBi and simultaneously suppressing metallic droplets at the same time are summarized as below:

- Low growth temperatures ranging between 330 and 395°C are employed.
- Low growth rates (0.1 and 0.2 $\mu\text{m}/\text{h}$ for GaSb and InSb, respectively) are used.
- Low V/III ratios are utilized. The BEP of Sb is set to be 10% higher than the critical Sb BEP for the growth of GaSb or InSb with the criterion of the surface degradation judged by RHEED.
- The Bi BEP is selected close to the Bi vapor pressure corresponding to the growth temperature. Thus, the excess Bi will be evaporated. The relation between Bi vapor pressure and temperature was calculated and plotted in Fig. 5-4.

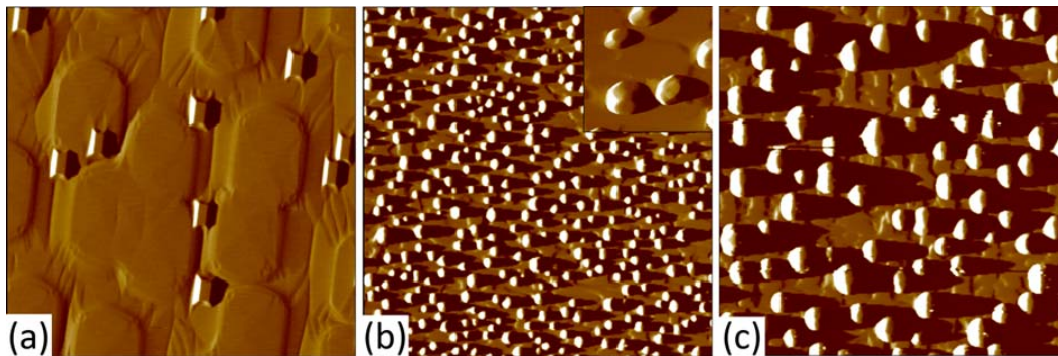


Figure 5-3. $10 \times 10 \mu\text{m}^2$ AFM amplitude images of $\text{GaSb}_{1-x}\text{Bi}_x$ samples grown with a $0.5 \mu\text{m}/\text{h}$ growth rate on GaSb substrate. The samples are grown at (a) 380°C , (b) 360°C and (c) 340°C , respectively. The inset in (b) is a zoom-in image with a $1 \times 1 \mu\text{m}^2$ area.

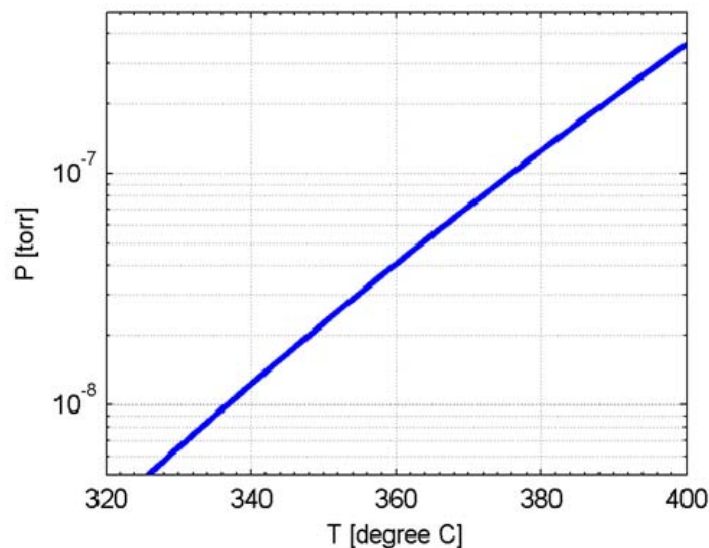


Figure 5-4. Bi vapor pressure vs. temperature

5.3 MBE growth and characterization of GaSb_{1-x}Bi_x

5.3.1 GaSbBi on GaSb substrates

Based on the strategies discussed in the previous section and some optimizations of growth conditions, a group of 200 nm thick GaSb_{1-x}Bi_x samples are grown on undoped (100) GaSb substrates by MBE. All these samples are grown at 0.1 $\mu\text{m}/\text{h}$ with a Ga BEP of $2.0\text{e-}8$ Torr and an Sb BEP of $8.8\text{e-}8$ Torr. The growth temperature is varied from 330 °C to 390 °C and the Bi BEP is set to be close to the vapor pressure at particular growth temperatures, *i. e.* $1\text{e-}8$, $4\text{e-}8$, $7\text{e-}8$, $1\text{e-}7$ and $2\text{e-}7$ Torr at 330, 360, 370, 380 and 390 °C, respectively.

5.3.2 Surface morphology

The Ref sample without Bi shows smooth and uniform surface with atomic steps. The GaSbBi samples grown at 360 °C or lower show similar high quality surface with atomic steps forming triangle shaped features as shown in Fig. 5-5 (a) and have slightly larger RMS roughness than that of the Ref sample. For the samples grown at high temperatures, the surface becomes rough with elongated dots as shown in Fig. 5-5 (b). The shape of elongated dots indicates anisotropy of surface diffusion of adatoms along the two orthogonal crystal directions.

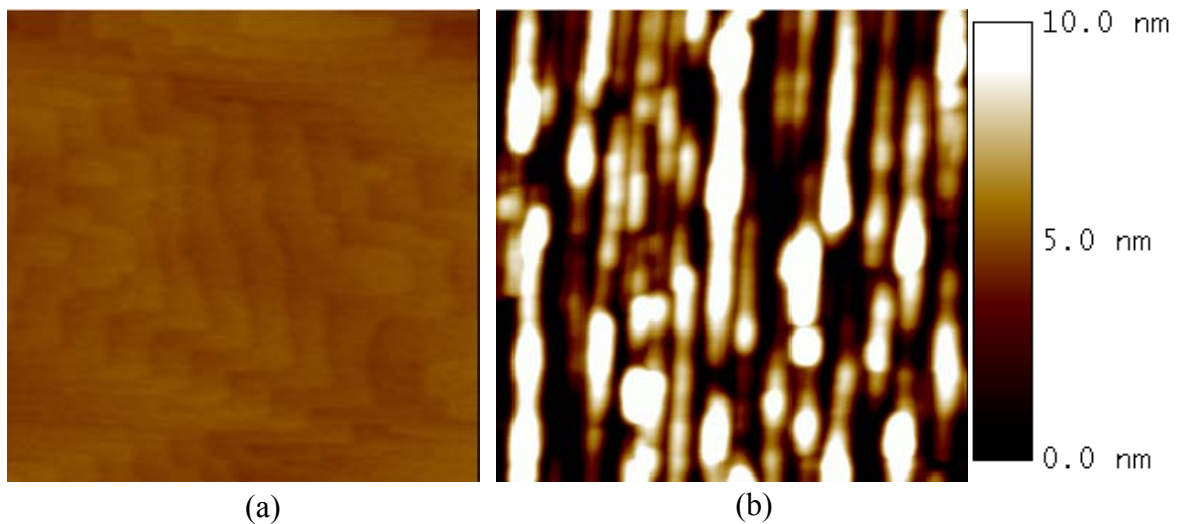


Figure 5-5. $1\times 1\ \mu\text{m}^2$ AFM height images showing the typical surface morphologies of smooth surface with triangle shaped features (a) and rough surface (b).

5.3.3 Confirmation of Bi incorporation

RBS measurements are carried out to examine Bi incorporation in these samples and the results of four samples are presented in Fig. 5-6 (a). Compared with the

Ref sample, a peak/step-like signal is observed at the channel value of around 480 and its intensity increases with T_g . This signal is a strong evidence of Bi incorporation. From the simulations, the Bi concentration of 0.2%, 0.7% and 0.7% is deduced for the $\text{GaSb}_{1-x}\text{Bi}_x$ samples grown at 360 °C, 370 °C and 390 °C, respectively, indicating a trend of Bi saturation at high temperatures. RBS channeling measurement is performed for the sample grown at 390 °C. The channeled spectrum is compared with two random spectra as shown in Fig. 5-6 (b). By evaluating the yield difference, about 65% of the incorporated Bi atoms are estimated to be at substitutional sites. The rest Bi atoms are either interstitials or accumulated on surface.

SIMS measurements are carried out in parallel with the RBS to show the relative counts of elements along the depth in a sample. Figure 5-6 (c) shows depth profiles of the three key elements Ga (69), Sb (121) and Bi (209) as well as In (115) and As (75) which may remain in the MBE growth chamber as background species. The initial intensity changes within 20-25 nm are artifacts. A clear step of Bi intensity at the interface between the epitaxial $\text{GaSb}_{1-x}\text{Bi}_x$ layer and the GaSb substrate, corroborated by the background As and In steps at the same depth ensures that the Bi signal is reliable although its intensity is relatively low. It is possible for the Bi signal to be interfered by Ga isotopes due to atomic mass superimposition ($\text{Ga } 69 + \text{Ga } 70 + \text{Ga } 70 = 209$). However, no correlation can be found between the Ga isotopes and Bi curves, proving again the reliability of the Bi results. Background As is detected from the growth chamber. It is about one order of magnitude higher than the value found in GaSb substrates and is similar for both the Ref sample and the GaSbBi samples grown in the range of 330-390 °C. Figure 5-6 (d) summarizes the Bi distribution profile in four samples showing a step for Bi intensity at the same position. Strong Bi surface accumulation is clearly observed for the samples grown at 370 and 390 °C. The Bi level increases following T_g (also Bi BEP) up to the maximum growth temperature of 390 °C. However, the difference between 370 °C and 390 °C is rather small, indicating saturation of Bi incorporation. This saturation results from the balance between the increased Bi BEP, the weak Ga-Bi bonding and the enhanced Bi segregation at high growth temperatures. Due to the lack of pure GaBi for calibration, it is very difficult to obtain the exact Bi concentration in these samples. Comparisons are made relatively. For example, the average incorporated Bi level in the $\text{GaSb}_{1-x}\text{Bi}_x$ layer grown at 370 °C is 1.45 times compared with that grown at 360 °C. This difference is smaller than that deduced from the RBS measurement confirming the relatively high percentage of Bi surface accumulation in the sample grown at 370 °C. We can thus conclude that, by combining the results of RBS and SIMS measurements, Bi incorporation is unambiguously demonstrated, Bi concentration in the $\text{GaSb}_{1-x}\text{Bi}_x$ layer increases with Bi BEP and tends to saturate at the growth temperature above 370 °C.

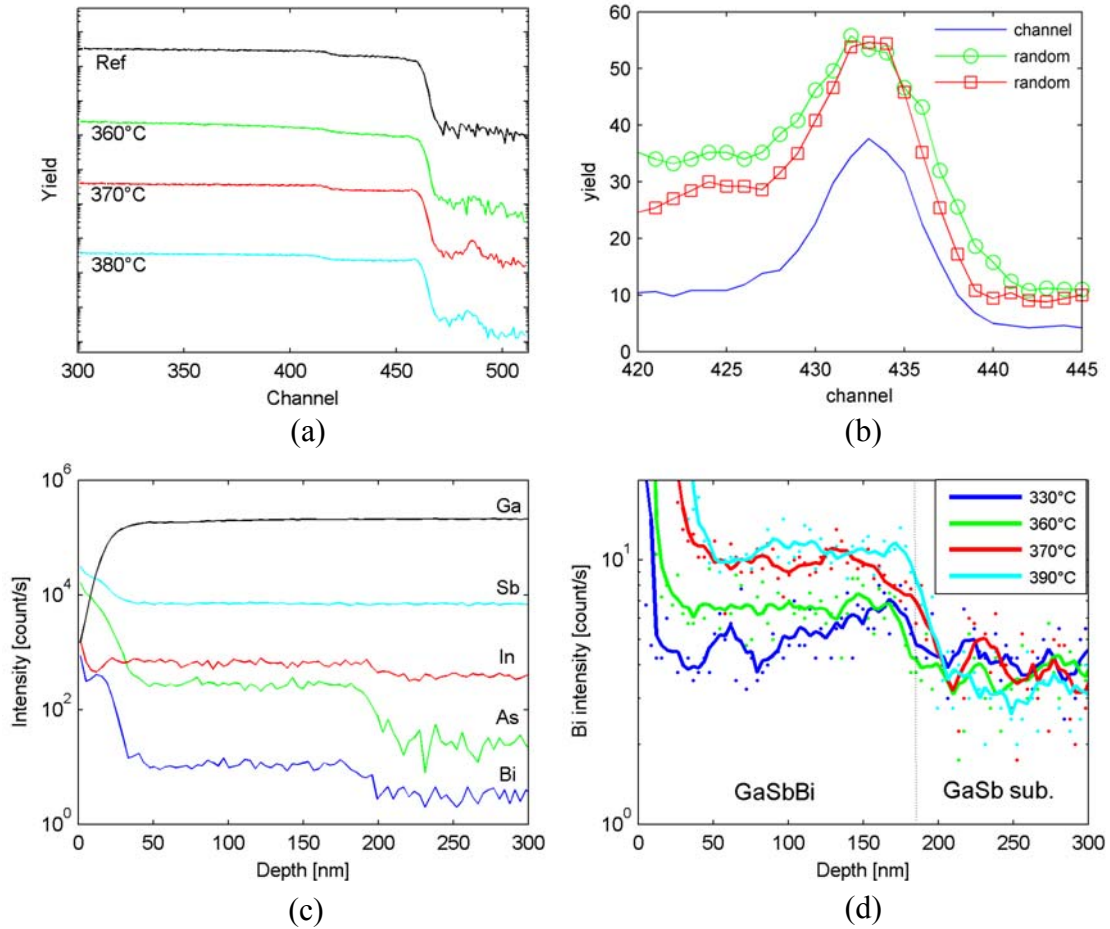


Figure 5-6. (a) RBS spectra of the Ref sample and the samples grown at 360 °C, 370 °C and 390 °C. (b) RBS channeling result (focusing on the Bi signal) for the sample grown at 390 °C. The green circled and red squared curves are from two random measurements and the blue solid curve is from the channeled measurement. (c) SIMS profiles of different elements in the sample grown at 390 °C. (d) Bi profiles from SIMS in the GaSb_{1-x}Bi_x samples. Dots are measurement data and the solid curves are obtained from five-point-smoothing of the measurement data.

5.3.4 Lattice contraction

As GaBi is predicted to have a larger lattice constant (6.324 Å [121]) than that of GaAs (5.653 Å) and GaSb (6.096 Å), the lattice constant of GaAs_{1-x}Bi_x and GaSb_{1-x}Bi_x is expected to be between the values of the constituent binaries. Fitting of GaAs_{1-x}Bi_x layer peak in an XRD rocking curve has been utilized as a convenient and accurate tool to measure the Bi composition in GaAs_{1-x}Bi_x materials [122], [110]. However, the GaSb_{1-x}Bi_x signals in XRD (004) rocking curves are found at the right side of the GaSb substrate peak as shown in Fig. 5-7 (a), indicating smaller lattice constants of GaSb_{1-x}Bi_x thin films than that of GaSb.

When the T_g increases from 330 °C to 380 °C (correspondingly the Bi BEP from 1e-8 Torr to 1e-7 Torr), the separation between the $\text{GaSb}_{1-x}\text{Bi}_x$ and the GaSb substrate peak increases as well. Clear interference fringes between the $\text{GaSb}_{1-x}\text{Bi}_x$ layer and the GaSb substrate can be found for samples with T_g lower than 380 °C, indicating high interface quality. In order to rule out the possibility that this $\text{GaSb}_{1-x}\text{Bi}_x$ peak is an illusion caused by crystal plane tilting, XRD (004) scans with sample rotation angles of 0°, 90°, 180° and 270° are implemented. All the curves have exactly the same shape. XRD (115) and (11-5) scans with sample rotation angles of 0° and 180° are also carried out. Free standing lattice constants of the $\text{GaSb}_{1-x}\text{Bi}_x$ layer are estimated. Compared with the lattice constant of GaSb: 6.096Å, lattice contraction of 0.034%, 0.061%, 0.079%, 0.084% and 0.041% are found for the sample grown at 330 °C, 360 °C, 370 °C, 380 °C and 390 °C, respectively. Except for the sample grown at 390 °C, the trend of lattice contraction well follows the Bi concentration deduced from RBS and SIMS measurements as shown in Fig. 5-7 (b). The lattice constant of $\text{GaSb}_{1-x}\text{Bi}_x$ layer reduces with increasing T_g /Bi BEP and increases when T_g is above 380 °C.

As discussed in Paper [E], possible reasons for similar lattice contraction found in $\text{InSb}_{1-x}\text{Bi}_x$, $\text{InTl}_x\text{As}_{1-x}$ and $\text{InTl}_x\text{Sb}_{1-x}$, such as Lanthanoid contraction [123] and lattice transformation from zincblende to tetragonal structure [24], can be ruled out. We propose that the lattice contraction is due to vacancies at group-V sites caused by Bi segregation, as illustrated in Fig. 5-8. Surface segregation is a well known phenomenon for group-III elements in ternary III-III-V compounds like In in InGaAs [92] as well as group-V elements in III-V-V system like Sb in $\text{GaAs}_x\text{Sb}_{1-x}$ [124]. Compared with Sb, Bi is metallic and has a larger atomic radius, larger atomic mass and weaker bonding energy with group-III elements. Bismuth is also a well known surfactant for growth of InGaAs with a complete layer of Bi atoms floating on the growing surface to minimize the system energy [128]. Therefore, Bi atoms should be very easy to segregate to the surface during the growth if the Bi surface coverage is less than a monolayer. As a result, there is significant surface accumulation of Bi atoms and the SIMS results from the GaSbBi samples grown at 370 °C or above shown in Fig. 5-6 (d) support this assumption. As mentioned above, in order to realize efficient Bi incorporation, a very low Sb flux must be used, leading to a quasi-Ga-rich growth condition for $\text{GaSb}_{1-x}\text{Bi}_x$. When a certain amount of the incorporated Bi atoms are segregated to the surface, there are no enough excess Sb atoms available to fill in the vacant sites left by the segregated Bi atoms. Then, there are three possibilities as sketched in Fig. 5-8, Ga and background As atoms will take the sites forming Ga_v anti-site defects or GaAsSbBi , respectively, or the vacancies will be buried in the $\text{GaSb}_{1-x}\text{Bi}_x$ layer. All the cases will lead to a smaller lattice constant as it would be for $\text{GaSb}_{1-x}\text{Bi}_x$. Vacancies are the most effective in reducing the lattice constant than the other two possibilities. If the amount of vacancies is high, they can eventually compensate the incorporated Bi causing lattice contraction. Background As atoms are also possible to fill in the vacancies and results in lattice contraction. However, this

shouldn't be the major factor, because the measured As level by SIMS in all these samples are similar and very low.

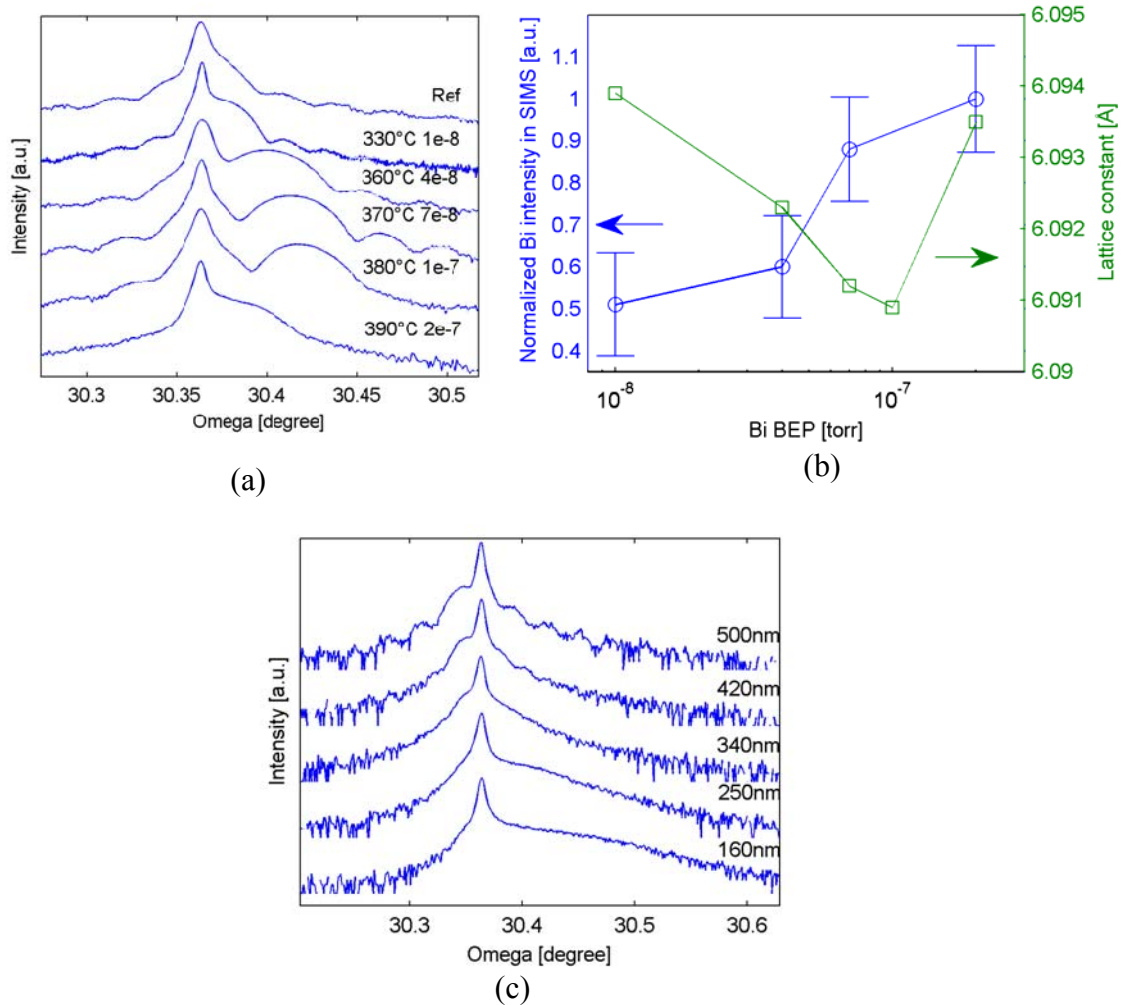


Figure 5-7. (a) XRD (004) rocking curves of the samples (logarithmic scale). Labels to the low-right of each curve indicate the growth temperature and the Bi BEP. (b) Trends of the relative Bi concentration obtained from SIMS measurements and the lattice constant of the GaSb_{1-x}Bi_x samples deduced from XRD. (c) XRD (004) rocking curves of a thick sample (500 nm) grown at 380 °C with different etch depths. The labels above each curve indicate the remaining layer thickness from the interface.

Surface segregation effect is usually enhanced at high growth temperatures. Fig. 5-7 (b) compares the trend of Bi concentration obtained from SIMS measurements and the deduced lattice constant of the GaSb_{1-x}Bi_x samples from XRD. When T_g increases from 330 °C up to 380 °C, we expect that Bi segregation increases as well, leading to more vacancies and stronger lattice contraction. Bi segregation also depends on surface coverage of Bi atoms. From SIMS results in Fig. 5-6 (d), Bi surface accumulation increases with growth temperature and is the highest for

the sample grown at 390 °C. A large Bi surface coverage will suppress the Bi segregation, which is the case for the $T_g=390$ °C sample. From the SIMS measurement, the Bi level in this sample is similar to that of the sample grown at 370 °C, but the lattice constant of the $\text{GaSb}_{1-x}\text{Bi}_x$ layer increases. This implies that the suppressed Bi segregation induces fewer vacancies which can't effectively compensate the incorporated Bi atoms in this particular sample. The incorporated Bi atoms will thus stay at the lattice sites in the $\text{GaSb}_{1-x}\text{Bi}_x$ layer leading to smaller lattice contraction.

A 500 nm thick $\text{GaSb}_{1-x}\text{Bi}_x$ layer is grown at 380 °C under the identical growth conditions as the 200 nm thick sample. To the contrary, the $\text{GaSb}_{1-x}\text{Bi}_x$ layer peak appears at the left side of the GaSb substrate, which is shown as the top curve in Fig. 5-7 (c), indicating a larger lattice constant as expected. To evaluate the evolution of lattice constant with the $\text{GaSb}_{1-x}\text{Bi}_x$ layer thickness, we etch down the sample at four different depths. As found in Fig. 5-7 (c), the $\text{GaSb}_{1-x}\text{Bi}_x$ peak moves towards the GaSb substrate peak and eventually to the right side and becomes lower and broader at the same time when the $\text{GaSb}_{1-x}\text{Bi}_x$ layer thickness is reduced. The interference fringes are observed in the un-etched sample, but lost in the etched samples due to the rough etched surface. This observation supports the model discussed above. Bi segregation occurs in the beginning of the $\text{GaSb}_{1-x}\text{Bi}_x$ growth leading to lattice contraction. It becomes weak with the film thickness and eventually stops when the Bi surface accumulation is high enough. For later growth, the incorporated Bi atoms will occupy lattice sites causing lattice dilation as expected.

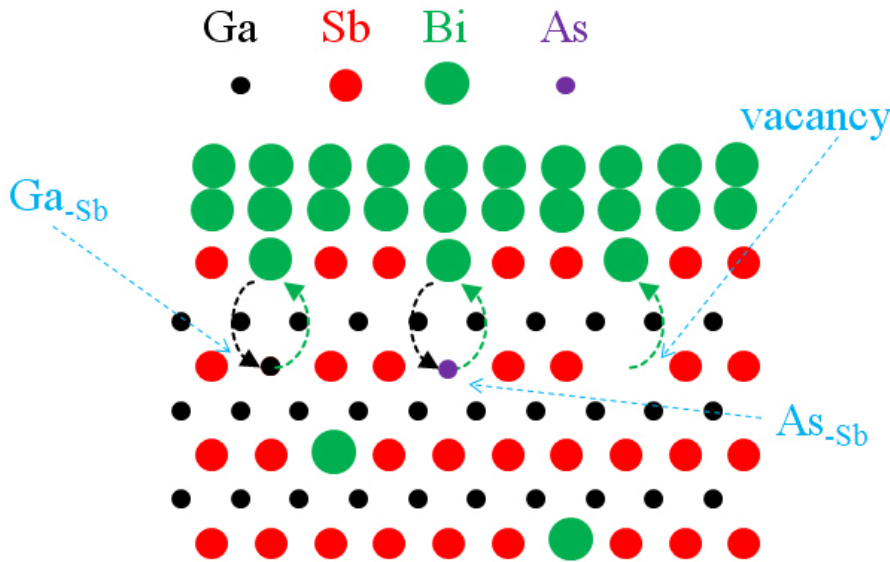


Figure 5-8. Schematic of possible formation of defects, i.e. vacancy and antisite, due to Bi segregation during growth of $\text{GaSb}_{1-x}\text{Bi}_x$.

5.3.5 GaSb_{1-x}Bi_x on GaAs substrates.

Samples with the same growth conditions are also grown on un-doped GaAs (100) substrates for comparison. No apparent difference in Bi incorporation is found within the accuracy of SIMS measurements. However, the surface of the samples grown on GaAs substrates is much worse than those grown on GaSb substrates due to the large lattice mismatch.

5.4 MBE growth and characterization of InSb_{1-x}Bi_x

5.4.1 Sample structure and growth

As we don't have InSb substrates available, all InSb_{1-x}Bi_x samples are grown on undoped (100) GaAs substrates by MBE. To accommodate the large lattice mismatch, an intermediate 200 nm thick fully relaxed GaSb layer is grown at 510 °C utilizing the interfacial misfit method [59] to obtain a low TD density and a smooth surface. The growth temperature is then reduced to 280 °C to initiate growth of a 30 nm InSb buffer layer which is enough to recover from a dotted to a streaky pattern judged by RHEED. Then, the growth temperature is increased to the range between 355°C and 395°C and a 150 nm thick InSb_{1-x}Bi_x layer is grown at 0.2 μm/h. The Sb BEP is set to be 4.2e-7 Torr, which is 10% more than the critical Sb BEP value required to protect InSb surface from degradation judged by RHEED. The selection of Bi BEP follows the same strategy as for the GaSb_{1-x}Bi_x samples, *i. e.* close to the vapor pressure at a particular growth temperature. Two reference (Ref) samples of 150 nm thick InSb without Bi is grown at 360 °C and 385 °C for comparison.

5.4.2 Surface morphology

Figure 5-5 shows 10x10 μm² AFM scans of both Ref and InSbBi samples. Smooth surface with visible atomic steps in 1x1 μm² scans (not shown) is observed for the InSb_{1-x}Bi_x sample grown at 355 °C and the Ref sample grown at 360 °C with a RMS roughness value of 0.26 nm and 0.34 nm, respectively. The surface is getting rough with 3D features at high growth temperatures in both cases. Discrete platform-like features together with holes are observed on the Ref sample grown at 385 °C, indicating non-uniform growth rate in different regions. Adding Bi results in larger 3D structures with irregular shapes compared with the Ref samples grown at the same temperatures. Figure 5-2 summarizes the RMS roughness values measured from both 1×1 μm² and 10×10 μm² scans. It increases with growth temperature. The InSbBi has rougher surface than the InSb Ref samples but the difference in the 1x1 μm² scans is small.

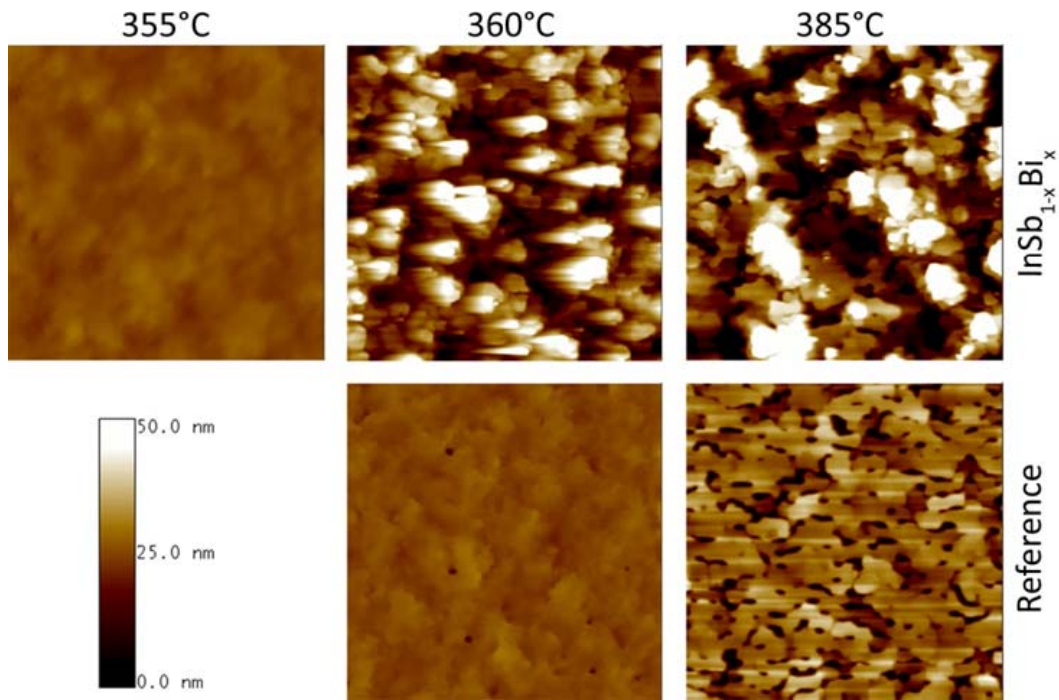


Figure 5-9. $10 \times 10 \mu\text{m}^2$ AFM images of InSb_{1-x}Bi_x samples. The first row shows the InSb_{1-x}Bi_x samples and the second row the reference samples.

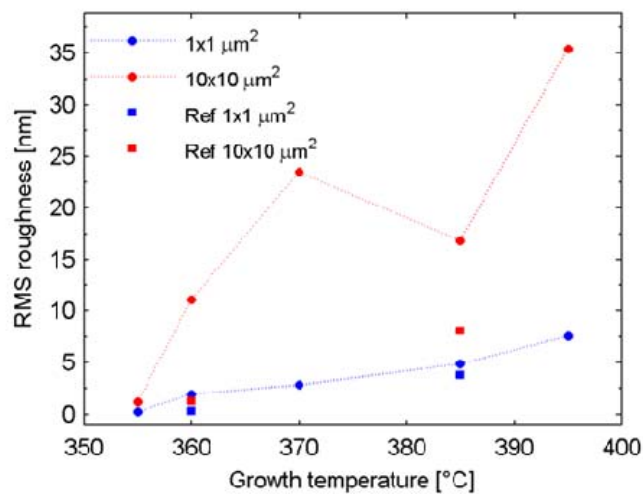


Figure 5-10. Summary of RMS roughness values of InSbBi and reference samples.

5.4.3 Structural properties

Cross sectional bright field TEM measurements are carried out for the InSb_{1-x}Bi_x sample grown at 370 °C and the reference sample grown at 360 °C as shown in Figure 5-11. The GaSb buffer grown by the IMF method shows high structural

quality with smooth interface and few TDs for both the Ref and the InSb_{1-x}Bi_x sample. The strain is almost fully relaxed through formation of periodical MDs at the GaSb/GaAs interface (observable at high magnifications). Most strain in the InSb(Bi) layer is found to be relaxed by formation of an MD array at the InSb/GaSb interface, but a much larger TD density ($>10^9 \text{ cm}^{-2}$) is observed in this layer. Holes are observed in some places accompanied by etched GaSb underneath. Reasons are unclear at the moment and we speculate that they are related to Bi droplets formed on surface that etch away the GaSb layer.

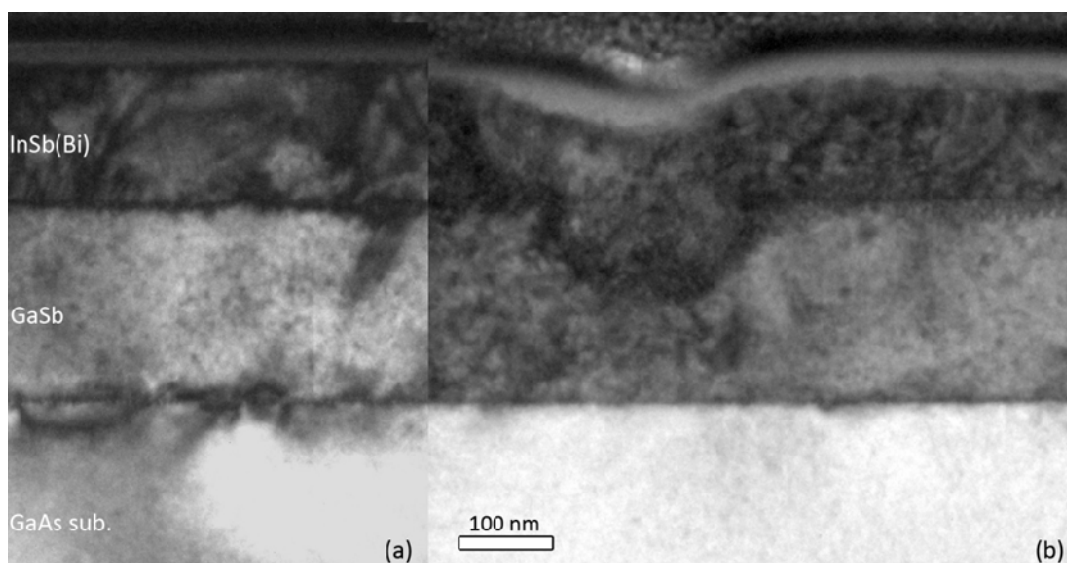


Figure 5-11. Cross-sectional bright field TEM images of (a) reference sample grown at 360 °C and (b) InSb_{1-x}Bi_x sample grown at 370 °C.

Figure 5-4 shows XRD (004) rocking measurements of InSb_{1-x}Bi_x samples. The right peaks are from GaAs substrates, the middle peaks are from the GaSb buffer layers while the left broadened peaks are from the 30 nm thick InSb grown at 280 °C and the 150 nm thick InSb_{1-x}Bi_x (InSb for the Ref sample) layer grown at higher temperatures. Even for the Ref sample, clear peak splitting is observed for only one material, InSb, without Bi. Curve fitting using two Gaussian profiles is performed and the result is shown in Fig. 5-12 (b). The right low broad peak is believed to be from the 30 nm InSb grown at 280 °C while the left high narrow peak is from the 150 nm of InSb grown at 360 °C. The dashed line marks the position of ideally fully relaxed InSb. The thick InSb peak appears at the left side of the dashed line, indicating 98% strain relaxation. The thin InSb peak can be found at nearly the same position for InSb_{1-x}Bi_x layers grown from 355 to 385 °C. Its low intensity and broad linewidth evidence a high structural defect density and possible In/Ga intermixing forming InGaSb near the InSb/GaSb interface. The peak from the 150 nm of InSb_{1-x}Bi_x of all InSb_{1-x}Bi_x samples appears at the right side of the 30 nm InSb peak except for the one grown at 355 °C and with the lowest Bi BEP (3e-8 Torr). The lattice contraction phenomenon of the InSb_{1-x}Bi_x

layers is similar to that found in GaSbBi, but mechanisms are different and more complicated in InSbBi. Not only Bi induced vacancies as discussed in the case of GaSbBi, but also Bi enhanced In/Ga intermixing can result in non-uniform and partially relaxed 150 nm thick InGaSbBi alloys along the growth direction leading to strong broadening and right shift of the XRD peak. In addition, the 30 nm InSb peak of the $\text{InSb}_{1-x}\text{Bi}_x$ sample grown at 395 °C is right shifted indicating strong Ga/In intermixing at this temperature.

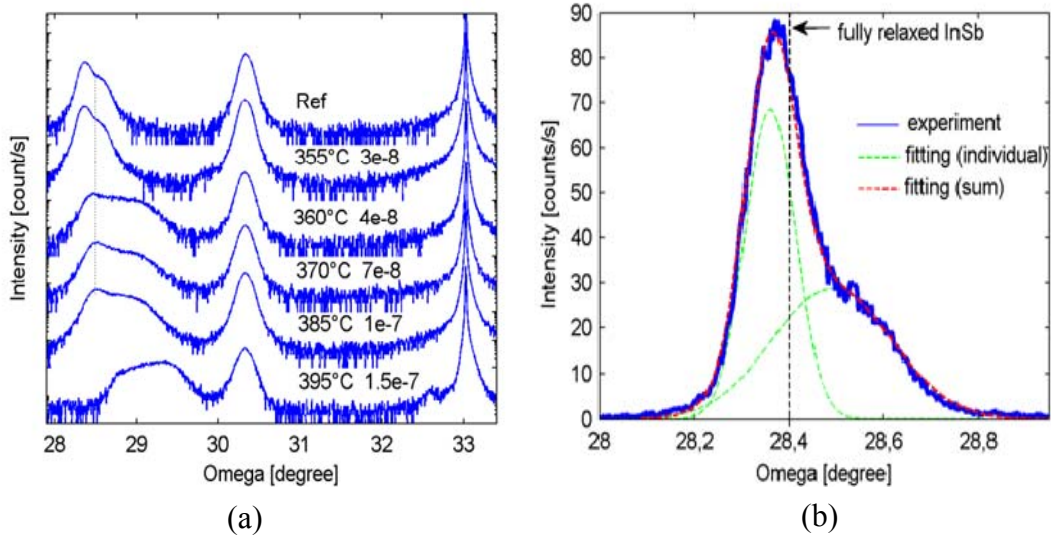


Figure 5-12. (a) XRD (004) rocking curves of InSbBi samples. The dashed line marks the position of the 30 nm InSb grown at 280 °C. (b) Two-Gaussian curve fitting for the InSb peak of the Ref sample grown at 360 °C.

5.4.4 Bi incorporation

RBS measurements are carried out to examine Bi incorporation and the results of four samples are summarized in Fig. 5-13 (a). Compared with the Ref sample, a peak/step-like signal can be observed at the channel value of around 480 for all the $\text{InSb}_{1-x}\text{Bi}_x$ samples (not very obvious for the one grown at 355 °C). This signal is a strong evidence of Bi incorporation. From the simulations, the deduced Bi concentrations are summarized in Fig. 5-13 (b). The highest Bi percentage is measured to be 2% in the sample grown at 370 °C. RBS channeling measurements are performed for two $\text{InSb}_{1-x}\text{Bi}_x$ samples. By evaluating the yield difference, about 70 % and 57 % of the incorporated Bi atoms are estimated to be at substitutional sites for the $\text{InSb}_{1-x}\text{Bi}_x$ layers grown at 360 and 385 °C, respectively.

A simulated curve based on sharp interfaces is also shown in Fig. 5-13 (a). A clear trend can be found that the steps in the measured curves become blunter when growth temperature increases, indicating interface roughening.

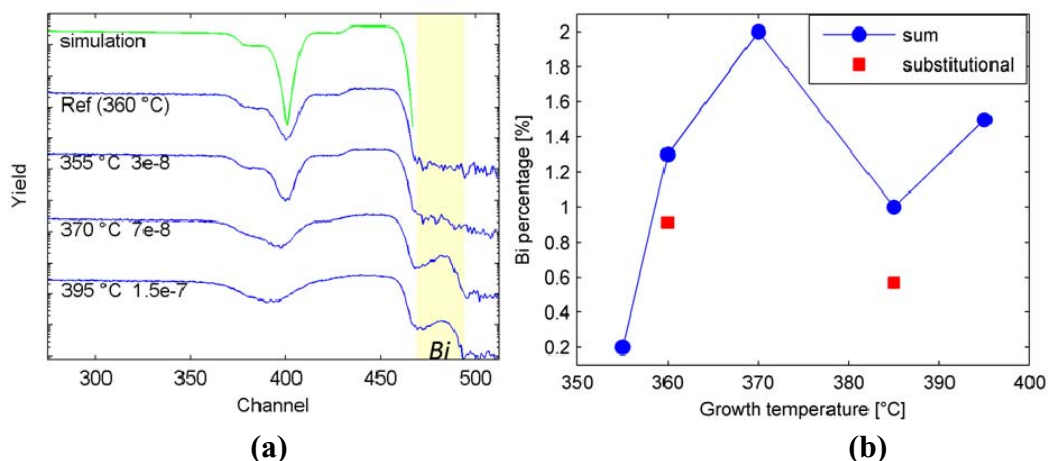


Figure 5-13. (a) RBS spectra of InSbBi samples. The green curve is the simulation based on sharp interfaces without Bi. The yellow belt marks the signal region from Bi. (b) Bi concentrations in total (blue round) and at substitutional sites (red square).

SIMS measurements are carried out in parallel with the RBS measurements as antitheses and the results are summarized in Fig. 5-14. Figure 5-14 (a) shows the Bi profiles for InSbBi samples grown at 355, 370 and 395 °C. Clear Bi incorporation is observed, however the Bi distribution is not uniform. The Bi composition decreases within thickness in the first 100 nm thick InSbBi layer (Only the data from the very top (~30 nm) of the sample can be disturbed by stabilization process of the SIMS equipment.) Surprisingly a big Bi signal in the GaSb layer is found in the samples grown at 370 and 395 °C. It is suspected to be related to the Bi droplets as the one shown in Fig. 5-11 (b).

5.4.5 Bi induced In/Ga intermixing

Two different kinds of ions are used in the SIMS measurement. The positive Cs ions are firstly tried. It provides high depth resolution, but low sensitivity for Bi atoms. The negative O_x ions, on the other hand, are about one magnitude more sensitive on Bi atoms than the positive Cs ions. Therefore, in the later measurements for InSb_{1-x}Bi_x samples, the negative O_x ions are chosen. Figure 5-14 (b) shows the profiles measured by positive Cs ions of all involved elements in the two Ref samples grown at 360 °C and 385 °C, respectively, and the InSb_{1-x}Bi_x sample grown at 355 °C (log scale). The InSbBi grown at 355 °C shows a higher In content in the GaSb region and a higher Ga content in the InSb(Bi) region than those found in the Ref sample grown at 360 °C, but similar In and Ga profiles as those found in the Ref sample grown at 385 °C, giving direct evidence of Bi induced In/Ga intermixing. No large difference regarding interface broadening is found in all the three samples.

The Bi induced In/Ga intermixing in InSbBi/InSb/GaSb is enhanced with increasing growth temperature as seen in Fig. 5-14 (c). The InSbBi grown at

355 °C shows clear steps of both In and Ga profiles (normalized linear scale) at the InSb_{1-x}Bi_x/InSb/GaSb interface with small In/Ga intermixing. When the growth temperature is high, the steps become blunted indicating very strong In/Ga intermixing. This is consistent with lattice contraction of the InSb_{1-x}Bi_x layer observed in XRD. When the growth temperature reaches 395°C, a high tail of the Ga signal can be found even at the top of the InSb_{1-x}Bi_x layer while In atoms can diffuse into the GaAs substrate. The mixed InGaSb alloy explains the broad peak in the XRD rocking curves with a smaller lattice constant than InSb. To the contrary, much less intermixing of group-V atoms is observed as shown in Fig. 5-14 (d).

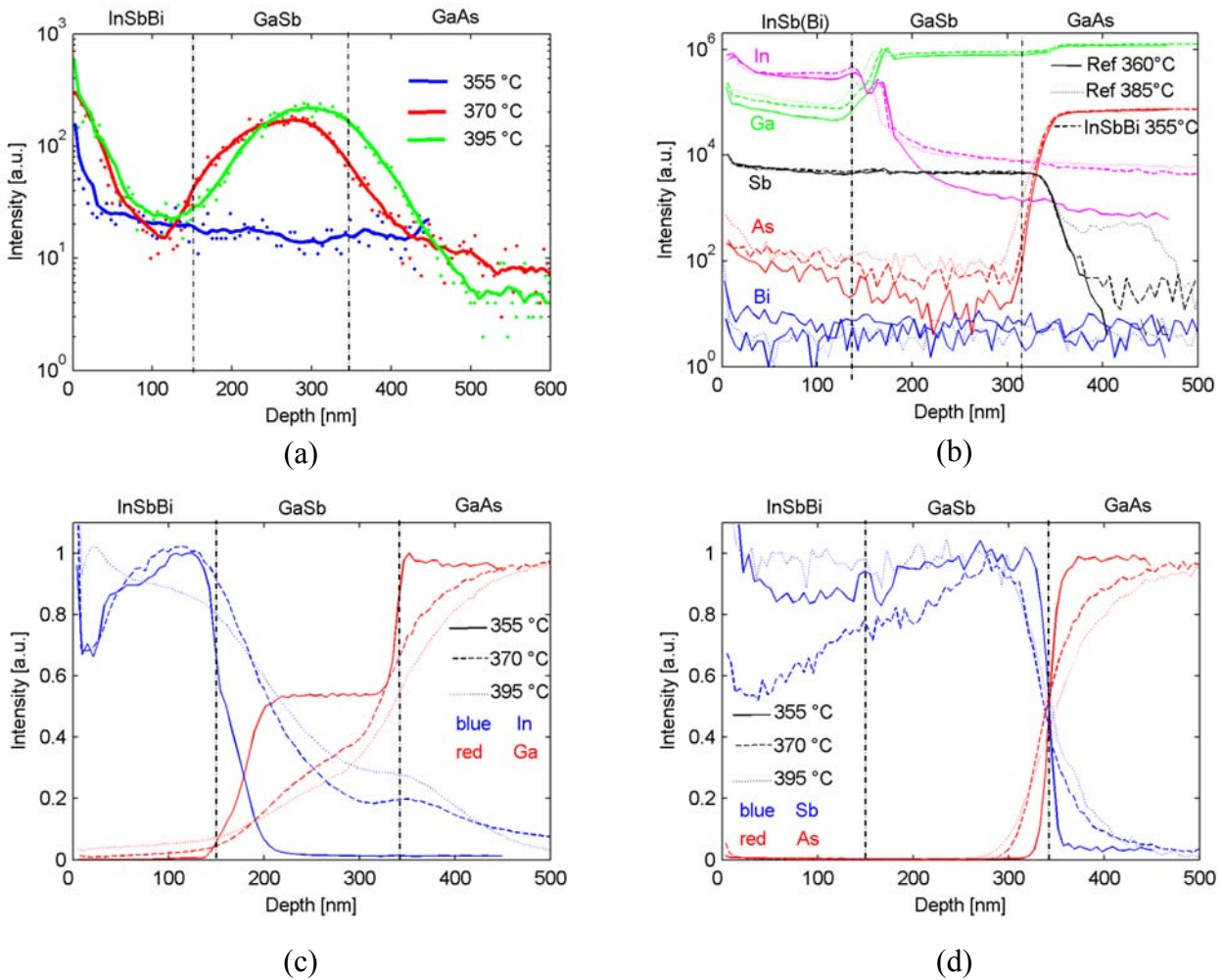
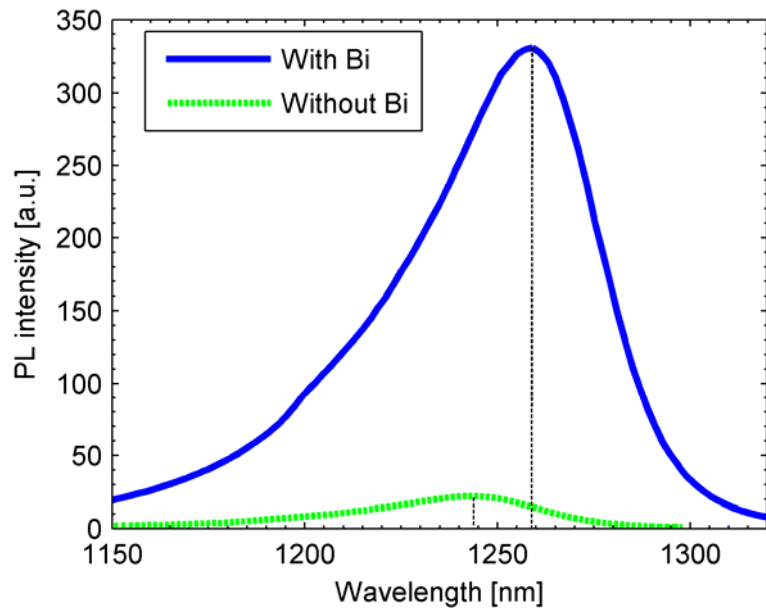
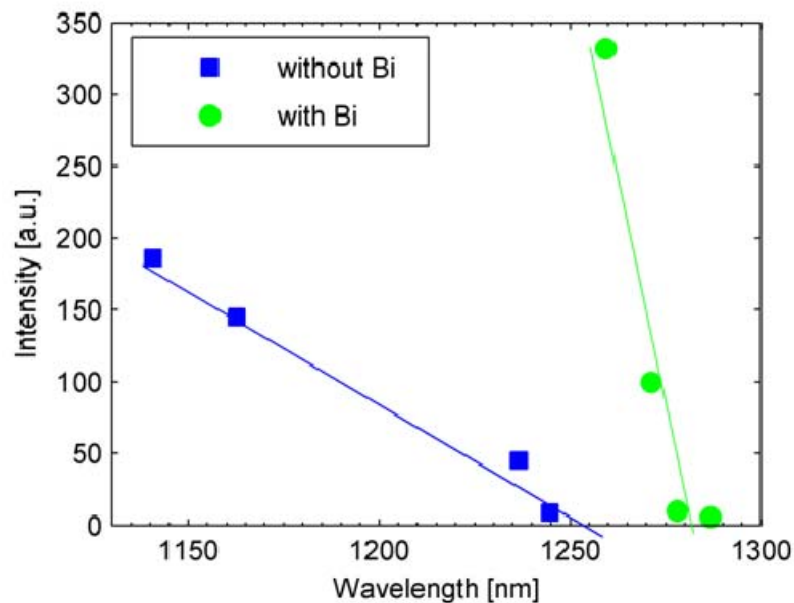


Figure 5-14. SIMS results of the InSb(Bi) samples. (a) Bi profiles of the InSb_{1-x}Bi_x samples grown at 355 °C, 370 °C and 395 °C measured by negative O_x ions. The dots are measured data points and the curves are five point smoothed results. (b) Element profiles measured by positive Cs ions of the two reference samples grown at 360 °C and 385 °C, respectively, and the InSb_{1-x}Bi_x sample grown at 355 °C. (c) and (d) show normalized profile of In/Ga and As/Sb measured by negative O_x ions in linear scale, respectively, for the InSb_{1-x}Bi_x samples grown at 355 °C, 370 °C and 395 °C.

5.5 Bismuth as surfactant for InGaAs QW on GaAs



(a)



(b)

Figure 5-15. (a) PL spectra of two identical InGaAs QWs with (blue solid) and without (green dashed) Bi as surfactant. (b) PL results of InGaAs QWs with (round) and without (square) Bi as surfactant. The lines are linear fit for the data points.

InGaAs QW lasers emitting at 1.3 μm on GaAs substrate is very attractive to improve temperature stability [41]. However, InGaAs QWs can't reach 1.3 μm rather stop at 1.24 μm [125] due to the large lattice mismatch. Surfactant-mediated growth has been found to extend the critical thickness for strain relaxation during

the growth of heterostructures with lattice mismatch [126]. Utilizing Bi as the surfactant during the growth of highly strained InGaAs QWs on GaAs substrates, we have successfully realized high PL intensity from InGaAs:Bi QWs with wavelength $>1.26 \mu\text{m}$, which is the lower limit of the O-band for optical fiber communication, and a maximum wavelength of $1.282 \mu\text{m}$ at 300 K. Figure 5-15(a) shows the PL spectra of two identical QWs with the same structure and In composition. Utilizing Bi as surfactant during the growth of the QW results in 15 times PL intensity increase and 15 nm wavelength red-shift. Figure 5-15(b) summarizes the PL results of all samples. The blue and red data points are from InGaAs QWs without and with Bi as surfactant. It is clearly seen that QWs with Bi as surfactant show higher intensity for the same wavelength, and can reach longer wavelength. We attribute this to the Bi surfactant effect which suppresses the strain relaxation by formation of 3D islands. As the growth temperature of the QWs is around $440 \text{ }^\circ\text{C}$, little Bi incorporation is expected [118].

6 Summary of appended papers

Group I: Paper [A] and Paper [B]

Doping effects in InGaAs alloy graded metamorphic buffers.

Paper A: The role of *n*- and *p*-type doping in strain relaxation of graded composition InGaAs layers grown by MBE is investigated. It is found that *p*-type Be-doping can improve material properties, resulting in smaller surface roughness and lower threading dislocation density, while *n*-type Si-doping has an opposite effect. The effect is strongly dependent on the grading profile, with linear grading showing small differences, while there is a significant difference when an exponential grading is used. I have performed AFM and XRD measurements on all the samples and been involved in data analysis, discussion and writing.

Paper B is a continuation of the work presented in Paper A. In this paper, the effects of doping and grading slope on surface and structure of linearly alloy graded InGaAs buffers are carefully investigated. Again the Be doping is found to improve material properties, resulting in smaller surface roughness and a lower threading dislocation density, while the Si doping has an opposite effect. The effect is strongly dependent on the grading slope. A moderate In grading slope is preferable for strain relaxation and minimization of the negative effect of Si doping. I have performed AFM and XRD measurements on all the samples, been involved in data analysis and discussions, and written the paper.

Group II: Paper [C] and Paper [D]

TD filtering and optical property enhancement for metamorphic QWs by dilute nitride.

In **Paper C**, we proposed a new method making use of the hardening effect of dilute nitrides to filter out threading dislocations in alloy graded metamorphic layers. We demonstrate 3.7 and 5.4 times enhancement of photoluminescence intensity from the metamorphic quantum wells when using dilute nitride superlattice alone or by adding nitrogen in a strain compensated GaAs/ In_{0.3}Al_{0.7}As superlattice, respectively. I have performed AFM, PL and XRD on all the samples, been involved in data analysis and discussions, and written the paper.

Paper D is the extension for the work reported in Paper C, showing details in structure designs, growth procedures, detail characterization results and discussions. I have been involved in structure designs, data analysis and discussions, performed AFM, PL and XRD on all the samples, and written the paper.

Group III: Paper [E]

MBE growth of InAs/GaSb T2SL materials.

In **Paper E**, we report MBE growth and optimizations of InAs/GaSb T2SL structures for mid-wavelength IR photodetectors. Different strain compensation schemes with insertion of InSb layers are proposed and tested to be efficient to tune the overall strain from tensile to compressive, and their structural and optical properties are compared. The effect of the proposed methods is modeled by analytic functions and the band structure calculations are performed to assist optimizing sample designs. Single pixel photodiodes with low dark currents are demonstrated. I have grown all the samples by MBE, performed XRD and Hall measurements, involved in structure design, analysis of strain compensation and discussions, and written the paper.

Group IV: Paper [F] and Paper [G]

MBE growth and characterization of GaSb_{1-x}Bi_x.

In **Paper F**, we report details of MBE growth of GaSb_{1-x}Bi_x. The growth window for Bi incorporation is studied, and surface and structural properties are investigated. Bismuth incorporation is confirmed by SIMS and RBS measurements. I have grown all the samples by MBE, involved in structure designs, data analysis and discussions, performed AFM and XRD on all the samples, and written the paper.

In **Paper G**, we report for the first MBE growth of GaSb_{1-x}Bi_x thin films and discover the lattice contraction phenomenon observed in this material. Bismuth incorporation is confirmed by RBS and SIMS measurements. Lattice contraction is observed from XRD showing tensile strain rather than compressive strain as it would be expected. I have grown all the samples by MBE, involved in structure designs, data analysis and discussions, performed AFM and XRD on all the samples, and written the paper.

Appendix

A1 In segregation in alloy graded InGaAs buffers

J. M. Muraki *et al* proposed a model to simulate the In segregation process in uniform III/V ternary compounds based on an iterative method [92]. We developed this model to simulate the situation in alloy graded $\text{In}_x\text{Ga}_{1-x}\text{As}$ buffers.

We assume the In segregation process involves only the top mono-layer of the under-growth structure and the being deposited mono-layer. Then assume that for the top monolayer, a portion of η of the In atoms will be segregated to the growth front. η is basically a constant with a typical value around 0.8 for In segregation in InGaAs. Some variables are assigned for the derivation: x_i ($i=1, 2, 3 \dots$) is the In composition of the i -th deposited mono-layer. $C^{(i)}$ is the amount of In atoms above the i -th deposited mono-layer in terms of monolayer. The In atoms above the top mono-layer come from two sources: the segregated In atoms from the beneath mono-layer and the newly deposited In atoms which take up a portion of x of the total group III atoms. Then,

$$C^{(1)} = \eta x_1 \tag{A-1}$$

$$C^{(2)} = (C^{(1)} + x_2)\eta = \eta^2 x_1 + \eta x_2 \tag{A-2}$$

$$C^{(3)} = (C^{(2)} + x_3)\eta = \eta^3 x_1 + \eta^2 x_2 + \eta x_3 \tag{A-3}$$

⋮

$$C^{(i)} = (C^{(i-1)} + x_{i+1})\eta = \eta^i x_1 + \eta^{i-1} x_2 + \dots + \eta^2 x_{i-1} + \eta x_i \tag{A-4}$$

⋮

$$C^{(N)} = \eta^N x_1 + \eta^{N-1} x_2 + \dots + \eta^2 x_{N-1} + \eta x_N \tag{A-5}$$

where, N is the total number of mono-layers of the alloy graded buffer, and $C^{(N)}$ means the total amount of In above the alloy graded buffer.

The “x” in the equations above depends on the grading profile. In the case of a LAG buffer,

$$x_i = i \frac{x_0}{N} \quad (\text{A-6})$$

where x_0 is the final In composition of the graded buffer. Eq. (A-5) can be further simplified as follow:

$$\begin{aligned} C^{(N)} &= \eta^N x_1 + \eta^{N-1} x_2 + \dots + \eta^2 x_{N-1} + \eta x_N \\ &= \eta^N \frac{x_0}{N} + \eta^{N-1} 2 \frac{x_0}{N} + \dots + \eta^2 (N-1) \frac{x_0}{N} + \eta N \frac{x_0}{N} \end{aligned} \quad (\text{A-7})$$

If we multiply a η to both sides of Eq. (A-7), we get

$$\eta C^{(N)} = \eta^{N+1} \frac{x_0}{N} + \eta^N 2 \frac{x_0}{N} + \dots + \eta^3 (N-1) \frac{x_0}{N} + \eta^2 N \frac{x_0}{N} \quad (\text{A-8})$$

Eq. (A-8) minus Eq. (A-7), we get

$$\begin{aligned} (\eta - 1)C^{(N)} &= \eta^{N+1} \frac{x_0}{N} + (\eta^N \frac{x_0}{N} + \eta^{N-1} \frac{x_0}{N} + \dots + \eta^3 \frac{x_0}{N} + \eta^2 \frac{x_0}{N}) - \eta N \frac{x_0}{N} \\ &= (\eta^{N+1} + \eta^N + \dots + \eta^2) \frac{x_0}{N} - \eta N \frac{x_0}{N} \\ &= \frac{\eta^{N+1} - (N+1)\eta + N}{1-\eta} \eta \frac{x_0}{N} \end{aligned} \quad (\text{A-9})$$

So,

$$C^{(N)} = \frac{\eta^{N+1} - (N+1)\eta + N}{(1-\eta)^2} \eta \frac{x_0}{N} \quad (\text{A-10})$$

Normally N is a very large number and η is always smaller than “1”, so $\eta^{N+1} \rightarrow 0$ and $\frac{1}{N} \rightarrow 0$. Then

$$C^{(N)} \approx \frac{\eta}{1-\eta} x_0 \quad (\text{A-11})$$

Therefore, the segregated amount of In atoms on top of a LAG buffer is only decided by the final In composition. However, Eq. (A-11) cannot reflect the kinetic process of In segregation during the growth of the graded buffer. If we

define α as the In grading slope, then the In composition at a distance of h from the substrate in the graded buffer is

$$x(h) = \alpha h \tag{A-12}$$

Based on Eq. (A-11), the In amount on the growth front when the graded buffer grows to a thickness of h can be expressed as

$$C(h) = \frac{\alpha\eta}{1-\eta} h \tag{A-13}$$

Although only the LAG profile is derived here, other grading profiles can be assumed to be a sum of many linear grading segments. So Eq. (3-3) can be implemented to predict the process of In segregation effect in other grading profiles during growth.

A2 Overall strain in T2SL structures

TABLE A-1 Expressions of the overall lattice mismatch for different strain compensation methods presented in Fig. 4-3.

Methods	Overall lattice mismatch
(a)	$f = \left[\left(M - 1 + \frac{x}{2} + \frac{y}{2} \right) f_{InAs} + \left(\frac{x}{2} + \frac{y}{2} + Nz' \right) f_{GaAs} + \left(\frac{1-x}{2} + \frac{1-y}{2} \right) f_{InSb} \right] / (M + N + 1)$ $f = (0.0691 - 0.0062M - 0.0709x - 0.0709y - 0.0726Nz') / (M + N + 1)$
(b)	$f = \left[\left(M - 1 + x + \frac{y}{2} \right) f_{InAs} + \left(\frac{y}{2} + Nz' \right) f_{GaAs} + \left(2 - x - \frac{y}{2} \right) f_{InSb} \right] / (M + N + 1)$ $f = (0.132 - 0.0062M - 0.0691x - 0.0709y - 0.0726Nz') / (M + N + 1)$
(c)	$f = \left[\left(M + \frac{x}{2} \right) f_{InAs} + \left(\frac{x}{2} + Nz' \right) f_{GaAs} + \left(1 - \frac{x}{2} \right) f_{InSb} \right] / (M + N + 1)$ $f = (0.0629 - 0.0062M - 0.0709x - 0.0726Nz') / (M + N + 1)$
(d)	$f = \left[\left(M - 1 + \frac{x}{2} + \frac{y}{2} \right) f_{InAs} + \left(\frac{x}{2} + \frac{y}{2} + Nz' \right) f_{GaAs} + \left(2 - \frac{x}{2} - \frac{y}{2} \right) f_{InSb} \right] / (M + N + 1)$ $f = (0.132 - 0.0062M - 0.0709x - 0.0709y - 0.0726Nz') / (M + N + 1)$

TABLE A-2. Expressions of the overall lattice mismatch for the combined strain compensation schemes.

Schemes	Overall lattice mismatch
(b)+ (c)	$f = [(M+x)f_{InAs} + (Nz')f_{GaAs} + (2-x)f_{InSb}] / (M+N+2)$ $f = (0.1258 - 0.0062M - 0.0691x - 0.0726Nz') / (M+N+2)$
(b)+ (d)	$f = \left[\left(M - 1 + x + \frac{y}{2} \right) f_{InAs} + \left(\frac{y}{2} + Nz' \right) f_{GaAs} + \left(3 - x - \frac{y}{2} \right) f_{InSb} \right] / (M+N+2)$ $f = (0.1949 - 0.0062M - 0.0691x - 0.0709y - 0.0726Nz') / (M+N+2)$
(c)+ (d)	$f = \left[\left(M + \frac{x}{2} \right) f_{InAs} + \left(\frac{x}{2} + Nz' \right) f_{GaAs} + \left(2 - \frac{x}{2} \right) f_{InSb} \right] / (M+N+2)$ $f = (0.1258 - 0.0062M - 0.0709x - 0.0726Nz') / (M+N+2)$
(b)+ (c)+ (d)	$f = [(M-1+x)f_{InAs} + (Nz')f_{GaAs} + (3-x)f_{InSb}] / (M+N+3)$ $f = (0.1887 - 0.0062M - 0.0691x - 0.0726Nz') / (M+N+3)$

References

- [1] A. Rogalski and K. Chrzanowski, "Infrared devices and techniques," *Opto-Electronics Review*, vol. 10, no. 2, pp. 111-136, 2002.
- [2] I. Ganga, B. Booth, H. Frazier, S. Muller, and G. Nicholl, "IEEE P802.3ba 40Gb/s and 100Gb/s Ethernet Task Force, May 2008 Meeting." [Online]. Available: <http://www.ieee802.org/3/ba/public/may08/index.htm>.
- [3] R. Ramaswami, "Optical fiber communication: from transmission to networking," *Communications Magazine, IEEE*, vol. 40, no. 5, pp. 138-147, 2002.
- [4] K. Volz et al., "Material Development for Improved 1 eV (GaIn)(NAs) Solar Cell Structures," *Journal of Solar Energy Engineering*, vol. 129, no. 3, pp. 266-271, Aug. 2007.
- [5] "Infrared/ Applications." [Online]. Available: <http://en.wikipedia.org/wiki/Infrared#Applications>.
- [6] "Infrared spectroscopy." [Online]. Available: http://en.wikipedia.org/wiki/Infrared_spectroscopy.
- [7] S. S. Kim, C. Young, B. Vidakovic, S. Gabram-Mendola, C. W. Bayer, and B. Mizaikoff, "Potential and Challenges for Mid-Infrared Sensors in Breath Diagnostics," *Sensors Journal, IEEE*, vol. 10, no. 1, pp. 145-158, 2010.
- [8] H. Ishikawa, "Theoretical gain of strained quantum well grown on an InGaAs ternary substrate," *Applied Physics Letters*, vol. 63, no. 6, pp. 712-714, Aug. 1993.
- [9] W. Shockley and H. J. Queisser, "Detailed Balance Limit of Efficiency of p-n Junction Solar Cells," *Journal of Applied Physics*, vol. 32, no. 3, pp. 510-519, Mar. 1961.
- [10] J. F. Geisz et al., "40.8% efficient inverted triple-junction solar cell with two independently metamorphic junctions," *Applied Physics Letters*, vol. 93, no. 12, pp. 123503-123505, Sep. 2008.
- [11] J. Faist, F. Capasso, D. L. Sivco, C. Sirtori, A. L. Hutchinson, and A. Y. Cho, "Quantum Cascade Laser," *Science*, vol. 264, no. 5158, pp. 553-556, Apr. 1994.
- [12] A. Rogalski, J. Antoszewski, and L. Faraone, "Third-generation infrared photodetector arrays," *Journal of Applied Physics*, vol. 105, no. 9, p. 91101, 2009.

References

- [13] G. A. Sai-Halasz, L. Esaki, and W. A. Harrison, "InAs-GaSb superlattice energy structure and its semiconductor-semimetal transition," *Physical Review B*, vol. 18, no. 6, p. 2812, Sep. 1978.
- [14] D. Z. Y. Ting et al., "Type-II Superlattice Infrared Detectors," in *Advances in Infrared Photodetectors*, vol. 84, D. R. R. and C. J. B. T.-S. and S. Sarath D. Gunapala, Ed. Elsevier, 2011, pp. 1-57.
- [15] I. V. and C. L. C. and C. S. K. and M. K. and W. W. B. and J. R. L. and J. A. and J. R. Meyer, "Mid-infrared interband cascade lasers operating at ambient temperatures," *New Journal of Physics*, vol. 11, no. 12, p. 125015, 2009.
- [16] K. Alberi et al., "Valence-band anticrossing in mismatched III-V semiconductor alloys," *Physical Review B*, vol. 75, no. 4, p. 045203, Jan. 2007.
- [17] M. Kondow et al., "GaInNAs: a novel material for long-wavelength semiconductor lasers," *Selected Topics in Quantum Electronics, IEEE Journal of*, vol. 3, no. 3, pp. 719-730, 1997.
- [18] S. A. Barnett, "Direct E[_{sub 0}] energy gaps of bismuth-containing III-V alloys predicted using quantum dielectric theory," *Journal of Vacuum Science & Technology A: Vacuum, Surfaces, and Films*, vol. 5, no. 5, pp. 2845-2848, Sep. 1987.
- [19] S. Francoeur, M.-J. Seong, A. Mascarenhas, S. Tixier, M. Adamczyk, and T. Tiedje, "Band gap of GaAs[_{sub 1-x}]Bi[_{sub x}], 0<x<3.6%," *Applied Physics Letters*, vol. 82, no. 22, p. 3874, 2003.
- [20] D. G. Cooke, F. A. Hegmann, E. C. Young, and T. Tiedje, "Electron mobility in dilute GaAs bismide and nitride alloys measured by time-resolved terahertz spectroscopy," *Applied Physics Letters*, vol. 89, no. 12, p. 122103, Sep. 2006.
- [21] B. Fluegel, S. Francoeur, A. Mascarenhas, S. Tixier, E. C. Young, and T. Tiedje, "Giant Spin-Orbit Bowing in GaAs-_{1-x}Bi-_{x}," *Physical Review Letters*, vol. 97, no. 6, p. 67205, Aug. 2006.
- [22] S. J. Sweeney, Z. Batool, T. J. C. Hosea, and S. R. Jin, "The Potential of III-Bismides for Near- and Mid-IR Photonic Devices," in *1st International Workshop on Bismuth-Containing Semiconductors: Theory, Simulation, and Experiment*, 2010.
- [23] T. Hosoda, G. Kipshidze, G. Tsviid, L. Shterengas, and G. Belenky, "Type-I GaSb-Based Laser Diodes Operating in 3.1- to 3.3 μm Wavelength Range," *Photonics Technology Letters, IEEE*, vol. 22, no. 10, pp. 718-720, 2010.
- [24] J. J. Lee and M. Razeghi, "Exploration of InSbBi for un cooled long-wavelength infrared photodetectors," *OPTO-ELECTRONICS REVIEW*, vol. 6, no. 1, pp. 25-36, 1998.

- [25] A. Rogalski, "Recent progress in infrared detector technologies," *Infrared Physics & Technology*, vol. 54, no. 3, pp. 136-154, May 2011.
- [26] D. Smith and C. Mailhot, "Proposal for strained jour II superlattice infrared detectors," *Journal of Applied Physics*, vol. 62, no. 6, p. 2545, 1987.
- [27] A. Y. Cho and J. R. Arthur, "Molecular beam epitaxy," *Progress in Solid State Chemistry*, vol. 10, no. 3, pp. 157-191, 1975.
- [28] R. F. C. Farrow, *Molecular Beam Epitaxy - Applications to Key Materials*. Noyes Publications, Park Ridge, New Jersey, U.S.A, 1995.
- [29] J. E. Ayers, *Heteroepitaxy of Semiconductors- Theory, Growth and Characterization*. London: Taylor & Francis Group, LLC, 2007.
- [30] J. H. G. Owen, W. Barvosa-Carter, and J. J. Zinck, "Growth oscillation decay rates for control of III--V molecular beam epitaxy near stoichiometry," *Applied Physics Letters*, vol. 76, no. 21, pp. 3070-3072, May 2000.
- [31] I. Tangring, "Metamorphic Heterostructures and Lasers on GaAs," PhD Thesis, Chalmers University of Technology, 2008.
- [32] L. Vegard, "Die Konstitution der Mischkristalle und die Rauffüllung der Atome," *Zeitschrift für Physik A Hadrons and Nuclei*, vol. 5, no. 1, pp. 17-26, Jan. 1921.
- [33] G. Q. Zhao, "Rutherford Backscattering Analysis," *PTCA (PART A: PHYSICAL TESTING)*, vol. 38, no. 1, pp. 41-46, 2002.
- [34] J. Griffiths, "Secondary Ion Mass Spectrometry," *Analytical Chemistry*, vol. 80, no. 19, pp. 7194-7197, Aug. 2008.
- [35] J. Handley, "Product Review: Secondary Ion Mass Spectrometry," *Analytical Chemistry*, vol. 74, no. 11, p. 335 A-341 A, Jun. 2002.
- [36] Z. I. Alferov, "Nobel Lecture: The double heterostructure concept and its applications in physics, electronics, and technology," *Reviews of Modern Physics*, vol. 73, no. 3, p. 767 LP - 782, Oct. 2001.
- [37] M. A. Herman, "Silicon-Based Heterostructures: Strained-Layer Growth by Molecular Beam Epitaxy," *Crystal Research and Technology*, vol. 34, no. 5-6, pp. 583-595, 1999.
- [38] J. W. Matthews and A. E. Blakeslee, "Defects in epitaxial multilayers: I. Misfit dislocations," *Journal of Crystal Growth*, vol. 27, pp. 118-125, Dec. 1974.
- [39] S. M. Wang, T. G. Andersson, V. D. Kulakovskii, and J.-Y. Yao, "Critical layer thickness in $\text{In}_x\text{Ga}_{1-x}\text{As}/\text{GaAs}$ quantum wells studied by photoluminescence and transmission electron microscopy," *Superlattices and Microstructures*, vol. 9, no. 1, pp. 123-126, 1991.

References

- [40] M. Jamil, J. R. Grandusky, V. Jindal, N. Tripathi, and F. Shahedipour-Sandvik, "Mechanism of large area dislocation defect reduction in GaN layers on AlN/Si (111) by substrate engineering," *Journal of Applied Physics*, vol. 102, no. 2, p. 023701, 2007.
- [41] V. M. Ustinov and A. E. Zhukov, "GaAs-based long-wavelength lasers," *Semiconductor Science and Technology*, vol. 15, p. R41-R54, 2000.
- [42] E. S. Semenova et al., "Metamorphic growth for application in long-wavelength (1.3-1.55 μ m) lasers and MODFET-type structures on GaAs substrates," 2003, p. S283-S287.
- [43] H. K. Choi, G. W. Turner, and B. Y. Tsaur, "Monolithic Integration of Si MOSFETs and GaAs-MESFETs," *Ieee Electron Device Letters*, vol. 7, no. 4, pp. 241-243, 1986.
- [44] R. N. Ghosh, B. Griffing, and J. M. Ballantyne, "Monolithic Integration of GaAs Light-Emitting-Diodes and Si Metal-Oxide-Semiconductor Field-Effect Transistors," *Applied Physics Letters*, vol. 48, no. 5, pp. 370-371, 1986.
- [45] H. K. Choi, J. P. Mattia, G. W. Turner, and B. Y. Tsaur, "Monolithic Integration of GaAs/AlGaAs LED and Si Driver Circuit," *Ieee Electron Device Letters*, vol. 9, no. 10, pp. 512-514, 1988.
- [46] M. Y. Frankel, B. Tadayon, and T. F. Carruthers, "Integration of Low-Temperature GaAs on Si Substrates," *Applied Physics Letters*, vol. 62, no. 3, pp. 255-257, 1993.
- [47] H. J. J. Yeh and J. S. Smith, "Fluidic Self-Assembly for the Integration of GaAs Light-Emitting-Diodes on Si Substrates," *Ieee Photonics Technology Letters*, vol. 6, no. 6, pp. 706-708, 1994.
- [48] H. J. Oh, K. J. Choi, W. Y. Loh, T. Htoo, S. J. Chua, and B. J. Cho, "Integration of GaAs epitaxial layer to Si-based substrate using Ge condensation and low-temperature migration enhanced epitaxy techniques," *Journal of Applied Physics*, vol. 102, no. 5, 2007.
- [49] Y. Okada, H. Shimomura, and M. Kawabe, "Low dislocation density GaAs on Si heteroepitaxy with atomic hydrogen irradiation for optoelectronic integration," *Journal of Applied Physics*, vol. 73, no. 11, pp. 7376-7384, 1993.
- [50] M. E. Groenert et al., "Monolithic integration of room-temperature cw GaAs/AlGaAs lasers on Si substrates via relaxed graded GeSi buffer layers," *Journal of Applied Physics*, vol. 93, no. 1, pp. 362-367, 2003.
- [51] M. Yamaguchi, T. Takamoto, K. Araki, and N. Ekins-Daukes, "Multi-junction III-V solar cells: current status and future potential," *Solar Energy*, vol. 79, no. 1, pp. 78-85, Jul. 2005.

-
- [52] M. Song et al., "Influence of the base layer thickness and the graded buffer layer thickness on the conversion efficiency of a metamorphic triple-junction solar cell," 2009, 1st ed., vol. 7518, p. 75180L-9.
- [53] T. Y. Zhang and Y. J. Su, "The critical thickness of an epilayer deposited on a semiconductor-on-insulator compliant substrate," *Applied Physics Letters*, vol. 74, no. 12, pp. 1689-1691, Mar. 1999.
- [54] J. E. Ayers, "Compliant Substrates for Heteroepitaxial Semiconductor Devices: Theory, Experiment, and Current Directions," *Journal of Electronic Materials*, vol. 37, no. 10, pp. 1511-1523, 2008.
- [55] A. Bourret, "Compliant substrates: a review on the concept, techniques and mechanisms," *Applied Surface Science*, vol. 164, no. 1-4, pp. 3-14, Sep. 2000.
- [56] J. Phillips, K. Kamath, J. Singh, and P. Bhattacharya, "Adatom migration effects during molecular beam epitaxial growth of InGaAs/GaAs quantum wells on patterned substrates with vertical sidewalls: Blue shift in luminescence spectra," *Applied Physics Letters*, vol. 68, no. 8, pp. 1120-1122, Feb. 1996.
- [57] H. Wada, H. Sasaki, and T. Kamijoh, "Wafer bonding technology for optoelectronic integrated devices," *Solid-State Electronics*, vol. 43, no. 8, pp. 1655-1663, Aug. 1999.
- [58] A. Trampert, E. Tournie, and K. H. Ploog, "Novel plastic strain-relaxation mode in highly mismatched III-V layers induced by two-dimensional epitaxial growth," *Applied Physics Letters*, vol. 66, no. 17, pp. 2265-2267, Apr. 1995.
- [59] S. H. Huang, G. Balakrishnan, a. Khoshakhlagh, a. Jallipalli, L. R. Dawson, and D. L. Huffaker, "Strain relief by periodic misfit arrays for low defect density GaSb on GaAs," *Applied Physics Letters*, vol. 88, no. 13, p. 131911, 2006.
- [60] S. H. Huang, G. Balakrishnan, A. Khoshakhlagh, L. R. Dawson, and D. L. Huffaker, "Simultaneous interfacial misfit array formation and antiphase domain suppression on miscut silicon substrate," *Applied Physics Letters*, vol. 93, no. 7, pp. 71102-71103, Aug. 2008.
- [61] C.-A. Chang, C. M. Serrano, L. L. Chang, and L. Esaki, "Studies by cross-sectional transmission electron microscope of InAs grown by molecular beam epitaxy on GaAs substrates," *Applied Physics Letters*, vol. 37, no. 6, pp. 538-540, Sep. 1980.
- [62] C. J. Nuese, R. E. Enstrom, and M. Ettenberg, "Room-temperature laser operation of In_xGa_{1-x}As p-n junctions," *Applied Physics Letters*, vol. 24, no. 2, pp. 83-85, Jan. 1974.

References

- [63] N. Rorsman, C. Karlsson, S. M. Wang, H. Zirath, and T. G. Anderson, "DC and RF performance of 0.15 μm gate length In_{0.70}Al_{0.30}As/In_{0.80}Ga_{0.20}As HFETs on GaAs substrate," *Electronics Letters*, vol. 31, no. 15, pp. 1292-1294, 1995.
- [64] S. M. Wang et al., "Molecular beam epitaxy growth and characterization of In_xGa_{1-x}As (0.57 $\leq x \leq 1$) on GaAs using InAlAs graded buffer," *Journal of Crystal Growth*, vol. 175-176, no. 2, pp. 1016-1021, May 1997.
- [65] O. Baklenov et al., "Molecular-beam epitaxy production of large-diameter metamorphic high electron mobility transistor and heterojunction bipolar transistor wafers," in *Papers from the 20th North American Conference on Molecular Beam Epitaxy*, 2002, vol. 20, no. 3, pp. 1200-1204.
- [66] D. Wu et al., "Low threshold current density 1.3 μm metamorphic InGaAs/GaAs quantum well laser diodes," *Electronics Letters*, vol. 44, no. 7, pp. 474-475, 2008.
- [67] I. Tangring et al., "1.58 μm InGaAs quantum well laser on GaAs," *Applied Physics Letters*, vol. 91, no. 22, p. 221101, 2007.
- [68] K. E. Lee and E. A. Fitzgerald, "High-quality metamorphic compositionally graded InGaAs buffers," *Journal of Crystal Growth*, vol. 312, no. 2, pp. 250-257, 2010.
- [69] H. K. H. Choy and J. C. G. Fonstad, "Effects of substrate temperature on the growth of InGaAs compositionally graded buffers and on quantum well structures grown above them," *Journal of Vacuum Science & Technology B: Microelectronics and Nanometer Structures*, vol. 23, no. 5, pp. 2109-2113, 2005.
- [70] Y. B. Bolkhovityanov, A. S. Deryabin, A. K. Gutakovskii, M. A. Revenko, and L. V. Sokolov, "Strain relaxation of GeSi/Si(001) heterostructures grown by low-temperature molecular-beam epitaxy," *Journal of Applied Physics*, vol. 96, no. 12, pp. 7665-7674, Dec. 2004.
- [71] E. B. Chen, D. C. Paine, P. N. Uppal, K. Nichols, and J. S. Ahearn, "Surface morphology evolution in highly mismatched Sb-graded buffer layers on GaAs," *Applied Physics Letters*, vol. 78, no. 16, pp. 2345-2347, Apr. 2001.
- [72] J. Schone, E. Spiecker, F. Dimroth, A. W. Bett, and W. Jager, "Misfit dislocation blocking by dilute nitride intermediate layers," *Applied Physics Letters*, vol. 92, no. 8, pp. 81903-81905, 2008.
- [73] Y. Takano, T. Kururi, K. Kuwahara, and S. Fuke, "Residual strain and threading dislocation density in InGaAs layers grown on Si substrates by metalorganic vapor-phase epitaxy," *Applied Physics Letters*, vol. 78, no. 1, pp. 93-95, Jan. 2001.

- [74] I. N. Stranski and L. V. Krastanow, "Abhandlungen der Mathematisch-Naturwissenschaftlichen Klasse," *Akademie der Wissenschaften und der Literatur in Mainz*, vol. 146, p. 797.
- [75] A. Martí, L. Cuadra, and A. Luque, "Design constraints of the quantum-dot intermediate band solar cell," *Physica E: Low-dimensional Systems and Nanostructures*, vol. 14, no. 1-2, pp. 150-157, Apr. 2002.
- [76] S. Nakamura et al., "Bright electroluminescence from CdS quantum dot LED structures," *Electronics Letters*, vol. 34, no. 25, pp. 2435-2436, Dec. 1998.
- [77] P. Bhattacharya, Z. Mi, J. Yang, D. Basu, and D. Saha, "Quantum dot lasers: From promise to high-performance devices," *Journal of Crystal Growth*, vol. 311, no. 7, pp. 1625-1631, 2009.
- [78] D. J. Eaglesham and M. Cerullo, "Dislocation-free Stranski-Krastanow growth of Ge on Si(100)," *Physical Review Letters*, vol. 64, no. 16, p. 1943 LP - 1946, Apr. 1990.
- [79] R. Jothilingam, M. Koch, J. Posthill, and G. Wicks, "A study of cracking in GaN grown on silicon by molecular beam epitaxy," *Journal of Electronic Materials*, vol. 30, no. 7, pp. 821-824, Jul. 2001.
- [80] G. Salviati et al., "Structural characterization of InGaAs/InP heterostructures grown under compressive and tensile stress," *Applied Surface Science*, vol. 188, no. 1-2, pp. 36-48, 2002.
- [81] M. Natali et al., "Crack formation in tensile InGaAs/InP layers," *Journal of Vacuum Science & Technology B*, vol. 18, no. 5, pp. 2527-2533, 2000.
- [82] H. Ye, P. Lu, Z. Yu, Y. Song, D. Wang, and S. Wang, "Critical Thickness and Radius for Axial Heterostructure Nanowires Using Finite-Element Method," *Nano Letters*, vol. 9, no. 5, pp. 1921-1925, 2009.
- [83] E. A. Fitzgerald, "Dislocations in strained-layer epitaxy: theory, experiment, and applications," *Materials Science Reports*, vol. 7, no. 3, pp. 87-140, 1991.
- [84] E. Peierls, "The size of a dislocation," *Proc. Phys. Soc.*, vol. 52, p. 34, 1940.
- [85] I. Yonenaga and K. Sumino, "Impurity effects on the generation, velocity, and immobilization of dislocations in GaAs," *Journal of Applied Physics*, vol. 65, no. 1, pp. 85-92, 1989.
- [86] O. Yastrubchak et al., "Misfit strain anisotropy in partially relaxed lattice-mismatched InGaAs/GaAs heterostructures," *Journal of Physics: Condensed Matter*, vol. 16, no. 2, p. S1-S8, 2004.
- [87] Y. S. Sergey, J. Flemming, and P. Jon Wulff, "On the nature of cross-hatch patterns on compositionally graded Si_{1-x}Gex alloy layers," *Applied Physics Letters*, vol. 64, no. June, pp. 3305-3307, 1994.

References

- [88] A. E. Romanov, W. Pompe, S. Mathis, G. E. Beltz, and J. S. Speck, "Threading dislocation reduction in strained layers," *Journal of Applied Physics*, vol. 85, no. 1, pp. 182-192, Jan. 1999.
- [89] I. Tångring, S. M. Wang, X. R. Zhu, A. Larsson, Z. H. Lai, and M. Sadeghi, "Manipulation of strain relaxation in metamorphic heterostructures," *Applied Physics Letters*, vol. 90, no. 7, p. 071904, 2007.
- [90] S. K. Mathis, X. H. Wu, A. E. Romanov, and J. S. Speck, "Threading dislocation reduction mechanisms in low-temperature-grown GaAs," *Journal of Applied Physics*, vol. 86, no. 9, pp. 4836-4842, 1999.
- [91] J. Tersoff, "Dislocations and strain relief in compositionally graded layers," *Applied Physics Letters*, vol. 62, p. 693, 1993.
- [92] J. M. Moison, C. Guille, F. Houzay, F. Barthe, and M. Van Rompay, "Surface segregation of third-column atoms in group III-V arsenide compounds: Ternary alloys and heterostructures," *Physical Review B*, vol. 40, no. 9, p. 6149, 1989.
- [93] M. Peach and J. S. Koehler, "The Forces Exerted on Dislocations and the Stress Fields Produced by Them," *Physical Review*, vol. 80, no. 3, p. 436 LP - 439, Nov. 1950.
- [94] I. J. Fritz, P. L. Gourley, L. R. Dawson, and J. E. Schirber, "Electrical and optical studies of dislocation filtering in InGaAs/GaAs strained-layer superlattices," *Applied Physics Letters*, vol. 53, no. 12, pp. 1098-1100, Sep. 1988.
- [95] N. A. El-Masry, J. C. L. Tarn, and S. M. Bedair, "Combined effect of strained-layer superlattice and annealing in defects reduction in GaAs grown on Si substrates," *Applied Physics Letters*, vol. 55, no. 14, pp. 1442-1444, Oct. 1989.
- [96] K. Samonji et al., "Reduction of threading dislocation density in InP-on-Si heteroepitaxy with strained short-period superlattices," *Applied Physics Letters*, vol. 69, no. 1, pp. 100-102, Jul. 1996.
- [97] Z. Mi, J. Yang, P. Bhattacharya, and D. L. Huffaker, "Self-organised quantum dots as dislocation filters: the case of GaAs-based lasers on silicon," *Electronics Letters*, vol. 42, no. 2, pp. 121-123, 2006.
- [98] Y. Jun, P. Bhattacharya, and M. Zetian, "High-Performance In_{0.5}Ga_{0.5}As/GaAs Quantum-Dot Lasers on Silicon With Multiple-Layer Quantum-Dot Dislocation Filters," *Electron Devices, IEEE Transactions on*, vol. 54, no. 11, pp. 2849-2855, 2007.
- [99] D. Huang, M. A. Reshchikov, F. Yun, T. King, A. A. Baski, and H. Morkoc, "Defect reduction with quantum dots in GaN grown on sapphire substrates by molecular beam epitaxy," *Applied Physics Letters*, vol. 80, no. 2, pp. 216-218, Jan. 2002.

- [100] K. Momose et al., "Hardening Effect of GaP_{1-x}N_x and GaAs_{1-x}N_x Alloys by Adding Nitrogen Atoms," *Japanese Journal of Applied Physics*, vol. 41, no. Part 1, No. 12, p. 7301 LP - 7306.
- [101] G. Sai-Halasz, R. Tsu, and L. Esaki, "A new semiconductor superlattice," *Applied Physics Letters*, vol. 30, no. 12, p. 651, 1977.
- [102] P.-Y. Delaunay, B. M. Nguyen, D. Hoffman, E. K.-W. Huang, and M. Razeghi, "Background Limited Performance of Long Wavelength Infrared Focal Plane Arrays Fabricated From M-Structure InAs/GaSb Superlattices," *Quantum Electronics, IEEE Journal of*, vol. 45, no. 2, pp. 157-162, 2009.
- [103] A. S. Bracker, M. J. Yang, B. R. Bennett, J. C. Culbertson, and W. J. Moore, "Surface reconstruction phase diagrams for InAs, AlSb, and GaSb," *Journal of Crystal Growth*, vol. 220, no. 4, pp. 384-392, Dec. 2000.
- [104] A. Khoshakhlagh, E. Plis, S. Myers, Y. D. Sharma, L. R. Dawson, and S. Krishna, "Optimization of InAs/GaSb type-II superlattice interfaces for long-wave (~8 [μ]m) infrared detection," *Journal of Crystal Growth*, vol. 311, no. 7, pp. 1901-1904, Mar. 2009.
- [105] L. Bürkle, F. Fuchs, J. Schmitz, and W. Pletschen, "Control of the residual doping of InAs/(GaIn)Sb infrared superlattices," *Applied Physics Letters*, vol. 77, no. 11, p. 1659, 2000.
- [106] R. Kaspi, J. Steinshnider, M. Weimer, C. Moeller, and A. Ongstad, "As-soak control of the InAs-on-GaSb interface," *Journal of Crystal Growth*, vol. 225, no. 2-4, pp. 544-549, May 2001.
- [107] E. Plis, S. Annamalai, K. T. Posani, S. Krishna, R. A. Rupani, and S. Ghosh, "Midwave infrared type-II InAs/GaSb superlattice detectors with mixed interfaces," *Journal of Applied Physics*, vol. 100, no. 1, p. 14510, 2006.
- [108] I. Vurgaftman, J.R. Meyer, and L. R. Ram-Mohan, "Band parameters for III-V compound semiconductors and their alloys," *Journal of Applied Physics*, vol. 89, p. 5815, 2001.
- [109] K. Oe and H. Okamoto, "New Semiconductor Alloy GaAs_{1-x}Bi_x Grown by Metal Organic Vapor Phase Epitaxy," *Japanese Journal of Applied Physics*, vol. 37, no. Part 2, No. 11A, p. L1283 LP - L1285, 1998.
- [110] S. Tixier et al., "Molecular beam epitaxy growth of GaAs_{1-x}Bi_x," *Applied Physics Letters*, vol. 82, no. 14, p. 2245, 2003.
- [111] J. Zilko and J. Greene, "Growth of metastable InSb_{1-x}Bi_x thin films by multitarget sputtering," *Applied Physics Letters*, vol. 33, no. 3. AIP, p. 254, 1978.

References

- [112] K. Oe, S. Ando, and K. Sugiyama, "InSb_{1-x}Bi_x Films Grown by Molecular Beam Epitaxy," *Japanese Journal of Applied Physics*, vol. 20, no. 4, p. L303 LP - L306, 1981.
- [113] A. Noreika, W. Takei, M. Francombe, and C. Wood, "Indium antimonide-bismuth compositions grown by molecular beam epitaxy," *Journal of Applied Physics*, vol. 53, no. 7, p. 4932, 1982.
- [114] Z. Fang, K. Ma, R. Cohen, and G. Stringfellow, "Photoluminescence of InAsBi and InAsSbBi grown by organometallic vapor phase epitaxy," *Journal of Applied Physics*, vol. 68, no. 3. AIP, p. 1187, 1990.
- [115] P. Dutta, H. Bhat, and V. Kumar, "The physics and technology of gallium antimonide: An emerging optoelectronic material," *Journal of Applied Physics*, vol. 81, no. 9. AIP, p. 5821, 1997.
- [116] P. Gladkov, E. Monova, and J. Weber, "Liquid phase epitaxy and photoluminescence characterization of p-type GaSb layers grown from Bi based melts," *Journal of Crystal Growth*, vol. 146, no. 1-4, pp. 319-325, Jan. 1995.
- [117] A. Danilewsky et al., "Growth and characterization of GaSb bulk crystals with low acceptor concentration," *Journal of Electronic Materials*, vol. 25, no. 7, pp. 1082-1087, 1996.
- [118] S. Tixier, M. Adamcyk, E. C. Young, J. H. Schmid, and T. Tiedje, "Surfactant enhanced growth of GaNAs and InGaNAs using bismuth," *Journal of Crystal Growth*, vol. 251, no. 1-4, pp. 449-454, Apr. 2003.
- [119] R. R. Reddy, S. Anjaneyulu, and R. Viswanath, "Optical and electronic properties of compound semi-conductors," *Infrared Physics*, vol. 33, no. 5, pp. 385-388, Sep. 1992.
- [120] M. A. Berding, A. Sher, A.-B. Chen, and W. E. Miller, "Structural properties of bismuth-bearing semiconductor alloys," *Journal of Applied Physics*, vol. 63, no. 1, pp. 107-115, Jan. 1988.
- [121] A. Janotti, S.-H. Wei, and S. B. Zhang, "Theoretical study of the effects of isovalent coalloying of Bi and N in GaAs," *Physical Review B*, vol. 65, no. 11, p. 115203, Feb. 2002.
- [122] A. R. Mohmad, F. Bastiman, C. J. Hunter, J. S. Ng, S. J. Sweeney, and J. David, "The effect of Bi composition to the optical quality of GaAs_{1-x}Bi_x," *Applied Physics Letters*, vol. 99, no. 4. AIP, p. 42107, 2011.
- [123] Y. Kajikawa, S. Asahina, and N. Kanayama, "X-Ray Diffraction Measurements on Lattice Mismatch of InTlAs Grown on InAs Substrates," *Japanese Journal of Applied Physics*, vol. 40, no. Part 1, No. 1, pp. 28 - 33, 2001.

- [124] R. Kaspi and K. R. Evans, "Sb-surface segregation and the control of compositional abruptness at the interface," *Journal of Crystal Growth*, vol. 175-176, no. 2, pp. 838-843, May 1997.
- [125] L. W. Sung and H. H. Lin, "Highly strained 1.24- μ m InGaAs/GaAs quantum-well lasers," *Applied Physics Letters*, vol. 83, no. 6, pp. 1107-1109, Aug. 2003.
- [126] E. Tournié and K. H. Ploog, "Surfactant-mediated molecular beam epitaxy of strained layer semiconductor heterostructures," *Thin Solid Films*, vol. 231, no. 1-2, pp. 43-60, Aug. 1993.
- [127] "Wavelength Engineering." [Online]. Available: http://www.tf.uni-kiel.de/matwis/amat/semi_en/kap_5/backbone/r5_1_4.html.
- [128] V. P. Germogenov, Y. I. Otman, V. V. Chaldyshev, and Y. V. Shmartsev, "Width of the band gap in GaSb_{1-x}Bi_x solid solutions," *Soviet physics: Semiconductors*, vol. 23, no. 8, pp. 942-943, 1989.